Characterization of three mineralization styles of the Revenue Au occurrence, Dawson Range, Yukon Territory, Canada: implications for a large-scale, intrusion related system

By
Mariah C.J. Williams

A Thesis Submitted to
Saint Mary's University, Halifax, Nova Scotia
in Partial Fulfillment of the Requirements for
the Degree of Bachelor of Science in Geology.

April 26th 2019, Halifax, Nova Scotia

Approved: Dr. Jacob Hanley
Full Professor and
Supervisor
Department of Geology

Approved: Dr. Erin Adlakha
Assistant Professor
and Supervisor
Department of Geology

Date: April 26th 2019

Characterization of three mineralization styles of the Revenue Au occurrence, Dawson Range, Yukon Territory, Canada: implications for a large-scale, intrusion related system

by Mariah C.J. Williams

Abstract

The Revenue Au occurrence, located in Dawson Range, Yukon, Canada is a complex magmatic-hydrothermal system comprised of at least three styles of mineralization with distinct mineral assemblages and textures, though the paragenic relationship between styles is poorly understood. This integrated field and microanalytical study aims to characterize the styles of mineralization using petrography, mineral chemical analysis, and thermometric methods. Methods applied include SEM-BSE imaging, EMPA analysis of the major and minor chemical compositions of sulfides and sulfarsenides, and LA-ICP-MS analysis of trace elements in major sulfides. The data show that in the Blue Sky Zone of the Revenue granite host rock, *style 1* mineralization is divided into an earlier, porphyry-like mineralization stage (Cu-Au) which is later overprinted by a later, epithermal-like (Cu-Ag-Au-Mo) mineralization stage. The breccia-hosted and W-Sn enriched *style 2* mineralization (Cu-Au-Mo-W) cross-cuts the early *style 1* mineralization, and both early *style 1* and *style 2* mineralization are cross-cut by diatreme-hosted *style 3* mineralization. Additionally, regional quartz-feldspar porphyry dykes are commonly associated with Au mineralization in the Dawson Range. This study shows that at the Revenue location there is evidence that these dykes formed pre- to syn- mineralization with respect to late *style 1* and *style 2* mineralization, suggesting their involvement in the formation of Au mineralization on site.

April 25th, 2019

Table of Contents

List of Figures

List of Tables

1.0 Introduction

The Dawson Range of the Tintina Gold Belt, located in west-central Yukon Territory, Canada, hosts numerous high-grade Au deposits (Fig. 1), including the Coffee and Golden Saddle deposits (MacKenzie et al., 2014; MacWilliam, 2018), and multiple Cu-Au-(Mo) deposits and showings including the Minto and Casino systems (Tafti and Mortensen, 2003; Godwin, 1976) (see Appendix 2 for additional comparisons). The Freegold Mountain Property is located 200 km north-west of Carmacks within the Dawson Range, and hosts several Cu-Au occurrences. Northern Freegold Resources Ltd. delineated three Au and polymetallic NI-43-101 compliant resources in the Freegold Mountain Property: (i) the Revenue Cu-Au-Mo-Ag- occurrence, (ii) the Nucleus Ag-Au-Bi-Cu occurrence, and (iii) the Tinta Hill Ag-Pb-Zn-Cu-Au vein occurrence (Northern Freegold Resources Ltd., 2015). The Revenue occurrence, the focus of this study, has an inferred resource of 80.8 million tonnes, grading 0.39 g/t Au, 3.45 g/t Ag, 0.14% Cu and 0.05% Mo (Northern Freegold Resources Ltd., 2015).

The Revenue occurrence is unique compared to the other Au showings on the property as it contains associated Mo and W mineralization. Current geological data from exploration activities suggests that mineralization was formed by at least two separate magmatic-hydrothermal events. Three styles of mineralization have been observed in drill core:

(i) *Porphyry-style mineralization* comprising early, granite-hosted, quartz-sulfide (pyrite, chalcopyrite) stockwork associated with potassic alteration (K-feldspar, biotite), and later, quartz-carbonate-sulfide (molybdenite, chalcopyrite, pyrite, pyrrhotite) stockwork. This

style of mineralization is spatially constrained to an area of the Revenue granite (the country rock in the area) called the Blue Sky Zone.

(ii) *Breccia-hosted mineralization* comprising quartz-sulfide (pyrite, chalcopyrite, molybdenite) matrix with minor scheelite associated with phyllic to argillic alteration. This breccia is called the "WAu Breccia" by workers and is spatially related to the contact of the Revenue granite with a cross-cutting hypabyssal diatreme (the Revenue diatreme) and quartz-feldspar-porphyry dykes that cross-cut the Revenue granite.

(iii) *Replacement-style mineralization,* associated with the Revenue diatreme, consisting of sulfide mineralization and replacement in the hydrothermal breccia along the margins of the diatreme (Northern Freegold Resources Ltd, 2017).

The close proximity of these occurrences suggest a broad genetic link between mineralized styles.

This integrated field and microanalytical study characterizes the mineralogy, paragenesis, and timing of the different styles of mineralization at the Revenue occurrence in order to better understand their genetic relationship to one another and relative timing. The results of this work provide new constraints for, and revisions to, the basic genetic model for the Revenue occurrence, with an intention to improve exploration success. Petrographic investigations by optical microscopy, scanning electron microscopy, and short-wave infrared spectroscopy (Terraspec®) was used to: (i) identify and characterize ore and accessory minerals, and associated alteration; (ii) examine microscopic textures to develop a paragenetic sequence; and (iii) determine the major and minor element composition of ore and alteration mineral phases. An electron microprobe analyzer (EMPA) was used to quantify major and minor element abundances in sulfide and

sulfarsenide minerals (sphalerite, pyrite, pyrrhotite, arsenopyrite, and glaucodot), allowing for the calculation of mineralization temperatures. Laser ablation inductively-coupled plasma mass spectrometry (LA-ICP-MS) was used to determine sulfide trace element abundances in order to characterize the chemical signatures of different mineralization styles.

2.0 Geological setting

2.1 Regional geology

The Freegold Mountain Property is located ~200 km northwest of Whitehorse, Yukon Territory, Canada, in the Dawson Range and is part of the Tintina Gold Province (Northern Freegold Resources Ltd, 2015). This region comprises predominantly Paleozoic metasediments and metavolcanics of the Yukon-Tanana Terrane (YTT), and is situated between two major NW-SE structures, the Tintina Fault to the northeast and Denali Fault to the southwest (Fig. 1). The YTT sediments were originally deposited on the NW passive margin of ancestral North America (Laurentia) after the breakup of Rodinia (800 to 700 Ma; Oriolo et al., 2017), with deposition lasting until the Middle Devonian (Bineli-Betsi et al., 2010, 2011, 2012, 2016; Allan et al., 2013). Subduction of oceanic crust under western Laurentia initiated during the middle Devonian (~365 Ma), producing a continental arc and associated back-arc basin (~360 Ma; Allan et al., 2013). Extension within the back-arc led to the formation of an ocean basin and the intrusion of mafic to felsic plutonic suites and emplacement of volcanic rock, until its closure in the late Permian through subduction (Allan et al., 2013). This second period of subduction led to the Klondike orogeny (~260 to 253 Ma; Beranek et al., 2011), which resulted the accretion of the over-thickened crust of YTT on top of Laurentia.

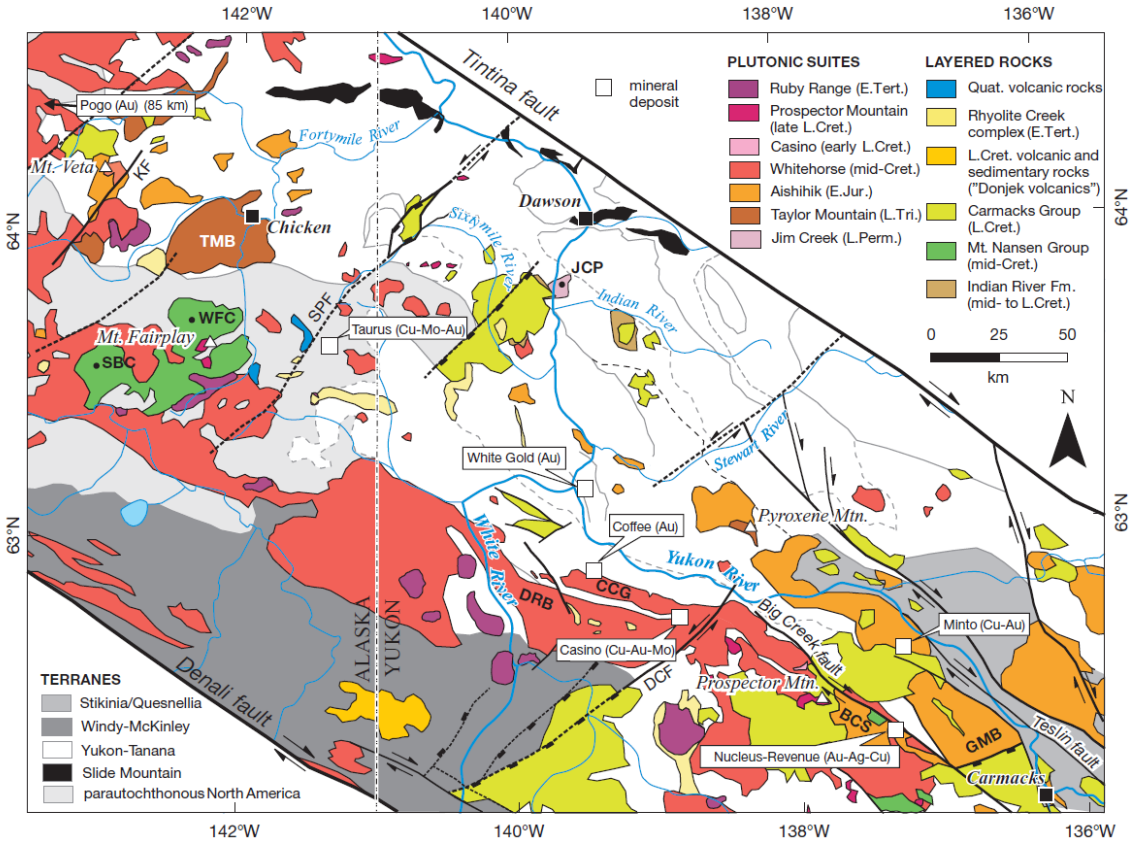

Figure 1. Simplified regional map of plutonic and volcanic suites intruding and overlying the Dawson Range area, Yukon (Foster (1970, 1976); Bacon and Lanphere (1996); Gordey and Makepeace (2003); Gordey and Ryan (2005); Murphy et al. (2009); Ryan et al. (2010, 2013a, b); Sánchez et al. (2013); Staples et al. (in press); Allan et al. 2013). Major faults are black and approximate tectonostratigraphic domain boundaries are in dashed lines. Lithology and structure abbreviations: BCS = Big Creek Syenite, CCG = Coffee Creek granite, DRB = Dawson Range Batholith, GMB = Granite Mountain batholith, JCP = Jim Creek pluton, SBC = Sixty Mile Butte caldera, TMB = Taylor mountain batholith, WFC = West Fork caldera. Fault abbreviations: DCF = Dip creek fault, KF = Kechumstuk fault, SPF = Sixtymile-Pika fault.

In the late Triassic to early Jurassic, convergence through subduction on the western coast of Laurentia resulted in magmatism within the Yukon-Tanana Arc and produced the metaluminous, mafic to intermediate intrusions of the Taylor Mountain Plutonic Suite and felsic intrusions of the Aishihik Plutonic Suite (Allan et al., 2013; Fig. 1). Magmatism ceased from the middle Jurassic to the early Cretaceous (~179 - 115 Ma), and during this period of inactivity the region experienced uplift and exhumation (Allan et al., 2013).

Renewed subduction below the Yukon Tanana Arc in the Mid-Cretaceous (~98 - 115 Ma) generated the Whitehorse Plutonic Suite, a suite of intermediate to felsic plutons, including the metaluminous Dawson Range Batholith (Fig. 1). In the back-arc basin, extensional tectonic activity led to low angle normal faults and ductile shear zone between the lower plate and the thrusted plate of the YTT. Following this episode of magmatism in the Dawson Range, a 40-million-year period of sedimentation occurred in an alluvial fan setting and transitioned into a shallow marine environment. Sedimentation in the back-arc basin was preserved as the Indian River Formation (Fig. 1). Volcanic rocks and high-level magmatic stocks of the Carmacks Group were emplaced over the Indian River Formation and a broad area of the Tintina Gold Province between 72 and 67 Ma (Allan et al., 2013 and references therein; Fig. 1). This formation is comprised of shoshonitic, high-Mg, intermediate to felsic volcanic rocks.

2.2 Property-scale geology

The Freegold Mountain area is located the southeast Dawson Range, and contains three major Cu-Au (± Mo, W, Ag) occurrences (Revenue, Nucleus, and Tinta) with 11 additional Au showings (Fig. 2; Friend et al., 2018). The property consists of the YTT intruded by the Big Creek Syenite of the Jurassic Aishihik Plutonic Suite, and the Dawson

Range Batholith of the mid-Cretaceous Whitehorse Plutonic Suite (Allan et al., 2013). The Dawson Range Batholith hosts small intrusions of the Casino Plutonic Suite in the late Cretaceous (79 to 70 Ma; Allan et al., 2013; Friend et al., 2018). A dextral strike-slip fault, the Big Creek Fault, runs through the Freegold Mountain area and is oriented parallel to the regional-scale Tintina and Denali Faults (Northern Freegold Resources Ltd, 2015). The Big-Creek Fault diverges into northern and southern fault segments NW of the Revenue occurrence, with the Nucleus occurrence on the southern segment, west of Revenue occurrence, and the Tinta Hill occurrence lying on the northern segment, east of the Revenue occurrence (Fig. 2). Allan et al. notes that it is unclear whether the Dawson Range Batholith pre-dates the Big Creek fault between 107 - 100 Ma (2013). Secondary features include sets of porphyritic dykes, generally striking west to east (Bineli-Betsi et al., 2010, 2011, 2012, 2016). These dykes are spatially associated with mineralized veins and may also be genetically related since some host pyrite-chalcopyrite along their altered margins (Bineli-Betsi and Lentz, 2011).

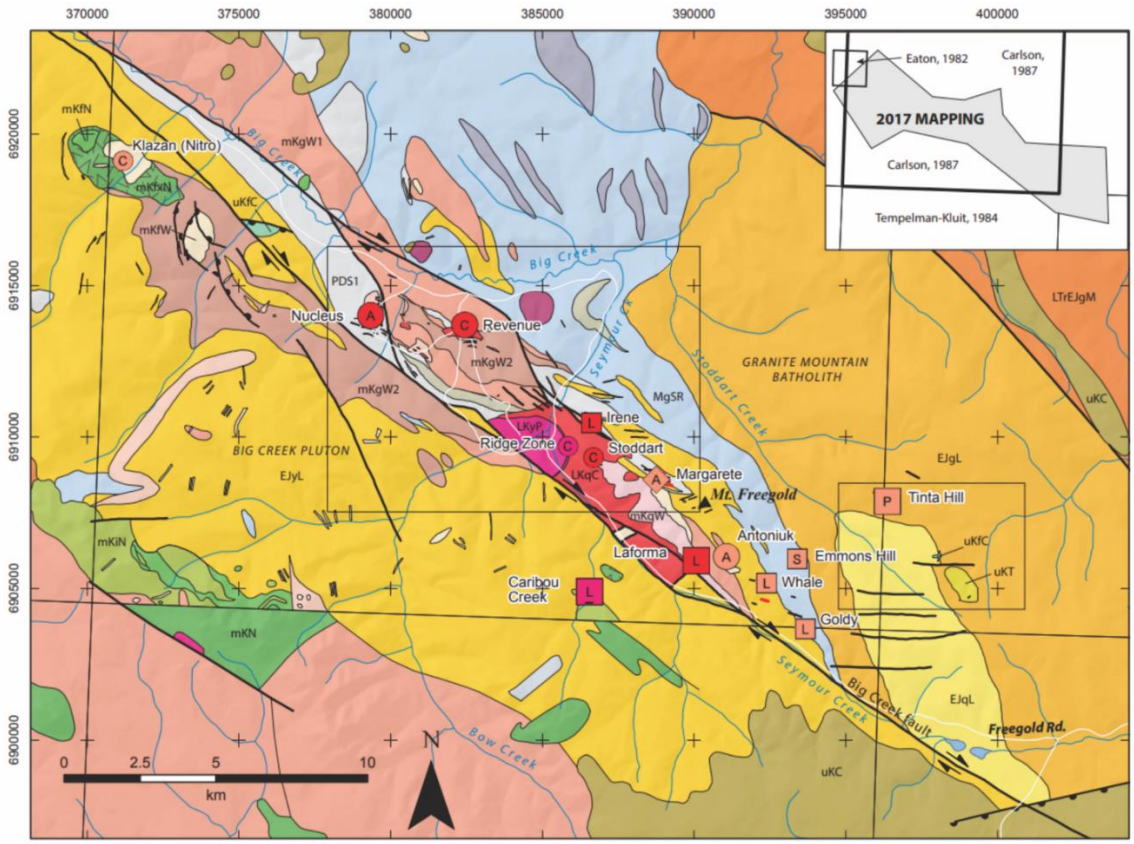

Figure 2. Geological map of Triumph Gold Corp's property in the Freegold Mountain area (after Eaton, 1982; Templemen-Kluit, 1984; Carlson, 1987; Friend et al., 2018). The Big Creek Fault is represented by the central dextral strike-slip fault (Allan et al., 2013; Bineli-Betsi et al., 2016).

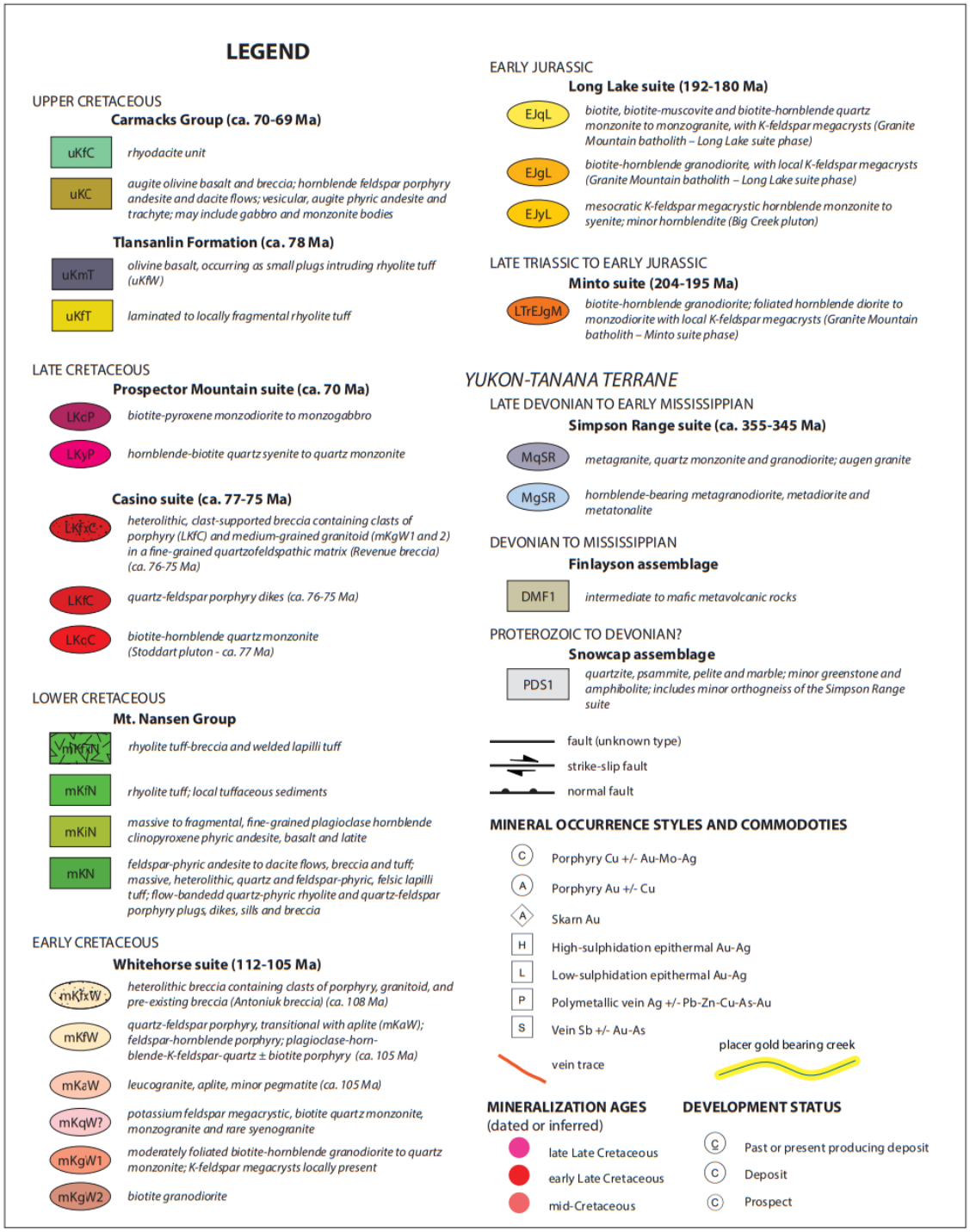

Figure 2 (cont'd). Legend accompanying geological map of Triumph Gold property (after Eaton, 1982; Templemen-Kluit, 1984; Carlson, 1987; Friend et al., 2018). Strike Slip faults are sections of the Big Creek Fault, which diverge around the Revenue occurrence (Bineli-Betsi et al., 2016; Allan et al., 2013).

The Revenue occurrence is located in a dilational zone between the northern and southern segments of the Big Creek Fault, in the Dawson Range Batholith (Fig. 2). The occurrence is comprised of quartz-chalcopyrite-pyrite veins and vein stockwork, and disseminated pyrite and chalcopyrite mineralization in the granodiorite (Northern Freegold Resources Ltd, 2015). Locally, Cu-Au±Mo±W mineralization is more abundant at the contacts with the Revenue diatreme and near porphyritic dykes (Northern Freegold Resources Ltd, 2015). Both the Nucleus and Revenue occurrences are intrusive, fine-grained, intermediate to felsic monzonites to granites hypothesized to be emplaced in the mid Cretaceous (Bineli-Betsi et al., 2010; Allan et al., 2013, Friend et al., 2018). The Nucleus occurrence is situated in a fine-grained, tabular granitic intrusion with a microgranitic texture that was later crosscut by quartz-feldspar porphyry (QFP) dykes, and located ~3 km west of Revenue (Bineli-Betsi and Lentz, 2011) and 1 km north of the Big Creek-South fault (Fig. 2). Gold mineralization is more abundant in brecciated zones, and along contacts with intrusive porphyritic plugs that lie in a west-east trend (Northern Freegold Resources Ltd, 2015), and are hypothesized to have been emplaced within zones of dilation (T. Baressi, personal communication 2018). South-east of the Revenue occurrence, the northern segment of the Big Creek fault is terminated near a mineralized zone called “Stoddart” on the property, whereas the southern segment continues (Fig. 2). The Stoddart zone contains an abundance of deformed late Cretaceous rocks, and the shape of the Big Creek fault segments are more deformed in this area. The Tinta Hill occurrence is located approximate 15 km SE from the Revenue occurrence and is hosted in granite and K-feldspar-rich monzonite of the Aishihik Lake plutonic suite (Northern Freegold Resources Ltd, 2015) (Fig. 2). Mineralization consists of quartz-carbonate-sulfide veins

containing chalcopyrite, pyrite, sphalerite and galena (Northern Freegold Resources Ltd, 2015).

In the southeastern region of the Dawson Range batholith, calc-alkaline, high-level porphyry dykes and breccias are spatially associated with, and locally controlled by, the Big Creek Fault (Bineli-Betsi et al., 2016). These dykes and breccias intrude the Dawson Range batholith and crosscut, or are associated with, mineralization at the Nucleus-Revenue locality (Bineli-Betsi et al., 2016; Allan et al., 2013).

2.3 History of mineral exploration at the Freegold Mountain Property

Numerous Au occurrences occur in the Freegold Mountain Property (Bineli-Betsi et al., 2010, 2011, 2012, 2016; Bineli-Betsi and Lentz, 2011; Allan et al., 2013) and exploration has been active in this area for over 80 years. It was originally prospected by P.F. Guder in 1930 and in 1968 Yukon Revenue Mines Ltd. laid the first claim. The property underwent exploration and was owned by multiple individuals and companies over the past 50 years (Northern Freegold Ltd., 2015). In 2006, Northern Freegold Resources Corp. (now Triumph Gold Corp.) purchased the property and its claim rights and continued exploration drilling until 2012, and again in 2017-2018 (Northern Freegold Resources Ltd., 2015).

2.4 Deposit-scale geology

The Revenue occurrence is largely hosted by a medium-grained, equigranular to weakly porphyritic, melanocratic, biotite-hornblende granite (herein termed Revenue granite) of the Dawson Range batholith, dated to 102.5±0.6 Ma (Bineli-Betsi et al., 2016; Northern Freegold Resources Ltd., 2017; Friend et al., 2018). On the its margin the granite is melanocratic, contains gneissic to schistose xenoliths, and is discontinuously altered to a

phyllic mineral assemblage (Northern Freegold Resources Ltd., 2015). The Revenue granite hosts a felsic to intermediate, pyroclastic volcanic pipe (herein termed the Revenue diatreme) that has been dated to ~75 Ma and east-west striking quartz-feldspar porphyry (QFP) dykes (Bineli-Betsi et al., 2016; Northern Freegold Resources Ltd., 2017). Two other granitoids, a medium-grained, equigranular leucogranite and a foliated to non-foliated, locally porphyritic, fine-grained leucogranite, occur in the area but do not appear to be genetically or spatially associated with mineralization (Bineli-Betsi et al., 2016).

East-west trending porphyritic dykes crosscut the Revenue granite and the fine-grained felsic granite that hosts the Nucleus occurrence (Bineli-Betsi and Lentz, 2011). These dyke swarms have attributed the dykes to the Casino plutonic suite (Fig. 2) and dated to 76-75 Ma (Allan et al., 2013; Bineli-Betsi et al., 2016; Friend et al., 2018) and may be spatially associated with mineralization throughout the Dawson Range (Bineli-Betsi and Lentz, 2011). The dykes are mainly composed of quartz-feldspar porphyry, and can be further subdivided based on abundance of quartz phenocrysts relative to feldspar phenocrysts (Bineli-Betsi et al., 2011). Quartz clasts are typically rounded, and are sometimes referred to as “quartz eyes”. They may be strained into elongated grains. Feldspar crystals are euhedral and typically altered to sericite, though epidote alteration may also be present (Bineli-Betsi et al, 2011). Other dykes in the area include aphanitic to very fine-grained aplite dykes that intrude the Dawson Range batholith at the Revenue granite, but do not crosscut the diatreme (Northern Freegold Resources Ltd, 2017). These dykes are aplitic to granophyric in texture and are composed of quartz and feldspar with minor muscovite and biotite (Bineli-Betsi and Lentz, 2011). Locally at the Revenue occurrence pegmatitic quartz-feldspar dykes and pods occur that may have formed via

magmatic differentiation of the Revenue granite before complete crystallization (Northern Freegold Resources Ltd, 2017).

3.0 Field observations and mineralization

During the 2017 and 2018 drill programs, the location of the three aforementioned mineralization types were delineated in the southeast area of the Revenue property by on-site geologists (Fig. 3A). In this region the Revenue granite host rock is a biotite-K-spar monzogranite with K-spar porphyrocrysts, and contains rare pyrite-calcite stringers. Within the Revenue granite, a SW-NE-oriented mineralized body (herein termed the "Blue Sky Zone" or "BSZ") contains zoned mineralization and alteration. The BSZ hosts the first style of mineralization (*style 1*) which is further divided into i) early quartz-sulfide veins and vein stockwork (early *style 1*) associated with intense potassic (biotite) alteration (Fig. 3B) and ii) late quartz-carbonate-sulfide veins and vein stockwork (late *style 1*) associated with phyllic alteration that cross-cuts early *style 1* mineralization, and is located in the northeast region of the Revenue granite (Figs. 3A,B).

In the Revenue granite, a breccia (herein termed the "WAu" breccia) consisting of angular clasts of the Revenue granite and fragments of QFP dykes in a quartz-sulfide matrix, with localized areas of massive sulfide or sulfide-carbonate matrix, near the south-east edge of the Revenue diatreme (Fig. 3). This breccia body has been This breccia hosts the second style of mineralization (*style 2*) comprising of sulfides and tungstates in the interstices to rock fragments.

The third style of mineralization (*style 3;* sulfide replacement) is hosted in the Revenue diatreme, interpreted to belong to the Casino suite and dated to 77 - 75 Ma (Friend et al., 2018) and crosscuts Revenue granite (Figs. 3A,B). The Revenue diatreme is

composed of subvolcanic rock with a porphyritic texture of quartz and feldspar crystals in an aphanitic to visibly fine-grained, light grey groundmass. Local hydrothermal breccias overprint the diatreme within 30 meters of the diatreme margins, and sulfides occur interstitial to rounded diatreme fragments.

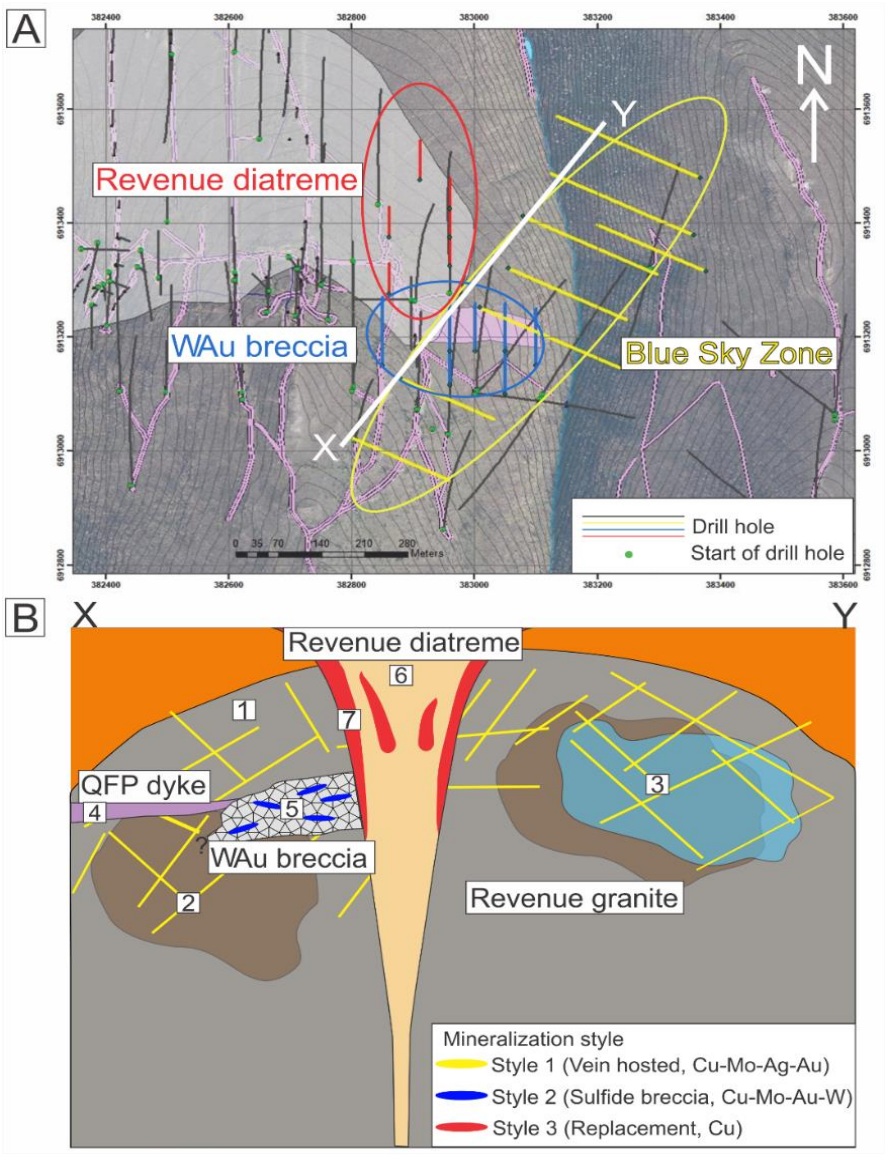

Figure 3. Aerial view and conceptual diagram of the Revenue mineral occurrence. A) Aerial view of the defined mineralized occurrences at the eastern Revenue property. The elongated yellow ellipse represents the general boundaries of the Blue Sky Zone (BSZ), with the early style 1 mineralization occurring in the SW end and the late style 1 mineralization occurring NE. The WAu breccia, outlined in blue, crosscuts the BSZ. The Revenue diatreme mineralization, outlined in red, occurs near the contact of the diatreme body and the surrounding host rocks. This diatreme overhangs the WAu breccia as the body of the diatreme is dipping WNW (T. Barresi, communication, 2018). A transect X-Y shows the location of image B. B) Corresponding conceptual schematic of transect X-Y based on current information, adapted from internal publications of Triumph Gold Corp. (2018). Styles of mineralization correspond to spatial zones shown in A. Also shown are QFP dykes, which are pre- to syn- WAu Breccia. The brown patches represent biotite alteration in the BSZ. The blue patch represents phyllic alteration of the BSZ. The boxes are labelled one through seven and represent areas of sample collection, with some areas representing multiple samples, see section 5.1. Not drawn to scale.

4.0 Field and analytical methods

4.1 Sampling

Thirty-two samples of drill core were collected from seven drill holes. These samples are representative of key host rock types, mineralization and/or alteration styles (Table 1; see Fig. 3 for sample locations). Samples were cut into blocks at Saint Mary's University and sent to Vancouver Petrographics Ltd. for preparation of polished thin sections (26 x 46 mm; 30 μm thick). Of these, 14 thin sections were further deemed representative of mineralization styles and underwent detailed petrographic analysis (see section 5.1).

Table 1. Sample descriptions including mineralization type, location, alteration, and assay data.

Host Rock	Sample	Drill Hole	Depth (m)	Representative Area	Mineralization style	Assays (ppm)	Mineralization and alteration
Revenue granite	RG-1	RVD17-01	157.55 - 157.58	Least altered granite	Barren	0.041 Au, 169 Cu, 0 Mo	Disseminated sulfides, occasional carbonate-sulfide veinlets in weak phyllic alteration.
	E-BSZ-1	RVD17-12	405.69 - 405.78	SW Blue Sky Zone	Early style 1	0.024 Au, 211 Cu, 2 Mo	Sulfide stringers along biotite veins and quartz veins. Biotite veins are crosscut by quartz veins.
	E-BSZ-2	RVD17-12	405.96 - 405.99	SW Blue Sky Zone	Early style 1	0.09 Au, 334 Cu, 35 Mo	Disseminated sulfides in a dense biotite stockwork.
	L-BSZ-1	RVD17-13	126.54 - 126.585	NE Blue Sky Zone	Late style 1	0.45 Au, 4300 Cu, 224 Mo	Phyllic altered granite with sulfide stringers crosscut and offset by quartz-sulfide veins, occasional quartz-sulfide±molybdenite veins.
	L-BSZ-2	RVD17-13	180.65 - 180.70	NE Blue Sky Zone	Late style 1	0.024 Au, 220 Cu, 1 Mo	Phyllic altered granite carbonate-quartz-sulfide vein with chlorite and K-feldspar halo, crosscutting pyrite stringers.
	L-BSZ-3	RVD17-13	186.205 - 186.235	NE Blue Sky Zone	Late style 1	0.101 Au, 188 Cu, 11 Mo	Dense potassic altered area near aplite dyke with barren quartz veins and biotite selvages cross-cut by quartz-sulfide veins.
	WAu-1	RVD11-028	231.92 - 231.955	Quartz-sulfide breccia	Style 2	0.184 Au, 1485 Cu, 2110 Mo	Phyllic altered breccia with coarse-grained aggregates of chalcopyrite-pyrite in quartz matrix.
	WAu-2	RVD11-028	212.105 - 212.13	Quartz-sulfide breccia	Style 2	0.479 Au, 2970 Cu, 3340 Mo	Localized area of massive chalcopyrite-pyrite-molybdenite matrix in breccia. Molybdenite mantles granite fragments and anhedral grains of scheelite-ferberite occur in the matrix.
	WAu-3	RVD11-028	244.32 - 244.35	Massive sulfide breccia	Style 2	0.368 Au, 1795 Cu, 669 Mo	Fe-carbonate-altered fragments of granite and QFP with barren quartz veins crosscutting the clast of QFP. Fine-grained pyrite-quartz-chalcopyrite matrix, molybdenite disseminated and mantling rock fragments. Ocassional subhedral to anhedral black sphalerite.
	WAu-4	RVD11-028	241.57 - 241.605	Sulfide-carbonate breccia	Style 2	2.01 Au, 14500 Cu, 1060 Mo	Localized area of massive galena blades in a Fe-carboante altered matrix within breccia.
Revenue diatreme	RD-1	RVD17-10	98.17 - 98.21	Least altered diatreme rock	Barren	0.059 Au, 209 Cu, 27 Mo	Phyllic altered, cement-beige matrix with feldspar and quartz clasts and disseminated sulfide.
	RD-2	RVD17-10	348.38 - 348.41	Near diatreme-granite contact	Style 3	0.268 Au, 612 Cu, 80 Mo	Phyllic altered diatreme-fragmented breccia with replacement texure sulfides. Located ~5 m from contact with granite.
Quartz-feldspar porphyry dykes	QFP-1	RVD17-12	60.52 - 60.56	Least altered dyke	Barren	0.101 Au, 918 Cu, 71 Mo	Medium grey-tan coloured matrix with phenocrysts (~0.1 - 0.5 cm) of weakly altered feldspars and disseminated sulfide.
	QFP-2	RVD17-01	332.05 - 332.08	Phyllic altered dyke	Barren	0.141 Au, 1040 Cu, 195 Mo	Phyllic altered dyke with a zoned feldspar phenocryst, including pyrite grains. Disseminated sulfides in the matrix.

4.2 Petrography

Mineral identification and textural analysis was done using a petrographic microscope in transmitted and reflected light, in conjunction with the use of photomicrograph capture software. High resolution imaging and mineral identification of optically-ambiguous phases, and semi-quantitative analysis of major and minor elements in minerals was done using SEM back-scattered electron (BSE) imaging and energy dispersive spectroscopy (EDS), respectively. The instrument used was a TESCAN MIRA 3 LMU VPS Field Emission Scanning Electron Microscope (SEM), equipped with an energy dispersive X-ray (EDS) Oxford INCA 80 mm^2 silicon drift detector (SDD) capable of near-quantitative analysis (Saint Mary's University, Halifax, Nova Scotia). The accelerating voltage was set at 20 kV, working distance to 17 mm, and EDS specta acquisition times to 30 seconds. The exception was sphalerite for which spectra were collected for 2 minutes to resolve minor concentrations of Cd, In, and Sn. Data reduction was done using INCA software. Compositional data reported for minerals is expressed in weight percent of all elements for sulfide, tungstate, and ore minerals and weight percent of oxides for silicates, oxides, carbonates and phosphate minerals with a detection limit of > 0.1 wt%. Data was adjusted for carbon in carbonates as the carbon-coating on slides resulted in an overestimation of carbon content.

4.3 Electron microprobe analysis (EMPA)

The composition of sulfide and sulfarsenide minerals was determined for the purpose of constraining mineralization conditions using well-established thermobarometers. This required wavelength dispersive spectrometry using an electron

microprobe analyser (EMPA). Analyses of the sulfarsenide glaucodot ($(Co_{0.75},Fe_{0.25})AsS$) (n = 11) were performed on a JEOL JXA8200 electron microprobe at Dalhousie University, Halifax, Nova Scotia, using a focused beam operating at an accelerating voltage of 15 kV, a beam current of 20 nA, with a spot size of 1 µm. Counting times for analyses were 10s on each background and 20s on peaks. Samples were analyzed for S, Fe, Co, Ni, Zn, As, Cu, Pb, and Si using the following standards to calibrate sensitives and for peak positioning: pyrite (S), pyrrhotite (Po), cobaltite (Co), pentlandite (Ni), sphalerite (Zn), arsenopyrite (As), chalcopyrite (Cu), galena (Pb), and sanidine (Si).

Analyses of sphalerite (n = 24), pyrite (n = 48), and pyrrhotite (n = 6), chalcopyrite (n = 6), and arsenopyrite (n = 21) were obtained using a JEOL JXA8230 EMPA at University of Toronto, Toronto, Ontario. For sphalerite, pyrite, pyrrhotite and chalcopyrite, analyses were performed at an accelerating voltage of 20 kV, a beam current of 20 nA, and a spot size of 1 µm. For pyrite-arsenopyrite pairs an accelerating voltage of 15kV was used, together with a beam current of 5nA, and a spot size of 1µm. Spectral counting times were 20s (on-peak) with 10s background (off-peak) for Fe, Cu, Zn, S, and In and 40s (on-peak) with a 20s background (off-peak) for As, Si, Co, Ni, Pb, Sn, and Cd. Standards for calibration and quantification used were synthetic FeS (Fe, Kα), chalcopyrite (Cu; Kα), arsenopyrite (As, Lα), PbZnGlass (Si, Kα), sphalerite (Zn, Kα; S, Kα), cobaltite (Co, Kα), pentlandite1 (Ni, Kα), SnS (Sn, Lα), CdS (Cd, Lα), and In_2Se_3 (In, Lα).

4.4 Laser ablation inductively coupled mass spectrometry (LA-ICP-MS)

Pyrite, pyrrhotite, and chalcopyrite trace element compositions (n = 16, n = 13, n = 9, respectively) were determined by LA-ICP-MS at the University of New Brunswick, Fredericton, New Brunswick. The instrument used was a Resonetics M-50 193 nm Ar-F

Excimer laser system connected via nylon tubing to an Agilent 7700x quadrupole ICP-MS with dual external rotary pumps (McFarlane and Luo, 2012). A Laurin Technic Pty sample cell was used to hold samples and standards. The cell was repeatedly evacuated and backfilled with ultra-pure He between sample exchanges in order to remove all air from the cells before analysis. Measurements involved 30 seconds of gas blank followed by 30 seconds of transient signal of the sulfide using a 24 μm laser spot size, a 3 Hz repetition rate, and a laser power regulated to produce a fluence of ~3 J/cm^2 at the sample surface during ablation. Ablated material was transported in a He carrier gas at a flow rate of 300 mL/min through the cell, mixed with N_2 at 2 mL/min to enhance some analyte sensitivities, and Ar make-up gas at a flow rate of 930 mL/min before arriving at the ICP-torch. Oxide production rate was maintained at < 0.3%. Dwell times for all isotopes was 10 ms with the exception of Ag, Pt, and Pd which were increased to 50 ms. Internal standardization required ideal Fe content of each mineral (30.43 wt% Fe in chalcopyrite, 46.55 wt% Fe in pyrite, 62.33 wt% Fe in pyrrhotite) for quantification. Calibration was done using MASS1 as the standard with NIT610 as a secondary standard. See Appendix 3 for additional isotope and calibration information.

4.5 Semi-quantitative fluid inclusion microthermometry

Fluid inclusions from the WAu breccia and late BSZ areas were used to provide minimum temperatures of mineralization by estimating halite total crystal area in three phased fluid inclusions in order to compare and constrain temperatures obtain from sulfide thermometry methods. This was done using an experimentally determined relationship between halite area and weight percent NaCl equivalent (wt% eqNaCl). Halite area was measured using Image J whereby total fluid inclusion and halite crystal areas were traced

and measured graphically. Uncertainty is up to ±5 area % which reflects inaccuracies in relating halite crystal and inclusion area to halite crystal and inclusion volume for non-isometric, non-spherical shapes. Area % halite measurements were converted into salinities using the equation: NaCl wt% equivalent = $10.903(\text{area \% halite})^{0.4793}$ at 25ºC (J. Hanley, personal communication 2019). Once bulk salinities were estimated the equivalent Ts of halite dissolution were determined using equations of state from Bodnar and Vityk (1995). Total variations of ±35 – 40ºC are associated with this approach, based on area to volume under or overestimations, tracing errors, and volume-salinity conversions.

4.6 Infrared spectroscopy (IR)

Thirteen samples were analyzed using a TerraSpec 3 infrared reflectance spectroscope equipped with a 6.5W, 10 mm, ASD Hi-bright contact probe. Spectra were constructed using ASD RS^3 software. Calibration was conducted using a fluoropolymer "Spectralon" white reference standard to create a reflectance reference for spectral comparison. Spectrum averaging during referencing occurred as 60 readings for the white reference and dark current. A muscovite control standard with a known spectrum was analyzed after calibration and at the end of each sample sequence to ensure the instrument was recording data properly and consistently. Samples were analyzed in 10-minute blocks whereby samples were placed upon a clean, white sheet of paper and were analyzed consecutively three times in three second intervals on one or more surfaces of the sample. Raw data from ASD RS^3 were processed using the ViewSpecPro software. Clay minerals in each sample were identified by comparing absorption bands and hull characteristics in average or ideal spectral features in the ADS spectral library database.

5.0 Results

5.1 Core sample petrography

The following list describes the studied samples and is organized according to host lithology:

i) Revenue granite containing *style 1* mineralization of the Blue Sky Zone (BSZ)

Sample RG-1 was collected near the south-eastern flank of the diatreme and represents the least altered Revenue granite in the area (area 1 of Fig. 3B). It contains quartz-plagioclase-K-feldspar-biotite (Fig. 4A) and shows weak alteration of K-spar to white clays. Disseminated sulfides and rare calcite-sulfide stringers are also present. Samples E-BSZ-1 and E-BSZ-2 were chosen to represent the early *style 1* mineralization of the BSZ stockwork, located ~650 m from late *style 1* mineralization (area 2 on Fig. 3B). These samples contain disseminated sulfides and quartz-sulfide veins with potassic (biotite) altered margins and biotite veins (Figs. 4B,C). Samples L-BSZ-1, L-BSZ-2, and L-BSZ-3 were chosen to represent late *style 1* mineralization of the BSZ. This style of mineralization is associated with quartz-sulfide±carbonate veins and associate phyllic alteration (Fig. 4D) that crosscut and overprint earlier, *style 1* mineralization. Sample L-BSZ-1 is representative of late *style 1* quartz-sulfide veins and associated phyllic overprinting of the wallrock (Fig. 4D). Local pyrite-carbonate stringers also occur in this area and are crosscut by quartz-carbonate-sulfide and quartz-molybdenite veins (Fig. 4D). Samples L-BSZ-2 contains carbonate-quartz-sulfide veins hosted in a phyllic-altered granite (Fig. 4E). L-BSZ-3 is from a strongly biotite-altered granite with quartz-sulfide veins, which crosscut barren quartz veins and aplite plugs in the area (Fig. F). The late *style 1* mineralization is represented by sample area 3 on Figure 3B.

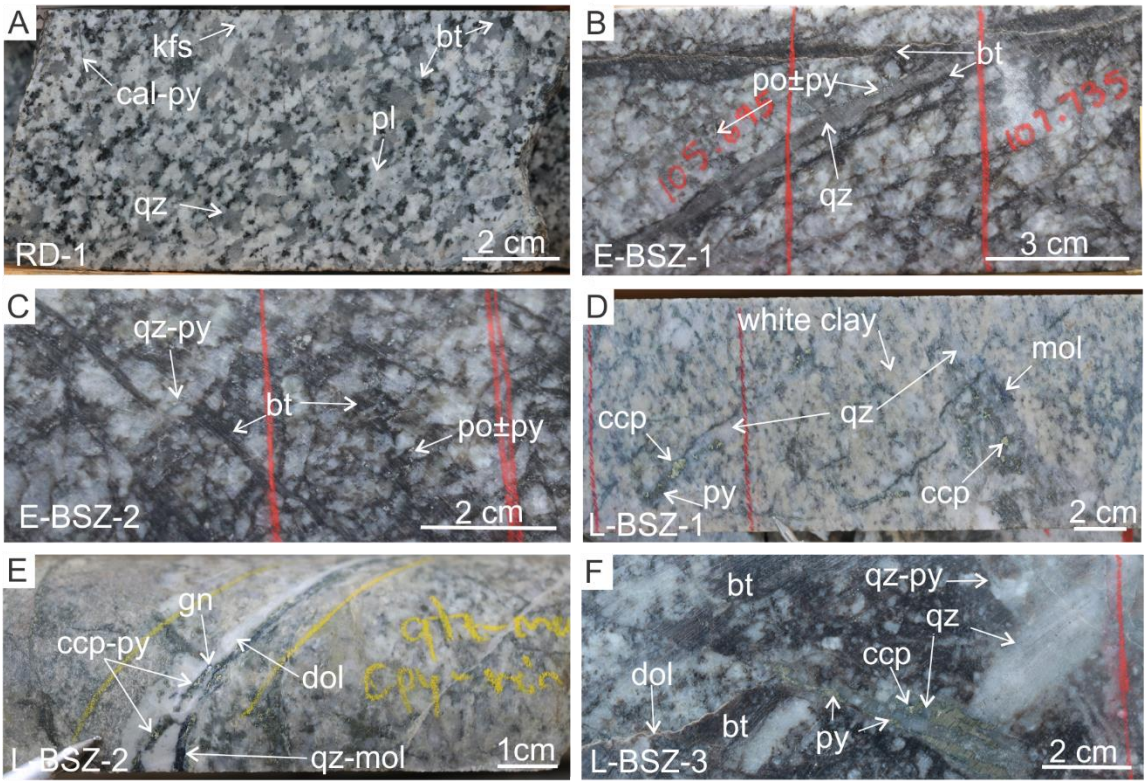

Figure 4. Revenue granite core samples showing representative host rocks and mineralization. A) The Revenue granite, the host rock of the Revenue deposit, crosscut by a calcite-pyrite vein of the Blue Sky Zone style 1 mineralization. B) Early BSZ biotite alteration and stringers with quartz-pyrite veining. C) Early BSZ biotite alteration and disseminated pyrite-pyrrhotite with biotite stringers crosscut by a quartz-pyrite vein. D) Late BSZ with beige phyllic alteration, quartz-chalcopyrite-pyrite veins, quartz-chalcopyrite patches, and quartz-molybdenite-chalcopyrite-pyrite veins. E) Dolomite infilling brecciated chalcopyrite-pyrite-quartz-molybdenite vein in the late BSZ. F) Within the same area of G, dense biotite alteration is crosscut by a barren quartz vein (1 - 2cm), which itself is crosscut and displaced by a quartz-pyrite-chalcopyrite vein (1.5cm). In both G and H, late dolomite stringers cross-cut features parallel to core. Sample numbers are in bottom left-hand corner. See Appendix 1 for list of mineral abbreviations.

ii) Quartz-feldspar porphyry (QFP) dykes

Samples QFP-1 and QFP-2 represent the QFP dykes that crosscut the Revenue granite, Blue Sky Zone, and the WAu breccia. Sample QFP-1 represents the least altered dyke. It is composed of a fine-grained, grey groundmass containing phyllic-altered feldspar phenocrysts (0.2 - 0.7 cm) and quartz eyes (0.2 - 0.5 cm). Dendritic, fine-grained pyrite is disseminated throughout the sample (Fig. 5A). Sample QFP-2 was collected from a QFP dyke that crosscuts the Revenue granite. The dyke is porphyritic with weak phyllic alteration of K-feldspar phenocrysts (0.5 - 1.8 cm) and quartz eyes (0.2 - 0.9 cm) in a groundmass also showing phyllic alteration of feldspar. Mineralization occurs as disseminated pyrite (Fig. 5B). The QFP samples are represented by sample area 4 in Figure 3B.

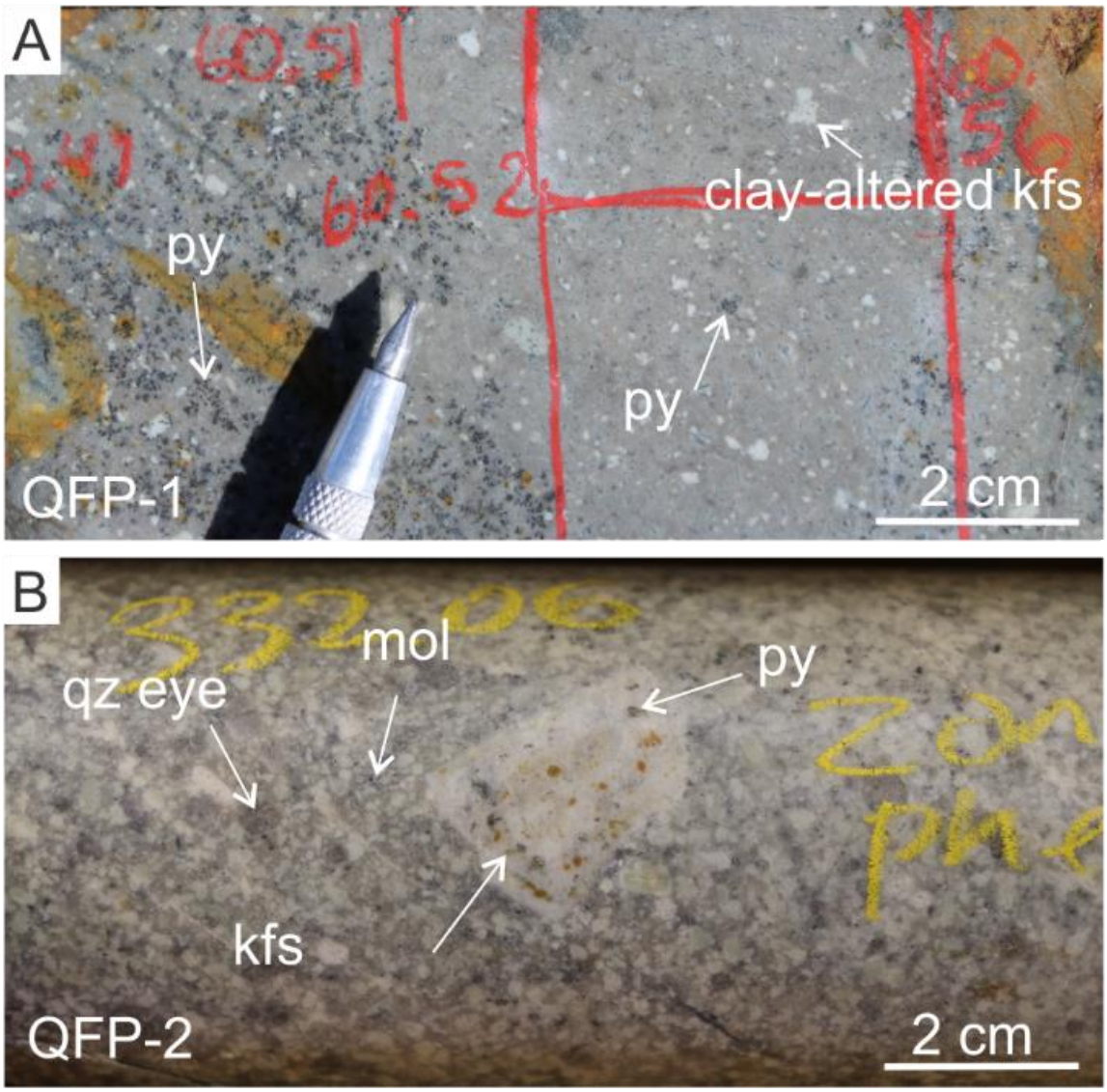

Figure 5. QFP core samples showing representative alteration. A) Grey-tan colored QFP with patches of dendritic pyrite, clay-altered K-feldspar phenocrysts and disseminated, fine-grain pyrite clusters. B) Strongly phyllic-altered QFP, with zoned K-feldspar phenocrysts containing pyrite inclusions and fine-grained molybdenite is disseminated in QFP groundmass. Sample numbers are in bottom left-hand corner.

iii) WAu Breccia

Samples WAu-1, WAu-2, WAu-3, and WAu-4 were collected from variably high grade (1500 to 14500 ppm Cu, 184 to 2010 ppb Au, 23 to 8290 ppm Pb; Table 1) domains of the WAu breccia, and represent *style 2* mineralization. Samples WAu-1, WAu-2, and WAu-3 contain coarse-grained, disseminated sulfides (chalcopyrite, pyrite, molybdenite) in a quartz matrix between clasts (< 10 cm) of phyllic-altered granite (Fig. 6A) and QFP fragments (Fig. 6B). Clasts of QFP may contain earlier, barren quartz veins (Fig. 6B). Sample WAu-4 represents a localized area of the breccia that contains massive sulfide-carbonate matrix comprised of coarse-grained galena with massive pyrrhotite and abundant QFP clasts (Figs. 6C,D). These samples are represented by area 5 in Figure 3B.

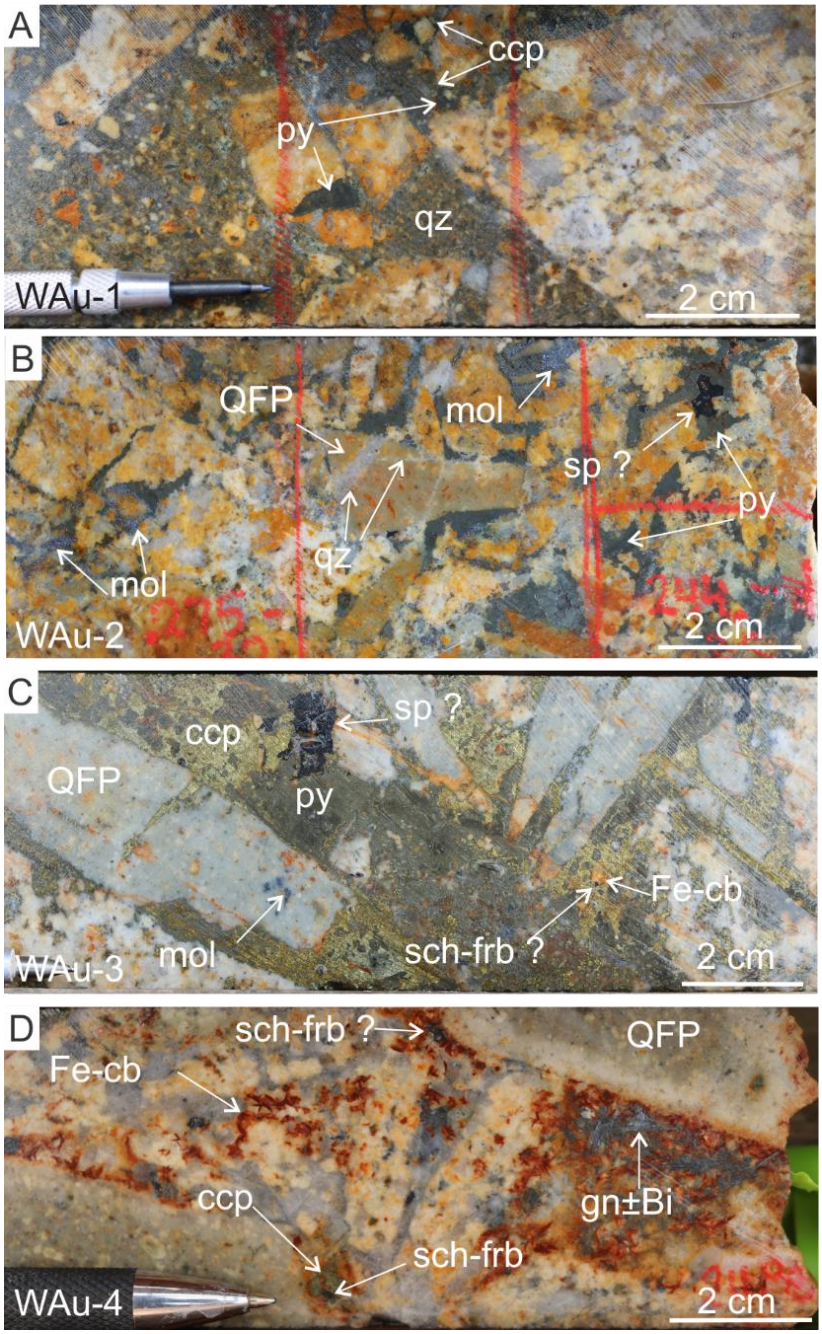

Figure 6. WAu breccia core samples showing representative mineralization. A) Representative WAu breccia quartz-sulfide matrix, with clasts of phyllic altered Revenue granite. Pyrite is fine-grained and occurs in grey-black clots. B) WAu breccia with clasts of phyllic altered QFP and Revenue granite in a matrix of quartz-pyrite-molybdenite-chalcopyrite±sphalerite. A barren quartz vein crosscuts the QFP clast. C) Localized area of WAu breccia containing sulfide matrix, dominantly pyrite-chalcopyrite with larger sphalerite grains. Fe-carbonate locally occurs in the matrix. D) Localized area of massive sulfide matrix comprising of coarse-grained bladed galena, surrounded by feathery textured Fe-carbonate. Chalcopyrite is present and contains inclusions of scheelite-ferberite. QFP clasts have chilled margins. Sample numbers are in bottom left-hand corner.

iv) Revenue diatreme

Two samples, RD-1 and RD-2, where chosen from the mineralization *style 3* location of the Revenue diatreme. Sample RD-1 is representative of the least-altered diatreme, and consists of fine-grained, tan-beige-coloured matrix, containing weakly to moderately phyllic-altered feldspar clasts (< 2.5 cm) (Fig. 7A) and disseminated, euhedral pyrite crystals (Fig. 7A). This sample is represented by sample area 6 in Figure 3B. Sample RD-2 is comprised of brecciated diatreme with strong phyllic alteration, located ~5 meters from the contact with the Revenue granite. This breccia consists of rounded clasts of diatreme material (0.2 - 4.5 cm) with sulfides showing dendritic replacement textures (Fig. 7B), or occurring interstitial to the clasts (Fig. 7C). Samples RD-1 and RD-2 are represented by sample area 7 in Figure 3B.

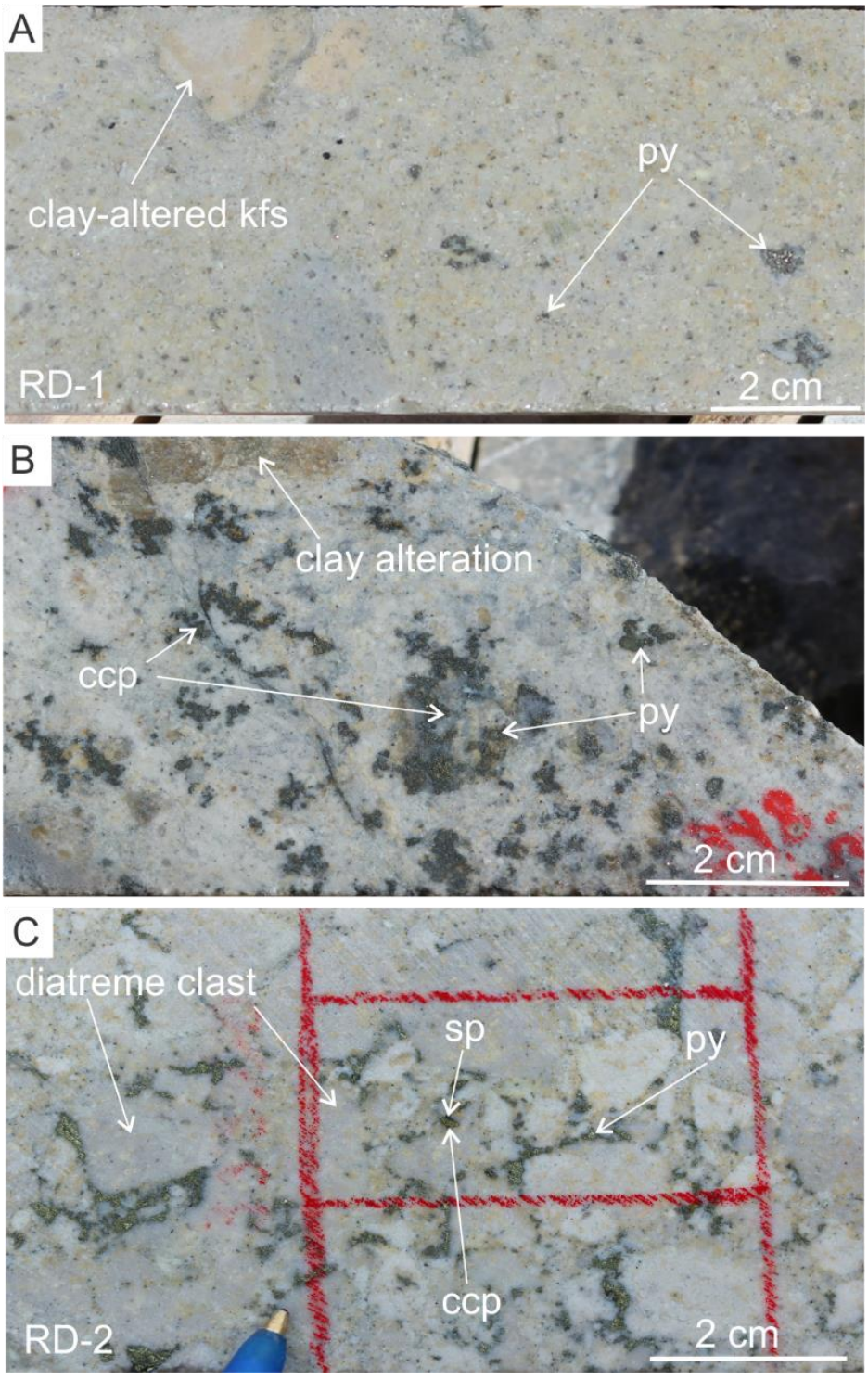

Figure 7. Revenue diatreme core samples showing representative host rocks and mineralization. A) Representative texture of the beige-coloured Revenue Diatreme containing disseminated fine-grained pyrite in sample RD-1. K-feldspar is altered to clay. B) An area ~10 meters from sample RD-2, where chalcopyrite and pyrite occurring as dendrites that replace the diatreme material. C) Chalcopyrite and pyrite with trace sphalerite interstitial to diatreme clasts.

5.2 Thin section petrography

5.2.1 Revenue granite

The least-altered Revenue granite (sample RG-1) is a medium- to coarse-grained, melanocratic monzogranite (Fig 5a). The granite is predominantly comprised of plagioclase (~35 vol%), quartz (25%), K-feldspar (25%), and biotite (15%). Plagioclase (1.4 - 4.3 mm) is pitted and partially altered to fine-grained biotite and clays that measure < 3 μm (Fig. 8A). Quartz (~0.7 - 1.4 mm) occurs as anhedral coarse-grained crystals in polycrystalline patches (< 7 mm) with diffuse grain boundaries (Qtz-(i); Fig. 9A). K-feldspar is phenocrystic (< 1.4 cm) (Fig. 8A), pitted, and weakly altered to fine-grained biotite and clay minerals. Primary biotite laths (< 2.1 mm) are reddish tan in colour and show no consistent orientation (Fig. 8B). Accessory minerals apatite (< 150 μm), allanite (< 35 μm inclusions, < 640 μm crystals), and trace zircon (~50 μm) typically occur interstitial to the major minerals or near potassium alteration.

Sulfide within the granite includes pyrrhotite, chalcopyrite, and pyrite that account for < 1 modal% (0.5% pyrrhotite, 0.1% chalcopyrite, trace pyrite) of the granite. Anhedral pyrrhotite (65 - 320 μm) is disseminated and shares grain boundaries with chalcopyrite (70 - 250 μm) (Fig. 8C,D). Pyrite occurs as trace subhedral disseminated crystals (20 μm), veins, overgrowths on pyrrhotite (Fig. 8E) and masses. Rutile is uncommon in this assemblage, but may occur locally as anhedral blebs (165 μm) with pyrrhotite in K-feldspar or with ilmenite (Fig. 8C). Alteration minerals include fine-grained biotite, chlorite, clay, calcite, and trace titanite. Fine-grained biotite (< 3 - 20 μm) occurs in areas associated with sulfides (Fig 8D). Chlorite occurs as a pseudomorphic alteration of biotite (Fig. 8F,G), as anhedral blebs (15 - 110 μm) disseminated throughout alkali-feldspars, and as laths along

the edges of sulfides in veins. Anhedral rutile (< 50 μm) and titanite (< 10 μm) may form in chlorite-altered biotite grains (Fig. 8F). Calcite (< 5 - 20 μm) is associated with sulfides (Fig G,H) and may mantle massive sulfides in fractures within feldspar and quartz crystals (Fig. 8E).

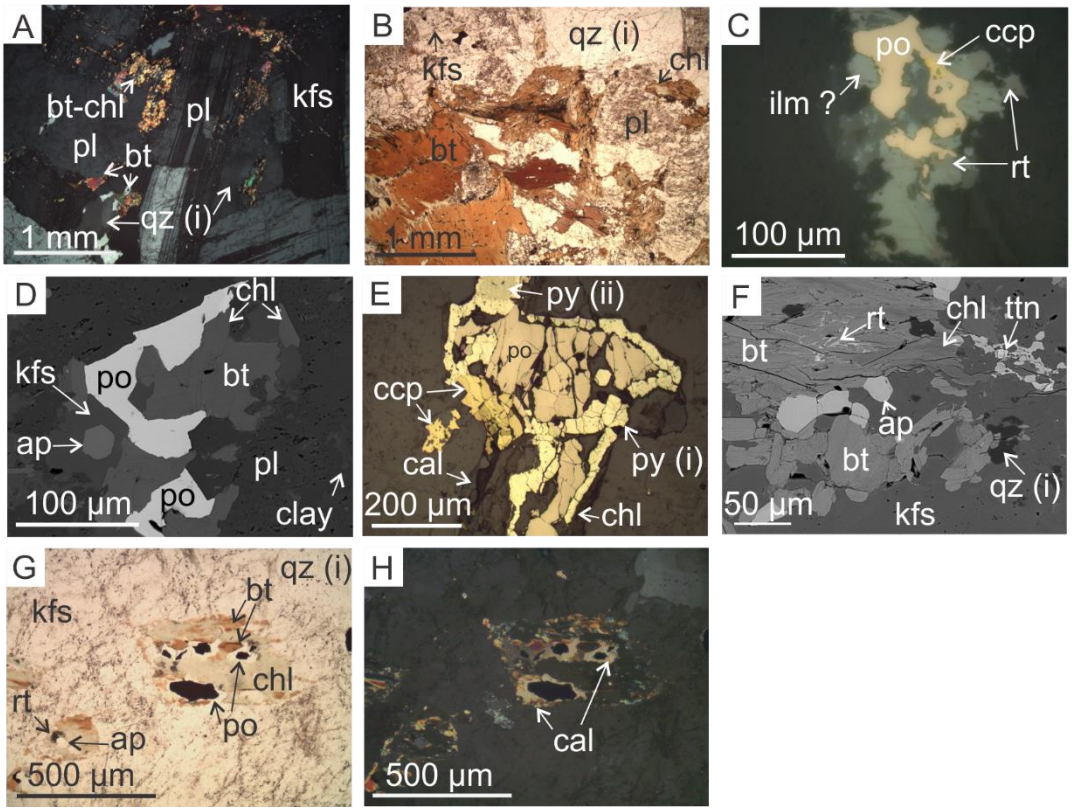

Figure 8. Primary minerals and sulfide mineral assemblages of the least altered granite (sample RG-1). A) Revenue granite plagioclase, K-feldspar, and quartz (i) grains with secondary biotite interstitial, taken by cross-polarized light (XPL). B) Primary biotite laths with no specific orientation. C) A chalcopyrite dissemination partially surrounded by pyrrhotite and altered to rutile-ilmenite taken by reflected light (RL). D) Disseminated pyrrhotite with fine-grained biotite and euhedral apatite. Biotite is altered to chlorite. Image taken by BSE. E) Massive pyrrhotite and chalcopyrite mantled by pyrite and calcite with minor chlorite, taken by RL. F) Mineralization associated alteration of fine-grained biotite and apatite altered to chlorite and rutile, with rare titanite, taken by BSE. G) Primary biotite pseudomorphically altered to chlorite, with pyrrhotite, and rutile, taken by plane-polarized light (PPL). H) XPL image of E showing later calcite surrounding pyrrhotite.

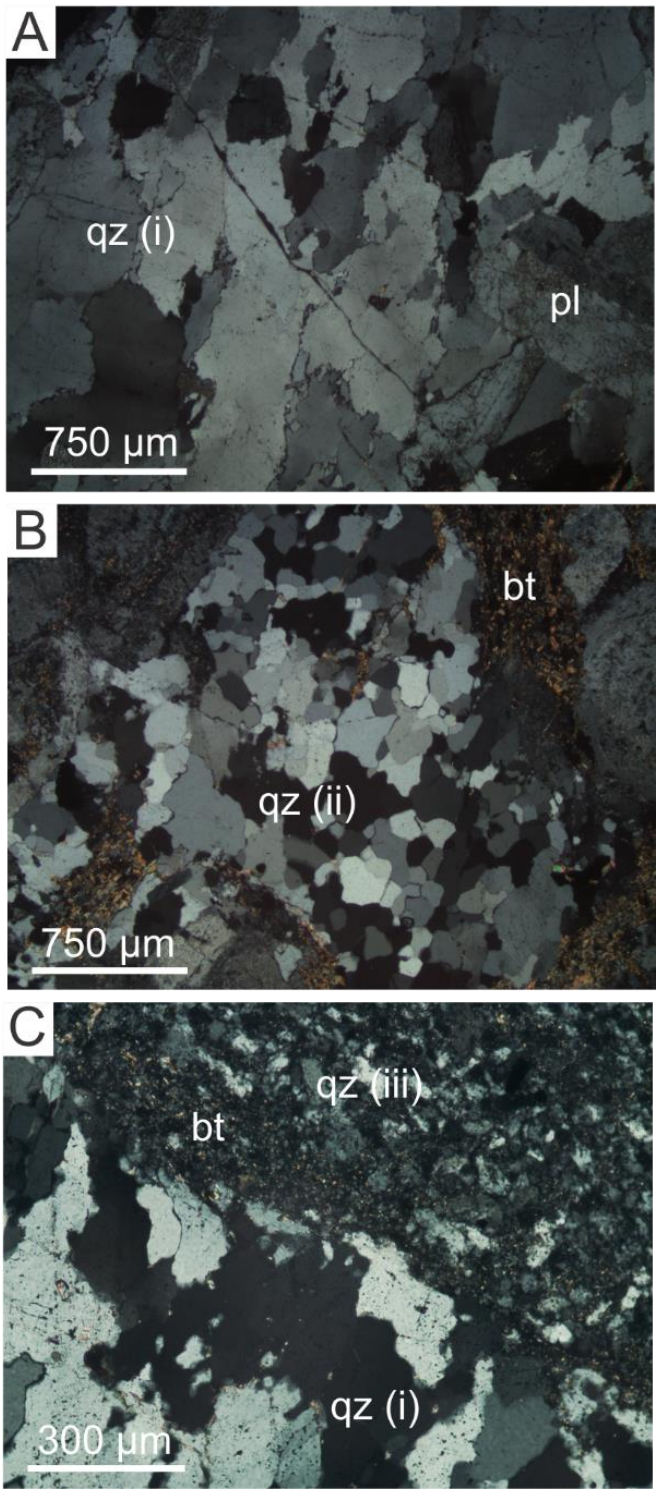

Figure 9. Three texturally distinct quartz generations throughout the Revenue occurrence identified in XPL. A) Sample RG-1 quartz (i), where individual grains show undulose extinction, and grain boundaries are diffuse. B) Sample E-BSZ-2 quartz (ii) as a mosaic texture in cross-polarized light, grains have clear boundaries. C) Sample E-BSZ-1 quartz (iii), where crystals are fine-grained and boundaries are not clear.

5.2.2 Early style 1 mineralization, Blue Sky Zone

Early style 1 mineralization in the Blue Sky Zone is represented by samples E-BSZ-1 and E-BSZ-2. Mineralization is characterized by an assemblage of pyrrhotite, chalcopyrite, pyrite, marcasite, sphalerite and that typically occur along the margins of quartz (ii and iii) veins (Figs. 10A,B), with or without biotite, chlorite, rutile and local calcite (Figs. 10A-C). This mineral assemblage is similar to that of the sulfide associated assemblage in the least-altered Revenue granite; although, the abundance of pyrrhotite, chalcopyrite, rutile, and secondary biotite is greater (2% modal volume at 1.5% pyrrhotite, 0.5% chalcopyrite, trace pyrite and rutile). Additionally, pyrrhotite (50 - 285 μm) is locally altered to marcasite on its grain boundaries, and may contain inclusions of chalcopyrite (35 - 310 μm), pyrite (50 - 320 μm), and fine-grained rutile (~25 - 140 μm) (Figs. 10D-F). Chalcopyrite, and occasionally pyrrhotite, rarely have trace amounts of galena (~15 μm) and sphalerite (~20 μm) inclusions (Fig. 10E). Rutile commonly occurs as disseminated fine-grained patches (< 3 μm grains, 110 - 260 μm patches; Fig. 10E), and may show replacement textures with ilmenite (1.0 mm; Fig. 10G) that contain microinclusions of monazite (< 3 μm). The associated potassic alteration mineral assemblage is similar to that associated with sulfide in the least altered granite (e.g., biotite, chlorite, calcite, rutile), though it occurs as veins with the addition of trace ilmenite and without titanite.

Three distinct texturally generations of quartz occurs in the BSZ (Figs. 9B,C): i) qtz-(i) occurs as described in the pervious section and is relict of the granite host rock, ii) qtz-(ii) occurs as subhedral polycrystalline masses and veins (30 - 185 μm for individual crystals, 0.7 to 1.8 mm for patches) with well defined grain boundaries (Fig. 9B), and iii) anhedral and fine-grained qtz-(iii) (10 - 70 μm) that occurs within veins or on the margin of coarse-grained qtz (i) or qtz (ii) (Fig. 9C).

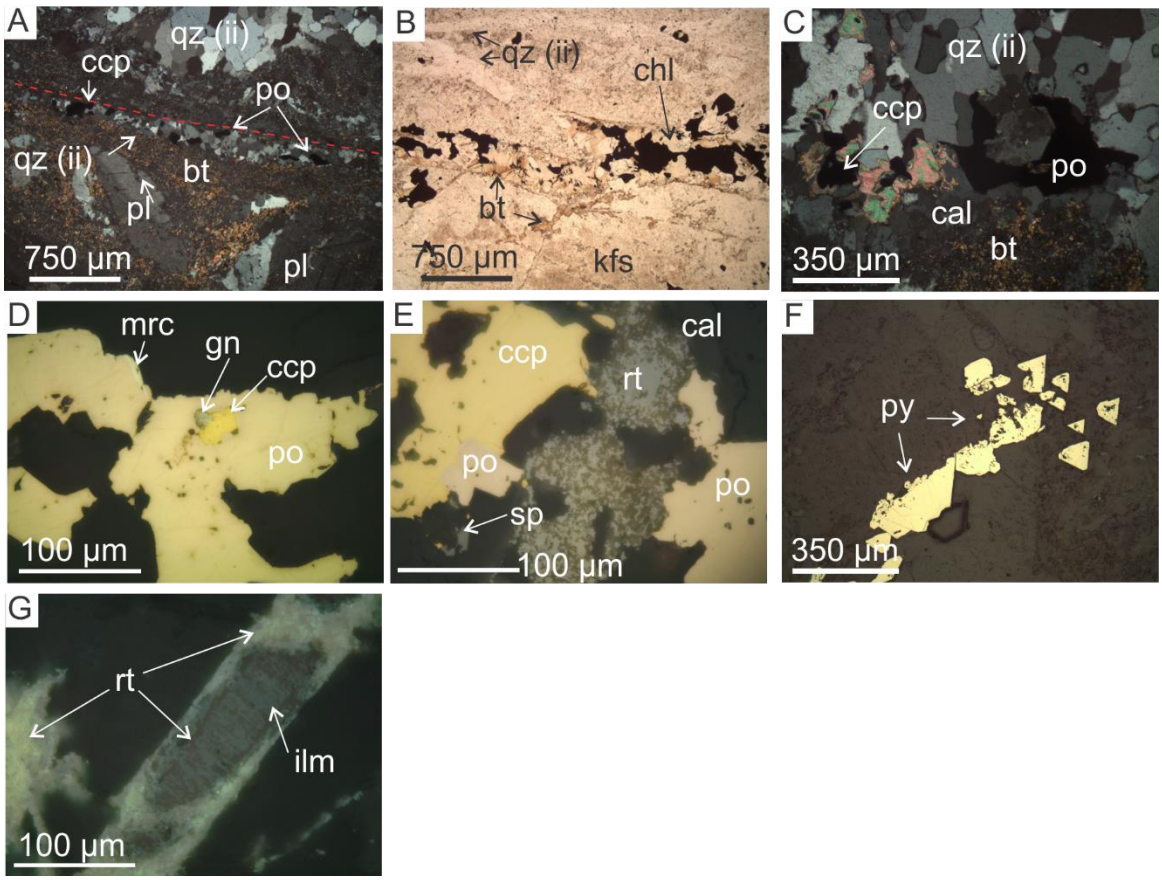

Figure 10. Main mineral assemblages of the BSZ early style 1 mineralization. A) Sample E-BSZ-1;representative mineralized quartz (ii) vein in granite showing fine-grained biotite alteration of feldspar grains at the vein margin (shown as red dashes) in XPL. B) Sample E-BSZ-1; sulfide-quartz-biotite-calcite vein with minor chlorite alteration on biotite. C) Sample E-BSZ-2; late calcite associated with chalcopyrite and pyrrhotite mineralization in quartz (ii) patches in XPL. D) Sample E-BSZ-2; disseminated pyrrhotite with minor marcasite alteration surrounding chalcopyrite and galena. E) Sample E-BSZ-2; pyrrhotite and syn to late chalcopyrite associated with minor sphalerite and anhedral rutile. F) Sample E-BSZ-2; disseminated subhedral pyrite with minor sieve textures. G) Sample E-BSZ-2; ilmenite crystal pseudomorphically altered to rutile.

5.2.3 Late style 1 mineralization, Blue Sky Zone

Late style 1 mineralization in the Blue Sky Zone is represented by samples L-BSZ-1, L-BSZ-2, and L-BSZ-3, and consists predominately of chalcopyrite, pyrite, and molybdenite with minor sphalerite and galena, trace arsenopyrite, Ag-Au, and stannite, and argillic to phyllic alteration characterized by white clays, muscovite and dolomite-siderite. The sulfide minerals are hosted in quartz (ii, iii) veins and dolomite (± quartz) veins (Fig. 11A). Both types of veins contain chalcopyrite and pyrite-marcasite as dominant sulfides (Figs. 10A-D) with molybdenite and subhedral to euhedral rutile (< 200μm) on the margins (Fig. 11B): dolomite veins contain a greater abundance of minor and trace minerals. Two types of pyrite occur in the veins: i) pyrite (i) occurs as smooth to pitted, subhedral to euhedral (< 700 μm) crystals and may surround chalcopyrite (0.15 - 3mm) and occur as inclusions within later pyrite (ii) (Fig. 11C), and ii) pyrite-ii occurs as masses (< 2.5 mm) of fine-grained anhedral grains that may exhibit pitted or coliform textures (Fig. 11C), and occasionally surround pyrite (i) grains. Both types of pyrite show pseudomorphic alteration to marcasite. Siderite (15 - 55 μm width) occurs interstitial to, and mantling, sulfide aggregates (Fig. 11C). Euhedral, lath-like molybdenite (30 - 40 μm) occurs lining, and disseminated within, the dolomite veins and may occur as inclusions within chalcopyrite and pyrite masses and rutile (Fig. 11E). Subhedral apatite grains (< 300 μm) occur disseminated or as inclusions within chalcopyrite in carbonate veins (Fig. 11F). Late stage 1 mineralization crosscuts early style 1 mineralization and potassic alteration, and pyrite-dolomite stringers (Fig. 11F).

The late style 1 mineralization has higher abundances of minor and trace minerals in comparison with early style 1 mineralization. Sphalerite (70 - 115 μm) may occur as anhedral inclusions in pyrite-marcasite or chalcopyrite (< 200 μm), as “X-shaped”

microinclusions in chalcopyrite, and may be enriched in Sn (Fig. 11G; see Appendix 4B). Galena occurs as disseminated inclusions (35 - 320 μm) and may be associated with chalcopyrite (Fig. 11H), arsenopyrite (< 450 μm; Appendix 4B), stannite (15 μm; see Appendix section 9.3.2) in carbonate veins, or interstitial to pyrite (ii) in association with Native Au-Ag (< 5 μm; Appendix 4B). Trace amounts of silver and electrum are found with galena in fractures within pyrite-(i-ii) and as interstitial blebs in masses of pyrite (i)-marcasite (Fig. 11I).

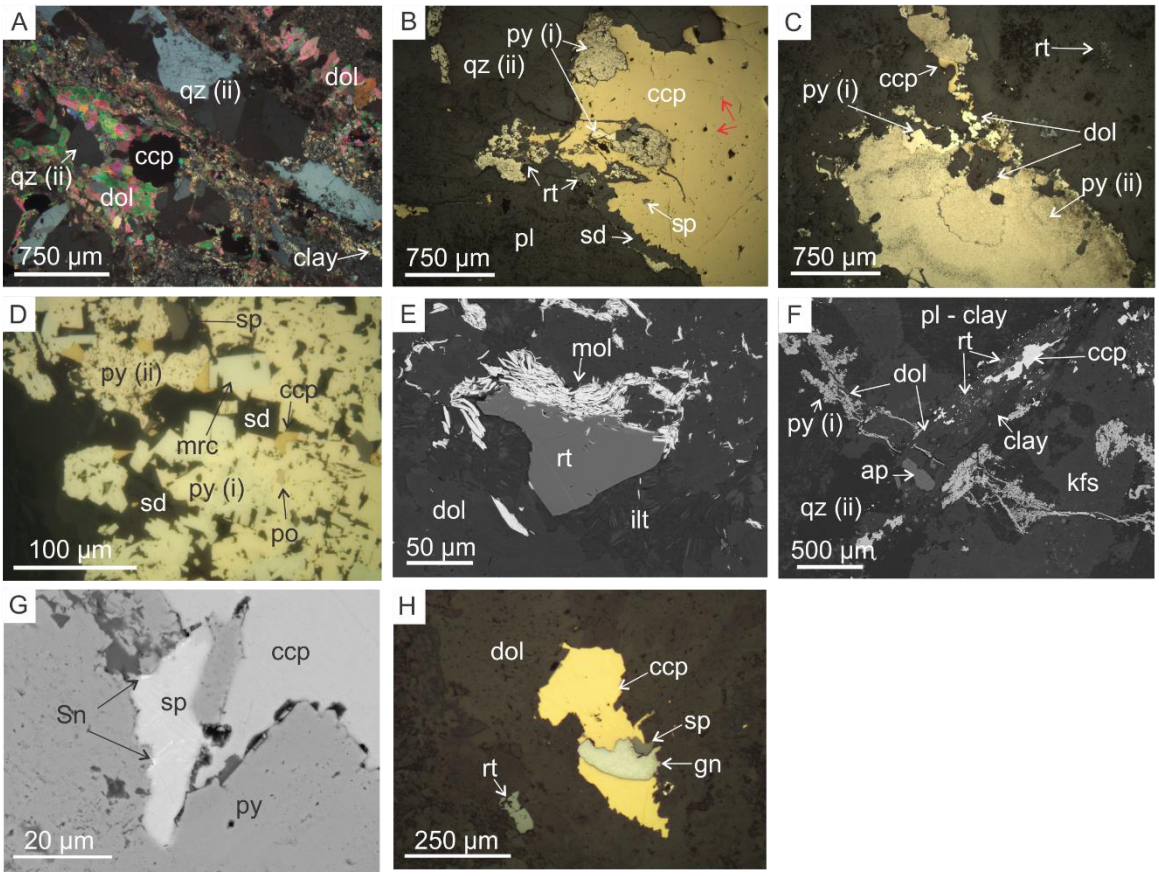

Figure 11. Main and local mineral assemblages of the BSZ late style 1 mineralization. A) Sample L-BSZ-2; XPL photomicrograph of representative dolomite±quartz (ii) veins containing chalcopyrite. B) Sample L-BSZ-1; anhedral chalcopyrite partially surrounding earlier pyrite and rutile. Siderite mantles chalcopyrite, and is in turn mantled by pyrite (i). Red arrows indicate sphalerite inclusions in chalcopyrite. C) Sample L-BSZ-3; fine-grained pyrite (ii) showing colliform texture in quartz-dolomite vein with early smooth textured pyrite (i), chalcopyrite, and disseminated rutile. D) Fine-grained pyrite (i) and anhedral pyrite (ii) altered to marcasite with trace pyrrhotite inclusions. Chalcopyrite and sphalerite occur interstitially to pyrite. E) BSE image of molybdenite mantling rutile on vein margins. F) BSE image of pyrite-dolomite stringer (NW-SE) cross-cut by dolomite-chalcopyrite-apatite-rutile vein (SW-NE). G) BSE image of Sn-enriched sphalerite inclusions occurring within in pyrite. H) Disseminated chalcopyrite, containing early sphalerite and galena within dolomite and with anhedral rutile.

Associated phyllic-argillic alteration includes white clays, determined to be dominantly illite (< 50 μm) and lesser muscovite (< 125 μm) via TerraSpec® and petrography (Appendix 4B), and carbonate patches of fine-grained anhedral dolomite replaced by subhedral and local zoned siderite (< 25 μm) (Figs. 12A,B). Fine-grained (5 μm) rutile needles or euhedral Sn-enriched rutile (Fig. 12A) and rarely fractured pyrite grains (~150 μm) locally occurs in this alteration assemblage. Earlier apatite crystals (< 50 μm) are rounded, whereas later apatite crystals (< 35 μm) are euhedral (Figs. 12A,B). This alteration assemblage shows textural evidence of overprinting the K-alteration assemblage from early mineralization as remnant apatite, chlorite and euhedral rutile are concentrated phyllic alteration areas (Fig. 12B) where white clay pseudomorphically replaces chlorite and "digests" apatite (Fig. 11C).

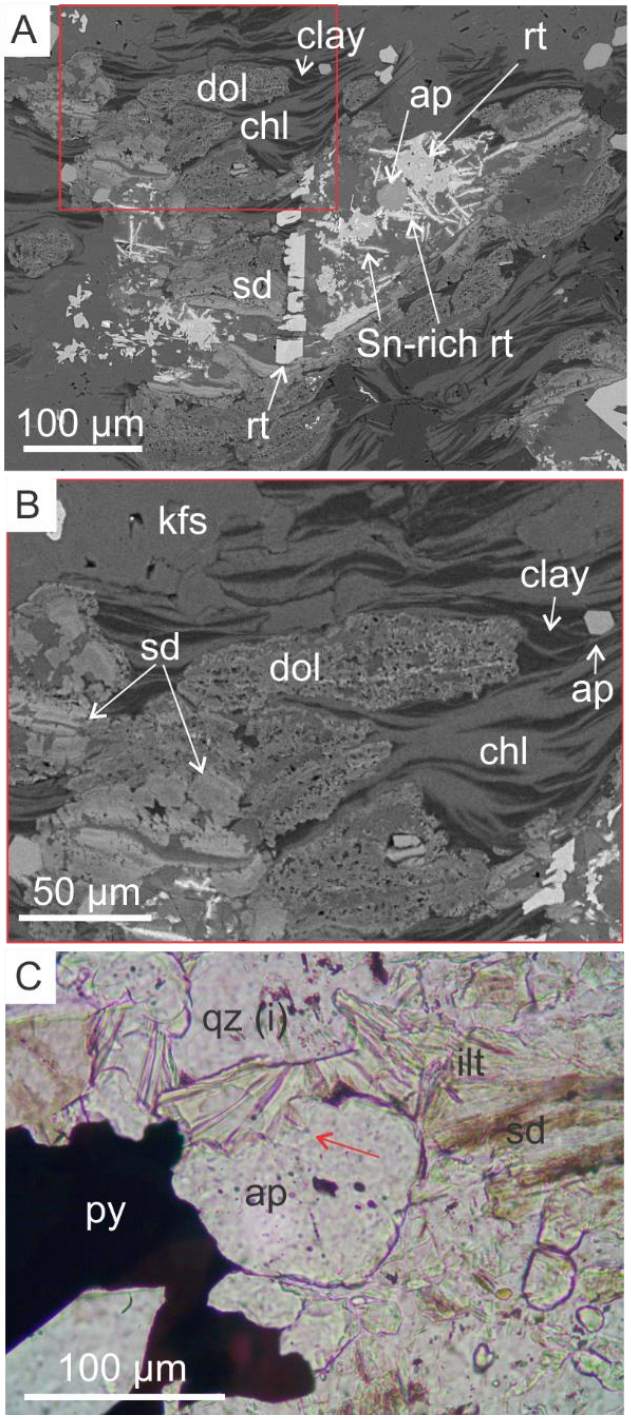

Figure 12. Alteration assemblage associated with late style 1 mineralization. A) Sample L-BSZ-2; BSE image of associated phyllic alteration, showing euhedral rutile textural decomposition, acicular rutile with Sn-enrichment, and both euhedral and rounded apatite. Earlier apatite crystals are rounded, whereas later apatite crystals are euhedral. B) Red inset of A, where chlorite is altered to illite/white clays. Anhedral and partially zoned dolomite is altered to pseudo-cubic and zoned siderite. F) Sample L-BSZ-1; rounded apatite crystal is partially surrounded by pyrite and further digested by clays (indicated by red arrow).

5.2.4 Quartz-feldspar porphyry dykes

Quartz-feldspar porphyry (QFP) dykes are represented by samples QFP-1 and QFP-2. They have a matrix comprising fine-grained quartz-plagioclase with phenocrystic fragments of plagioclase and quartz (i, ii). Plagioclase crystals (0.25 - 2 mm), typically oligoclase, are pitted and strongly altered by white clays (Fig. 13A), which may occur as inclusions within K-feldspar phenocrysts (< 1.7cm) (Fig. 13A). Round, monocrystic "quartz eye" grains (~450 µm - 2 mm) are commonly disseminated throughout groundmass.

Relatively unaltered QFP (QFP-1) contains a disseminated sulfide mineral assemblage of predominantly pyrrhotite (25 - 350 µm) that may contain inclusions of pyrite-marcasite (50 to 175 µm), anhedral rutile (60 - 140 µm), and chalcopyrite (25 - 175 µm) (Fig. 13B). Chalcopyrite occurs in equilibrium with trace amounts of sphalerite. These pyrrhotite-chalcopyrite-rutile clusters are often associated with a halo of quartz (ii), anhedral calcite (20 - 50 µm), and fine-grained biotite grains (< 55 µm) that pseudomorphically altered to chlorite and rutile (Fig. 13C).

Phyllic altered QFP (QFP-2) mineralization is dominantly disseminated, coarse-grained subhedral pitted grains pyrite (> 450 µm) that contain inclusions of pyrrhotite (< 10 µm; Fig. 13D). Quartz (ii)-dolomite veins (Figs. 13E,F), similar to those of the late stage 1, containing molybdenite (40 - 120 µm) with subhedral rutile (< 5 - 70 µm), chalcopyrite, and subhedral apatite (10 - 100 µm), from the BSZ mineral assemblage were also observed. This mineral assemblage also occurs disseminated throughout the matrix. In altered K-feldspar phenocrysts, pyrite occurs as anhedral masses (30 - 350µm) that are mantled by subhedral to euhedral arsenopyrite (< 5 µm) (Fig. 13G) and associated with Fe-dolomite (< 400 µm) and chalcopyrite (< 100 µm). The associated alteration assemblage includes Fe-

dolomite, which occurs as patches (750 μm) with fibrous white clays on the edges (Fig 13E), or as fine-grained, “dirty” texture when lining quartz-ii veinlets (Figs. 13H,I).

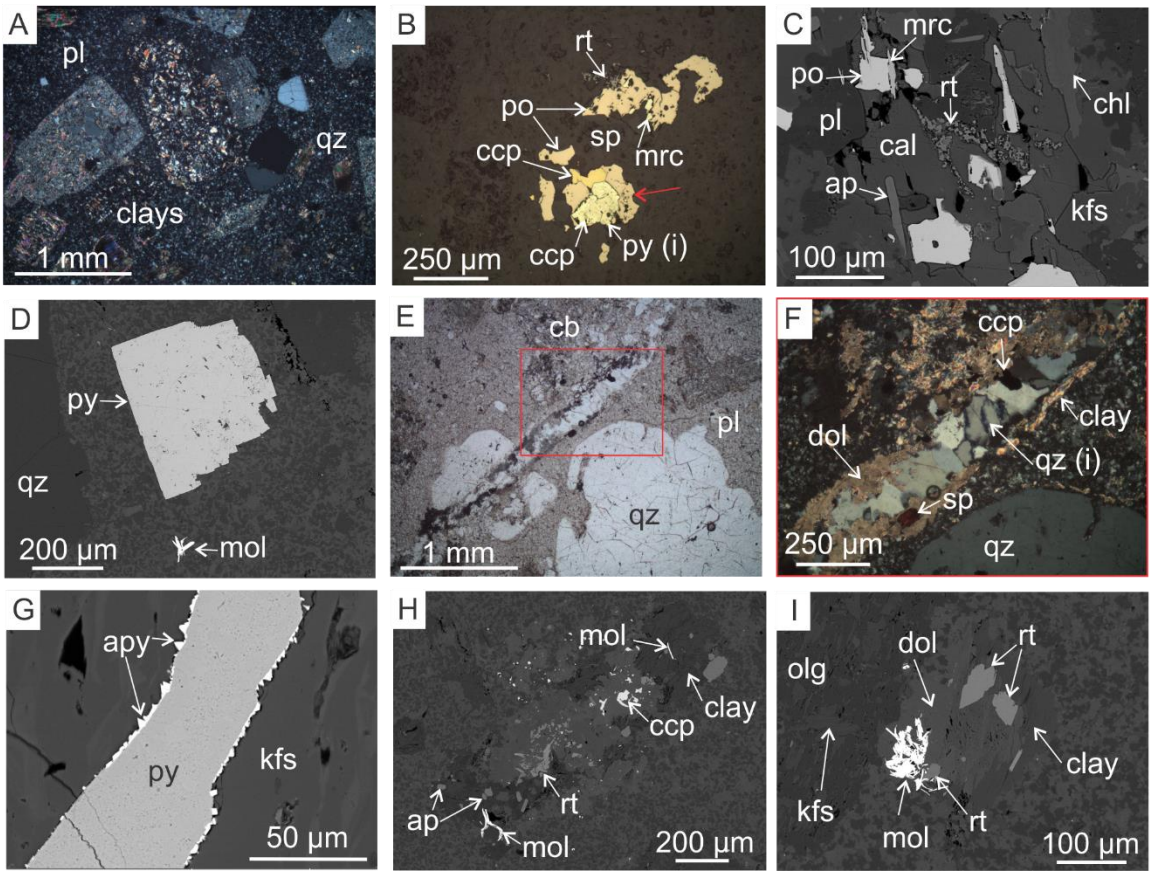

Figure 13. Mineralization of the QFP dykes. A) Cross polarized, representative image of clay-altered feldspars grains in least-altered QFP groundmass. B) Disseminated mineralization where early pyrite (i) is partially surrounded by pyrrhotite and chalcopyrite with trace sphalerite in the least-altered QFP. Anhedral, fine-grained rutile may occur near edges. Marcasite alters the edges of pyrrhotite or earlier pyrite. C) BSE image of disseminated pyrrhotite with marcasite alteration, associated with calcite, fine-grained rutile, chlorite, and apatite in the least-altered QFP. D) BSE image of subhedral cubic pyrite and molybdenite grains disseminated within the phyllic-altered QFP. E) Quartz-carbonate-sulfide veining in the phyllic-altered QFP crosscutting a quartz-eye. F) Red inset of E, where quartz (i-ii) is overprinted by fine-grained dolomite and clays on the margins. G) BSE image of euhedral arsenopyrite overgrowths on pyrite within a K-feldspar grain. H) BSE image of apatite associated with chalcopyrite, molybdenite, and rutile. I) BSE image of early rutile overprinted by molybdenite in a carbonate alteration patch.

5.2.5 Style 2 mineralization, WAu breccia

The WAu breccia, which hosts style 2 mineralization, is a breccia containing a variable matrix from quartz- to sulfide- dominate with local carbonate supporting angular clasts of granite and QFP. Mineralization style 2 is mineralogically complex, containing pyrite (i,ii), chalcopyrite, molybdenite, with local scheelite-ferberite, pyrrhotite, galena±Bi, and electrum, and is commonly associated with phyllic and siderite-rutile alteration. In the quartz matrix, mineralization typically includes sub to euhedral pyrite (i) grains (10 - ~125 μm), chalcopyrite (0.04 - 2.5 mm) and fine-grained pyrite (ii) (Fig. 14A). Chalcopyrite occurs as inclusions (~70 μm) within the pyrite (i,ii), interstitial (3 - 20 μm) to pyrite (i), or along the margins of breccia clasts (Fig. 13a). Pyrite (ii) typically has a coliform texture with sub to euhedral pyrite (i) crystals on its margin (5 - 50 μm) (Fig. 14A). Molybdenite laths (< 140 μm), may occur as inclusions within chalcopyrite and pyrite (ii) (Figs. 14A,B). Trace glaucodot (5 - 30 μm width) lines the edges of these fine-grained pyrite (ii)-siderite masses (Fig. 14B). Chalcopyrite (10 - 30 μm), molybdenite (10 - 25 μm), anhedral to subhedral W-zoned rutile (~30 μm), and local anhedral sphalerite (~15 μm) occur as disseminated grains in the quartz matrix and in localized areas of carbonate matrix (Fig. 14C). These minerals may be disseminated as individual crystals or as clusters in the quartz matrix.

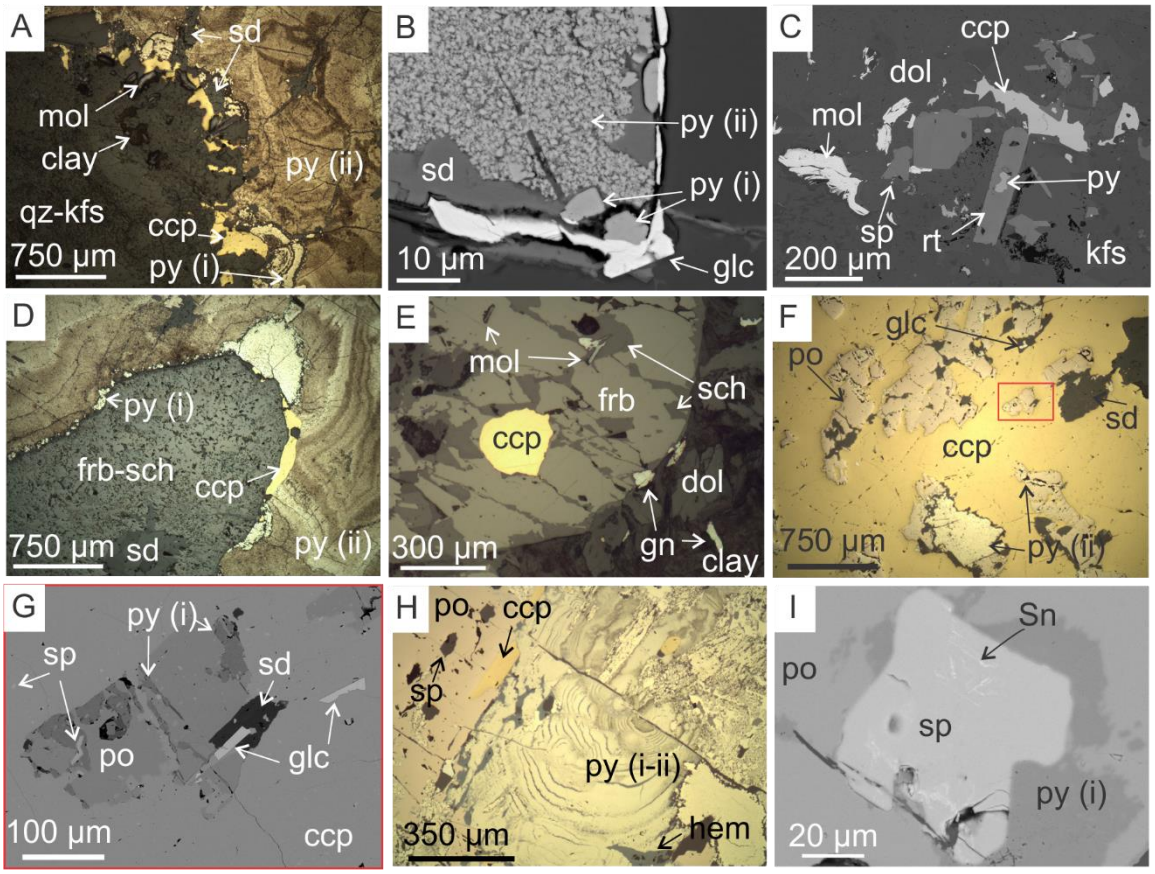

Figure 14. Main and local mineral assemblages of the WAu breccia style 2 mineralization. A) Colloform pyrite (ii) that partially or completely surrounds pyrite (i), chalcopyrite, and molybdenite. B) BSE image of pyrite (ii) aggregate with interstitial siderite and larger euhedral pyrite (i) on edges, later rimmed by glaucodot. C) SEM image of disseminated molybdenite, chalcopyrite, sphalerite, and rutile ± pyrite in a dolomite-siderite and K-feldspar matrix. D) Massive ferberite-scheelite infilled by siderite and mantled by chalcopyrite, pyrite (i) and late coliform pyrite (ii). E) Early ferberite "islands" showing replacement by scheelite. Chalcopyrite, molybdenite and galena grains occur as inclusions in ferbite. F) Local massive chalcopyrite with pyrrhotite, pyrite, and minor glaucodot inclusions and interstitial siderite. G) BSE image of red inset in F showing euhedral glaucodot and small sphalerite inclusions in chalcopyrite and pyrrhotite. Pyrite infills fractures in pyrrhotite masses. H) Massive pyrrhotite, with sphalerite inclusions, adjacent to massive open-space filling pyrite (ii). Hematite and siderite occur in interstitial spaces. I) Subhedral sphalerite with Sn enrichments adjacent to pyrite (i) and pyrrhotite, occurring in same region of image 13H.

In local areas, massive sulfides dominate the matrix with local masses of dark grey coloured Fe-rich tungstate minerals (1.4 - 2.8 mm). The tungstate includes patches of anhedral to subhedral ferberite crystals (< 50 μm) that are replaced by scheelite (Figs. 14D,E). Smaller anhedral grains of chalcopyrite (35 to 140 μm), euhedral quartz grains (40 μm), fine-grained molybdenite (~30 μm) and galena (~40 μm) may occur as inclusions within the ferberite-scheelite aggregates (Figs. 14E,F). Euhedral siderite (15 - 40 μm) infills voids (Fig. 14E). The tungstate may be partially mantled by chalcopyrite and siderite with minor amounts of sphalerite (8 - 170 μm), and further surrounded by pyrite (ii) and pyrite (ii) masses (Fig. 14D).

Locally, the sulfide matrix in the sulfide breccia is dominated by anhedral chalcopyrite (< 2.5 cm) with inclusions of pyrrhotite (140 - 830 μm), rarely pyrite (< 615 μm), associated with siderite (40 - 260 μm; Fig. 14F). Chalcopyrite and pyrrhotite contain inclusions of euhedral grains of glaucodot (15 - 85 μm) and anhedral sphalerite (5 - 50 μm) (Figs. 14F,G). Pyrrhotite clots may contain inclusions of pyrite and rutile fracture infills (~5 μm in width) (Fig. 14G). This assemblage is spatially adjacent to areas of massive, open-space textured pyrite (i) (~2.1 mm) and massive pyrrhotite (70 - 885 μm) with inclusions of chalcopyrite (35 - 215 μm) and occasionally Sn-rich sphalerite (< 65 μm) (Fig. 14H). Hexagonal to acicular hematite (35 - 85 μm) forms in between bands and grains of pyrite with siderite infilling the remaining space (see Appendix 4D). Trace assemblage of uraninite-zircon-barite-rutile-pyrite occur in areas of the K-feldspar-carbonate-quartz matrix (see Appendix 4D).

In other localized areas within the sulfide breccia, coarse-grained galena blades ± Bi-Te (75 - 780 μm) occur with native Au (400 μm) and local calcite (Figs. 15A,B). Euhedral red sphalerite (~80 μm) containing chalcopyrite inclusions occurs interstitial

galena blades and coarse-grained white clays (~150 μm) surround the aggregate of minerals (Fig. 15C). Relict galena (0.15 - 2 mm) also occurs with massive pyrite (ii) (< 1.7mm) (Fig. 15D) with trace amounts of chalcopyrite (~50 μm) and molybdenite (~40 μm) spatially associated in the siderite matrix. This assemblage was observed in sample WAu-4.

The associated alteration assemblage occurring in the wall-rock clasts is comprised of pervasive fine-grained, brown-stained white clay (< 5μm), determined to be illite with the use of a TerraSpec3® infrared spectrometer, fine-grained brown-stained siderite grains (~15 μm) with Mg-rich core, euhedral to subhedral apatite grains (40 - 175 μm) and occasionally muscovite (430 μm) in K-feldspar and plagioclase crystals (Figs. 15E,F). Carbonate-rutile-apatite-K-spar alteration, which consists subhedral to euhedral rutile (70 - 110 μm), euhedral to subhedral apatite grains (40 - 220 μm), and anhedral white clays may be partially or completely included in siderite crystals (20 - 240 μm) in the margins of quartz (ii) matrix (Figs. 15G-I). This assemblage may also occur in the embayment areas of fine-grained pyrite (ii) masses (Fig. 15H).

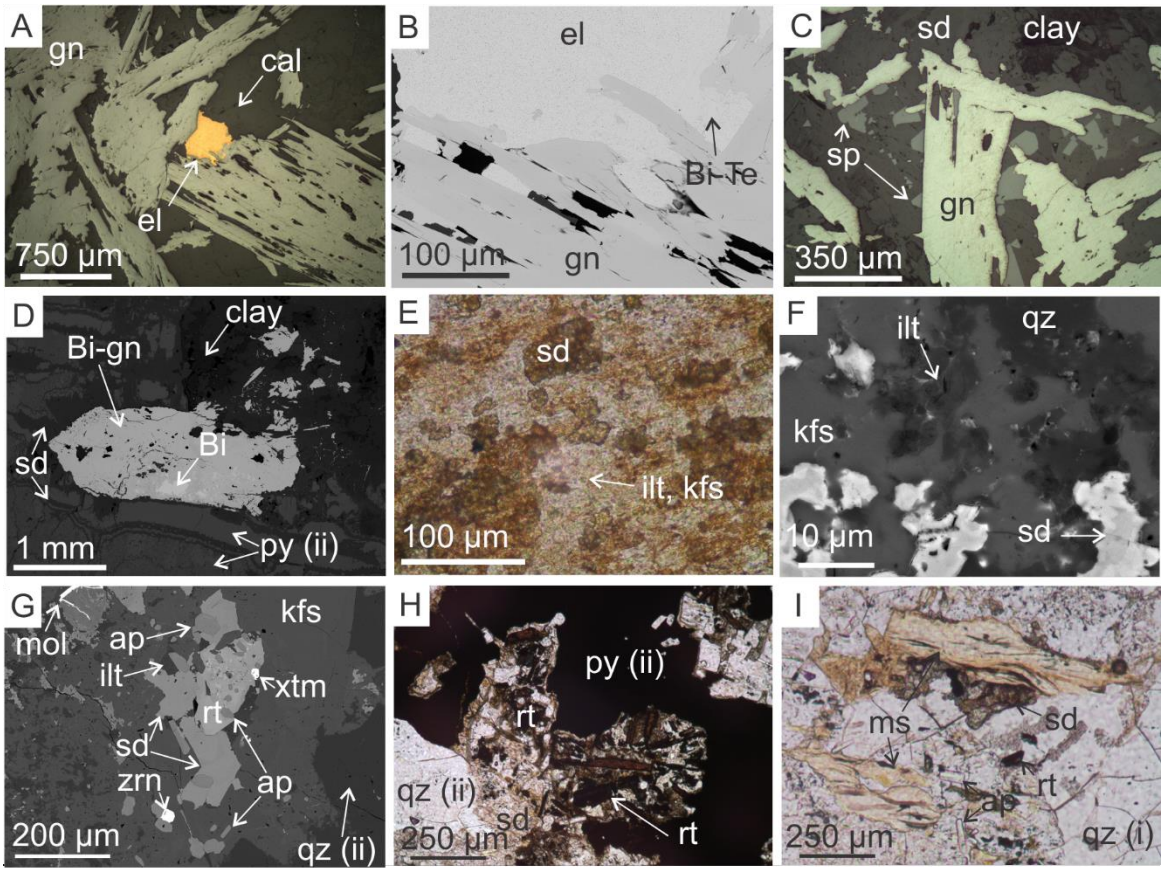

Figure 15. Localized mineral assemblages and associated phyllic to argillic alteration in the WAu breccia style 3 mineralization. A) Bladed galena partially surrounded by late Au and calcite. B) BSE image of electrum from A with areas of Bi-Te enrichment. C) Bladed galena with euhedral sphalerite in a clay-dominated area of the matrix. D) Galena with Bi-enrichments and Bi inclusions surrounded by layered pyrite-siderite. E) Fine-grained clay and anhedral siderite alteration of Revenue granite clasts within the WAu Breccia. F) BSE image of previous region, where quartz, illite, and siderite digest primary K-feldspar crystals. G) BSE image of carbonate-rutile alteration on edges of K-feldspar, where apatite and rutile crystals are inclusions in siderite. H) Rutile crystals form psuedo-radiating texture in pyrite (ii) embayment with clays and siderite interstitial. I) Muscovite occurring with carbonate-rutile alteration.

5.2.6 Style 3 mineralization, Revenue diatreme

The Revenue diatreme hosts mineralization style 3. The diatreme has a fine-grained (< 5 μm) groundmass, predominantly feldspar and quartz with occasional clasts of feldspars (< 1 mm), rounded quartz crystals (< 500 μm), carbonate patches (< 375 μm), and white clays (Fig. 16A). Sulfides of the least-altered representative sample RD-1 are predominantly euhedral pyrite and chalcopyrite with trace amounts of galena and sphalerite. Pyrite (i) cubes (20 - 125 μm) occur disseminated throughout the groundmass and may show local sieve textures and As enrichment, or occur disseminated with chalcopyrite (~175 μm) in dolomite patches (40 – 700 μm) where chalcopyrite may have inclusions (<3 μm) of sphalerite (Fig. 16B). Molybdenite grains (~55 μm) are rare and disseminated within the groundmass (Fig. 16B). Coarse-grained pyrite (1.5 - 3.3 mm) may contain anhedral rutile (70 - 250 μm), chalcopyrite (5 - 100 μm), and pyrrhotite (< 5 - 25 μm) inclusions (Fig. 16C). In rare occurrences, euhedral pyrite may occur with anhedral chalcopyrite with inclusions of galena, surrounded by sphalerite showing chalcopyrite disease(Figs. 16D,E). Alteration minerals associated with sulfides include rutile (~175 μm) which forms in fractures or partially surrounds the pyrite, and may also contain partial inclusions of apatite grains (~30 μm) (see Appendix Section 4E).

In the brecciated sample RD-2 from near the margins of the diatreme, sulfide mineralization predominantly occurs as creeping-net texture chalcopyrite (~500 - 800 μm) with inclusions of sphalerite and galena, surrounding clasts of quartz and feldspar (Fig. 16F). This is mantled by marcasite±pyrite (~25 μm mantle, masses <350 μm; Fig. 16F), where pyrite may be fragmented and altered to marcasite on the edges or completely replaced by marcasite. Large masses of smooth to fractured marcasite (< 1 mm) also occur in the surrounding groundmass (Fig. 16G), spatially associated to anhedral masses of fine-

grained rutile (< 650 µm). Trace arsenopyrite and galena occur disseminated in siderite lining massive chalcopyrite in this assemblage.

The phyllic alteration assemblages associated with mineralization in both areas include previously mentioned clay and carbonate patches (Fig. 16A). Rounded and partially digested apatite grains (< 80 µm) occur in alteration patches and are spatially associated with needle (<5 µm) and zoned, euhedral (<10 µm) rutile, and trace amounts of very fine-grained anhedral pyrite (< 5 µm; Figs. 16H,I).

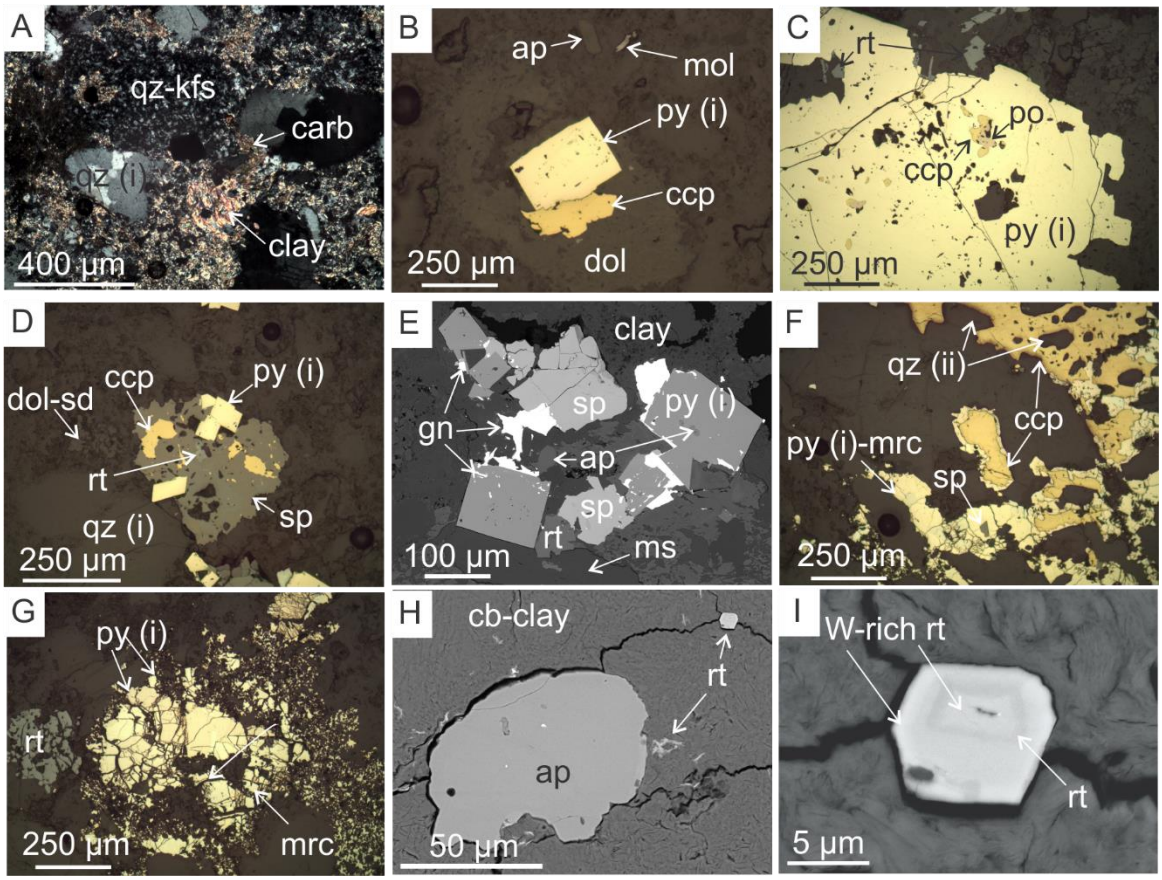

Figure 16. Main mineral assemblages of the Revenue diatreme style 3 mineralization. A) Sample RD-1; representative XPL image of phyllic altered Revenue diatreme groundmass with quartz clasts. B) Sample RD-1; disseminated pyrite cube with later chalcopyrite in dolomite in the least-altered Revenue diatreme. Apatite and trace molybdenite occur disseminated in groundmass. C) Chalcopyrite and pyrrhotite inclusions in coarse-grained pyrite cubes, which may partial include rutile. D) Sample RD-1; rare aggregate of sphalerite containing inclusions of chalcopyrite and cubic pyrite in the least-altered Revenue diatreme. E) Sample RD-1; BSE image of same region in C, showing galena overprinting pyrite and sphalerite. Pyrite contains apatite inclusions. F) Sample RD-2; large, anhedral chalcopyrite and quartz mantled by marcasite-altered pyrite in the phyllic altered area of the Revenue diatreme. Trace sphalerite occurs as inclusions within pyrite. G) Sample RD-2; fragmented pyrite (i) altered to marcasite with fragmented rutile. H) Sample RD-2; BSE image of carbonate (dolomite-siderite) and clay alteration digesting early apatite grain. I) Sample RD-2; BSE image of W-zonation in euhedral rutile.

5.3 Mineral chemistry of sulfides and sulfarsenides

5.3.1 EMPA major and minor elements

EMPA analysis was used to determine major and minor element composition of sulfides including sphalerite and arsenopyrite, and the sulfarsenide glaucodot. Mineral compositions are summarized in Table 2. For full dataset, see Appendix 6.

Analyses of sphalerite were obtained using the EMPA for samples from late BSZ (L-BSZ-1 and L-BSZ-2), WAu breccia (WAu-3), and the Revenue diatreme (RD-1), seen in Table 2. In the late BSZ, the sphalerite composition between the two samples differed in both Fe, Cu, and Zn abundances. Sphalerite from L-BSZ-1 (representing the quartz-vein assemblage; n = 3) contains near stoichiometric S (49.69±0.03 mol%), Zn (37.78±1.03 mol%), Fe (9.88±0.27 mol%), and variable Cu (1.2 – 2.98 mol%). Trace elements for this sphalerite include Co (0.03 mol%), Sn (0.07 - 0.60 mol%), Cd (0.41±0.01 mol%), and In (0.08±0.03 mol%). In comparison, sphalerite from sample L-BSZ-2 (representing the quartz-carbonate vein assemblage; n = 4) contains variable S (33.11 - 49.75 mol%), Zn (40.18 - 56.29 mol%), Fe (5.64±0.23 mol%), and Cu (3.66±0.0.49 mol%). Minor elements for this sphalerite include Co (below detection limit (bdl) - 0.02 mol%), Pb (bdl – 0.02 mol%), Sn (bdl – 0.41 mol%), Cd (0.29-1.09 mol%), and In (0.03 – 0.07 mol%). Sphalerite from sample WAu-3 (n = 11) contains variable S (33.34 - 49.89 mol%) with variable Zn (32.44 – 53.66 mol%), Fe (5.45 – 11.65 mol%), and Cu (0.11 - 5.72 mol%). Minor and trace elements for this sphalerite include Co (0.04±0.02 mol%), Cd (0.22 - 0.71 mol%), and In (0.03 - 0.53 mol%). In one analysis, Sn was detected at 2.35 mol% though all other analysis were below detection limits. Sphalerite from RD-1 (n = 9) contains S (49.98±0.18 mol%) and Zn (42.64±0.41 mol%) with variable Fe (3.73 - 7.00 mol%) and Cu (0.07 - 3.50

mol%). Minor and trace elements from this sphalerite include Cd (0.04 - 0.29 mol%), and In (0.03 mol%).

Table 2. Normalized sphalerite composition in molecular percent (mol%) obtained from samples L-BSZ-1, L-BSZ-2, WAu-3, and RD-1 via EMPA. bdl = below detection limits.

	Element (mol%)									
Sample and point	Fe	Cu	Zn	Co	S	Pb	Sn	Cd	In	total
RD-1-Sp-1	3.73	3.00	43.00	bdl	50.04	bdl	bdl	0.18	0.03	100
RD-1-Sp-2	3.76	2.73	43.25	bdl	50.02	bdl	bdl	0.20	0.03	100
RD-1-Sp-3	3.85	3.12	42.67	bdl	50.12	bdl	bdl	0.19	0.04	100
RD-1-Sp-4	3.84	3.50	42.18	bdl	50.23	bdl	bdl	0.18	0.03	100
RD-1-Sp-5	5.02	2.07	42.93	bdl	49.75	bdl	bdl	0.18	0.03	100
RD-1-Sp-6	6.32	1.26	42.12	bdl	50.00	bdl	bdl	0.26	0.03	100
RD-1-Sp-7	6.83	0.56	42.13	bdl	50.17	bdl	bdl	0.28	0.03	100
RD-1-Sp-8	7.00	0.07	42.77	bdl	49.81	bdl	bdl	0.29	0.03	100
RD-1-Sp-9	4.69	2.74	42.75	bdl	49.73	bdl	bdl	0.04	0.04	100
L-BSZ-1-Sp-1	10.12	1.29	38.17	0.04	49.71	bdl	0.21	0.40	0.05	100
L-BSZ-1-Sp-2	9.60	2.98	36.61	0.03	49.71	bdl	0.59	0.39	0.08	100
L-BSZ-1-Sp-3	9.94	1.22	38.56	0.03	49.66	bdl	0.07	0.41	0.11	100
L-BSZ-2-Sp-1	5.35	3.95	56.29	0.02	33.11	0.02	bdl	1.09	0.07	100
L-BSZ-2-Sp-2	5.59	4.10	40.18	0.01	49.67	bdl	bdl	0.41	0.03	100
L-BSZ-2-Sp-3	5.73	3.65	40.64	bdl	49.57	bdl	0.05	0.29	0.03	100
L-BSZ-2-Sp-4	5.89	2.99	40.39	bdl	49.75	bdl	0.41	0.49	0.03	100
WAu-3-Sp-1	9.59	0.20	40.19	0.04	49.49	bdl	bdl	0.30	0.18	100
WAu-3-Sp-2	9.42	0.21	40.42	0.05	49.39	bdl	bdl	0.33	0.16	100
WAu-3-Sp-3	9.28	0.11	40.26	0.05	49.89	bdl	bdl	0.29	0.11	100
WAu-3-Sp-4	9.91	5.72	32.44	0.05	49.23	bdl	2.35	0.22	0.03	100
WAu-3-Sp-5	9.49	0.11	40.51	0.05	49.43	bdl	bdl	0.32	0.10	100
WAu-3-Sp-6	8.80	0.18	40.66	0.03	49.85	bdl	bdl	0.40	0.05	100
WAu-3-Sp-7	11.65	0.11	38.90	0.05	48.89	bdl	bdl	0.34	0.06	100
WAu-3-Sp-8	9.16	0.49	40.02	0.05	49.73	bdl	bdl	0.33	0.21	100
WAu-3-Sp-9	10.67	0.95	53.66	0.09	33.34	bdl	bdl	0.71	0.53	100
WAu-3-Sp-10	5.81	4.71	39.30	0.02	49.83	bdl	bdl	0.27	0.05	100
WAu-3-Sp-11	5.45	4.06	40.29	0.02	49.84	bdl	bdl	0.28	0.05	100

Measurements of arsenopyrite were obtained for the sample QFP-2 (n=17), seen in Table 3. Typical arsenopyrite (n = 12) has variable S (30.32 – 38.64 mol%), Fe (32.58±0.84 mol%), and As (29.24 – 35.48 mol%). Minor and trace elements include Co (0.06 – 1.47 mol%), with two points reporting Ni (0.15 and 0.84 mol%) one point reporting Cu (0.25 mol%), and points reporting below detection limits for Pb. Co-Ni-rich arsenopyrite (n=5) has variable S (24.54 – 38.59 mol%), As (23.25 – 41.01 mol%), Fe (11.67 – 21.80 mol%), Co (8.33 – 15.81 mol%), and Ni (4.09 – 9.56 mol%). Minor elements include Cu (bdl – 0.88 mol%) and Pb (bdl – 0.11 mol%).

Measurements of glaucodot were obtained for samples from the WAu breccia (WAu-2 and WAu-3), seen in Table 4. Glaucodot (n = 18) has variable Co (37.25 – 45.62 mol%), S (27.12 – 35.91 mol%), As (08.21 – 24.41 mol%), Fe (2.99 – 8.42 mol%), and minor amounts of Ni (bdl – 0.70 mol%).

Table 3. Normalized arsenopyrite composition in molecular percent (mol%) obtained for sample QFP-2 via EMPA, University of Toronto. Green fields indicate values used for thermometry plot. Blue field indicate values of the Co-Ni-rich arsenopyrite grains. D.L = detection limit, bdl = below detection limit.

Point	Fe	Fe(D.L.)	Cu	Cu(D.L.)	As	As(D.L.)	Co	Co(D.L.)	Ni	Ni(D.L.)	S	S(D.L.)	Pb	Pb(D.L.)	Total
Typical arsenopyrite															
QFP-2-A1-apy-1	31.64	0.12	bdl	0.19	29.24	0.08	0.32	0.06	0.15	0.07	38.64	0.07	bdl	0.04	100
QFP-2-A2-apy-1	31.98	0.12	bdl	0.16	32.38	0.08	0.25	0.06	bdl	0.08	35.39	0.07	bdl	0.03	100
QFP-2-A2-apy-2	32.47	0.11	0.25	0.18	32.84	0.08	0.15	0.07	bdl	0.08	34.29	0.08	bdl	0.03	100
QFP-2-A2-apy-3	32.35	0.11	bdl	0.21	31.99	0.08	0.09	0.06	bdl	0.07	35.58	0.07	bdl	0.03	100
QFP-2-A2-apy-4	33.60	0.13	bdl	0.18	31.93	0.08	0.19	0.05	bdl	0.07	34.28	0.07	bdl	0.03	100
QFP-2-A2-apy-5	33.09	0.15	bdl	0.18	30.86	0.08	0.14	0.05	bdl	0.08	35.91	0.07	bdl	0.04	100
QFP-2-A2-apy-7	31.44	0.11	bdl	0.15	29.30	0.08	0.24	0.05	bdl	0.07	39.02	0.07	bdl	0.04	100
QFP-2-A2-apy-8	33.93	0.12	bdl	0.19	32.99	0.08	0.07	0.05	bdl	0.07	33.01	0.07	bdl	0.03	100
QFP-2-A2-apy-10	33.23	0.14	bdl	0.18	30.19	0.08	0.12	0.05	bdl	0.07	36.47	0.07	bdl	0.03	100
QFP-2-A2-apy-12	32.00	0.12	bdl	0.19	32.12	0.08	0.12	0.05	bdl	0.07	35.76	0.07	bdl	0.03	100
QFP-2-A2-apy-13	33.42	0.14	bdl	0.18	31.22	0.08	0.06	0.05	bdl	0.07	35.30	0.07	bdl	0.03	100
QFP-2-A3-apy-1	31.82	0.14	bdl	0.18	35.48	0.08	1.47	0.05	0.84	0.08	30.39	0.07	bdl	0.03	100
Co-Ni-rich arsenopyrite															
QFP-2-A3-apy-Ni-1	20.34	0.13	bdl	0.20	36.26	0.08	8.77	0.07	4.09	0.08	30.49	0.08	0.04	0.03	100
QFP-2-A3-apy-Ni-2	11.67	0.16	bdl	0.21	38.83	0.08	12.46	0.07	9.56	0.08	27.47	0.07	bdl	0.04	100
QFP-2-A3-apy-Ni-3	12.84	0.12	0.33	0.20	23.25	0.07	15.81	0.06	9.07	0.07	38.59	0.07	0.11	0.03	100
QFP-2-A3-apy-Ni-4	17.89	0.15	0.28	0.22	41.01	0.09	8.33	0.07	7.95	0.09	24.54	0.07	bdl	0.04	100
QFP-2-A3-apy-Ni-5	21.80	0.14	0.88	0.21	29.48	0.08	8.69	0.05	5.21	0.08	33.91	0.07	0.03	0.03	100

Table 4. Normalized glaucodot composition in molecular percent (mol%), obtained from samples WAu-2 and WAu-3 via EMPA.

Sample	Fe	S	As	Co	Ni	Total
WAu-2	2.99	29.19	22.31	45.53	bdl	100.00
WAu-2	8.42	35.91	18.21	37.25	0.22	100.00
WAu-2	4.01	27.12	23.12	45.62	0.14	100.00
WAu-2	5.77	28.27	22.93	42.54	0.50	100.00
WAu-3	6.12	28.05	23.94	41.34	0.53	100.00
WAu-3	6.09	28.68	23.70	40.99	0.53	100.00
WAu-3	5.16	28.10	23.24	42.96	0.49	100.00
WAu-3	7.41	28.31	24.63	38.99	0.66	100.00
WAu-3	6.58	28.40	23.43	40.91	0.66	100.00
WAu-3	7.30	28.45	23.83	39.81	0.62	100.00
WAu-3	7.43	28.26	23.87	39.82	0.59	100.00
WAu-3	7.44	27.87	24.71	39.27	0.70	100.00
WAu-3	6.57	27.93	24.07	40.87	0.56	100.00
WAu-3	6.44	28.25	23.71	41.10	0.44	100.00
WAu-3	6.13	28.25	23.68	41.39	0.44	100.00
WAu-3	6.64	27.87	24.01	40.80	0.60	100.00
WAu-3	6.86	27.80	24.54	40.18	0.61	100.00
WAu-3	6.54	27.49	24.29	41.08	0.62	100.00

5.3.2 LA-ICP-MS trace element data of major sulfide minerals

Chalcopyrite, pyrite, and pyrrhotite from the BSZ (samples E-BSZ-2 and L-BSZ-2), the QFP (samples QFP-1 and QFP-2), WAu breccia (sample WAu-3), and Revenue diatreme (samples RD-1 and RD-2) were analyzed via LA-ICP-MS.

5.3.2.1 Chalcopyrite

Early style 1 mineralization (sample E-BSZ-2)

Compared to other samples, chalcopyrite from sample E-BSZ-2 (n = 3) shows appreciable amounts of Zn (379 - 1130 ppm), Ni (5.43±1.07 ppm), moderate Se (25.4 - 30.4 ppm), Ag (48.23±0.45 ppm), Cd (5.3 - 10.9 ppm), In (13.7±2 ppm), and low Pb (0.92 - 2.68 ppm) (Table 5). Chalcopyrite typically contains low (< 2 ppm) Co, Ge, Sn, Sb, Au, and Bi. This chalcopyrite contains concentrations below detection limits for at least half or more analysis of As, Mo, Te, W, Pt, and Hg. In comparison to chalcopyrite from other samples, this chalcopyrite has the highest Co (1.613±0.105 ppm), Ni, and lowest In and Sn (0.165 - 0.49 ppm).

Late style 1 mineralization (sample L-BSZ-2)

Compared to other samples, chalcopyrite from the late BSZ (sample L-BSZ-2; n = 5) has appreciable Zn (433 - 2200 ppm), Ag (350 - 449 ppm), Sn (295 - 352 ppm), Pb (6.25 - 13.6 ppm) and Bi (1.87 - 5.04 ppm), relatively moderate levels of Se (13.6 - 32 ppm), Cd (9.3 - 49 ppm), In (20.64±27.25 ppm) (Table 5). This chalcopyrite typically contains low (< 2 ppm) Co, Ni, Ge, Sb, Te, Pt, and Au. This chalcopyrite contains concentrations below detection limits for at least half or more analysis of Ni, Ge, As, Mo, Te, W, and Hg. Chalcopyrite from the late BSZ has the highest values of Zn, Ag, and Pb, and lowest values of Co (bdl - 0.68 ppm) and Se when compared to chalcopyrite from the other locations.

Least altered QFP (sample QFP-1)

Compared to other samples, chalcopyrite of the least altered QFP (sample QFP-1; n = 4) has relatively appreciable Ag (658 – 727 ppm) and As (bdl – 12.6 ppm), relatively moderate levels of Co (1.46 – 2.94 ppm), Zn (516 – 938 ppm), Se (29.3 – 40.7 ppm), Cd (19.1 – 28.9 ppm), In (37.6 – 42.2 ppm), and Sn (2.48 – 8.2 ppm) (Table 5). This chalcopyrite typically contains low (< 2 ppm) Ge, Sb, Te, Wn, Pb, and Bi. This chalcopyrite contains concentrations below detection limits for at least half or more analysis of Ni, As, Mo, Sb, Te, W, Pt, Au, and Hg. This chalcopyrite also has the highest abundance of Ag in comparison to others.

Phyllic-altered QFP (sample QFP-2)

Compared to other samples, chalcopyrite of the phyllic-altered QFP (sample QFP-2; n = 3) has relatively appreciable Zn (494 – 1990 ppm), Ag (279 – 302.6 ppm), relatively moderate levels of Se (54.9 – 77.4 ppm), Cd (10.6 – 38.5 ppm), In (25.01 – 31.8 ppm), Sn (251.4 – 264 ppm), and Pb (4.15 – 10 ppm) (Table 5). This chalcopyrite typically contains low (< 2 ppm) Co, Ni, Ge, Mo, Sb, Te, Au, and Bi. This chalcopyrite contains concentrations below detection limits for at least half or more analysis of As, Te, W, Pt, Au, and Hg. The chalcopyrite analyzed in from QFP-2 is very similar to that of the late BSZ with the former comprising of higher Se.

Style 2 mineralization (sample WAu-3)

Compared to other samples, chalcopyrite from the WAu breccia (sample WAu-3; n = 6) has relatively appreciable Co (0.036 - 4.79 ppm), Zn (549 - 1060 ppm), Se (18.3 - 40.8 ppm), Cd (13.7 - 29.3 ppm), In (100.3-155 ppm), and Sn (216 - 489 ppm), with relatively moderate levels of Ag (15.5 - 42.4 ppm), Pb (0.62 - 3.38 ppm), and variable Sb (0.11 - 2.17 ppm) and Bi (0.135 - 2.48 ppm) (Table 5). This chalcopyrite typically contains low (< 2

ppm) Ni, Ge, As, Mo, Te, W, Pt, Au, and Hg. This chalcopyrite contains concentrations below detection limits for at least half or more analysis of Ni, Ge, As, Mo, Te, Pt, Au, and Hg. The chalcopyrite from this location has relatively low Co, Se, Cd, In, and Sn when compared to the chalcopyrite from the other locations.

Least-altered Revenue diatreme (sample RD-1)

Compared to other samples, chalcopyrite of the least altered Revenue diatreme (sample RD-1; n = 2) has anomalously high Zn (0.53 - 2.03 wt%), relatively appreciable Cd (960 – 4200 ppm), relatively moderate levels of Ag (15.1 – 33.3 ppm), In (34.9 – 67.3 ppm), Sn (583 – 649 ppm), Sb (12.78 – 19.4 ppm), Hg (2.01 – 7.5 ppm), Pb (12 – 21 ppm), and Bi (6.51 – 14.9 ppm) (Table 5). This typically contains low (< 2 ppm) Co, Ge, and Te. This chalcopyrite contains concentrations below detection limits for at least half or more analysis of Ni, Ge, As, Se, Mo, W, Pt, and Au. The anomalously high levels of Zn, and Cd likely represent sphalerite inclusions.

Style 3 mineralization (sample RD-2)

Compared to other samples, chalcopyrite of the phyllic-altered Revenue diatreme (sample RD-2; n = 5) has relatively appreciable Zn (489 – 1430 ppm and one analysis of 8600 ppm), As (bdl – 168 ppm), Sn (707 – 1404 ppm), Sb (bdl – 22.5 ppm), Pb (2.82 – 57.4 ppm), and Bi (0.93 – 30 ppm), relatively moderate levels of Ge (2.19 – 3.6 ppm), Se (18.5 ppm) Ag (1.36 – 20 ppm), Cd (8 – 20.7 ppm, with one analysis of 149 ppm), and In (15.88 – 25.01 ppm) (Table 5). This chalcopyrite typically contains low (< 2 ppm) Co, Ni, Mo, Te, Au, and Hg. This chalcopyrite contains concentrations below detection limits for at least half or more analysis of Ni, As, Se, Mo, W, Pt, and Hg. Similar to the least altered Revenue diatreme, the correlations of anomalously high Sn and Cd are likely due to

sphalerite inclusions in the chalcopyrite. The chalcopyrite from RD-2 also contains the highest Sn values in comparison to chalcopyrite in other samples.

5.3.2.2 Pyrite

Early style 1 mineralization (sample E-BSZ-2)

Compared to other samples, pyrite from the early BSZ (sample E-BSZ-2, n = 5) has appreciable As (2040 - 4660 ppm), Co (15 - 227 ppm), Se (47.8 - 58.8 ppm), Ni (0.97 - 3.15 ppm), Te (1.29 - 3.10 ppm) (Table 6). Pyrite typically contains low (< 2 ppm) Cu, Ge, Sb, Au, Pb, and Bi. This pyrite contains concentrations below detection limits for at least half or more analysis of Zn, Mo, Pd, Ag, Cd, In, Sn, W, Pt, and Hg. One analysis has relatively high concentrations of some of the lesser elements, including Cu (6.7 ppm), Ag (2.42 ppm), Sb (23.5 ppm), Pb (82 ppm), and Bi (46.2 ppm). In comparison to the pyrite analyses from the other pyrites, this sample has the among the highest As readings.

Late style 1 mineralization (sample L-BSZ-2)

Compared to other samples, pyrite from the late BSZ (sample L-BSZ-2; n = 5) has appreciable amounts of Co (220 - 580 ppm), Ni (200 - 570 ppm), Pb (20.62 - 300 ppm), Ag (7.53 - 19.6 ppm), Se (1.2 - 30.4 ppm), W (4.17 - 6.28 ppm), Cu (0.77 - 4.2 ppm), Sb (0.81 - 2.37 ppm), and Bi (0.68 - 3.7 ppm) (Table 6). This pyrite typically contains low (< 2 ppm) Zn, Ge, As, Cd, In, Sn, Pt, and Au. This pyrite contains concentrations below detection limits for at least half or more analysis of As, Mo, Pd, Te, Pt, Au, and Hg. This pyrite has among the highest levels of Ni, Wn, and Pb in comparison to pyrite from other areas.

Least altered QFP (sample QFP-1)

Compared to other samples, pyrite from the least altered QFP (sample QFP-1, n = 3) has appreciable Cu (1.58 – 1210 ppm), Zn (bdl – 62 ppm), and As (2340 - 3240 ppm),

relatively moderate levels of Co (13.11 – 105 ppm), Ni (1.12 – 19.4 ppm), Se (11.8 – 17.9 ppm), Ag (bdl – 8.4 ppm), Sb (0.94 – 11.7 ppm), Te (1.53 – 2.76 ppm), and variable levels of Sn (bdl – 19.2 ppm), W (bdl – 25 ppm), Pb (9.1 - 97.2 ppm), and Bi (0.96 – 32.1 ppm) (Table 6). This pyrite typically contains low (< 2 ppm) Ge, Mo, Cd, In, Sn, and Au. This pyrite contains concentrations below detection limits for at least half or more analysis of Pt and Hg. This sample has among the highest values of As, and has the highest value of Sn in the analyzed pyrite, though the values were variable and likely due to an inclusion or heterogeneous grain.

Phyllic-altered QFP (sample QFP-2)

Compared to other samples, pyrite from the phyllic-altered QFP (sample QFP-2, n = 3) has relatively moderate levels of Ni (107 – 143 ppm), As (250.3 – 752 ppm), Se (16.5 – 24.9 ppm), and variable levels of Co (6.74 – 472 ppm), Pb (0.235 – 2.7 ppm), and Bi (0.47 – 7.2 ppm) (Table 6). This pyrite typically contains low (< 2 ppm) Cu, Ge, Ag, Sb, Te, Au, and Pb. This pyrite contains concentrations below detection limits for at least half or more analysis of Zn, Mo, Cd, In, Sn, Sb, W, Pt, and Hg.

Style 2 mineralization (sample WAu-3)

Compared to other samples, pyrite from the WAu breccia (sample WAu-3; n = 6) has appreciable Co (675 - 1140 ppm), with relatively moderate Ni (14.6 - 86.4 ppm), Se (21.3 - 46.9 ppm), W (0.72 - 26.2 pm), Ag (0.096 - 2.06 ppm), and Pb (1.06 - 2.81 ppm) (Table 6). This pyrite typically contains low (< 2 ppm) Cu, Ag, Ge, Mo, Cd, In, Sn, Sb, Te, Pt, Au, Hg, and Bi. This pyrite contains concentrations below detection limits for at least half or more analysis of Zn, As, Mo, Pd, Cd, In, Sn, Te, Pt, Au, and Hg. One analysis has relatively high As (41.7 ppm) in comparison with other analysis in this sample. This pyrite was also the only one with relatively appreciable Mo (< 0.144 ppm).

Least altered Revenue diatreme (sample RD-1)

Compared to other samples, pyrite from the least altered Revenue diatreme (sample RD-1, n = 7) has appreciable Co (4.93 – 3030 ppm), Ni (117 – 525 ppm), As (177 – 2970 ppm), with relatively moderate levels of Cu (0.72 – 162 ppm), Se (bdl – 11.8 ppm), and variable Zn (bdl – 101.2 ppm), Ag (bdl – 5.27 ppm), Sb (bdl – 43.4 ppm), Te (0.25 -20.5 ppm), Pb (0.09 – 113.8 ppm), and Bi (0.342 – 38.9 ppm) (Table 6). This pyrite typically contains low (< 2 ppm) Ge, Mo, Cd, In, W, Pt, and Au. This pyrite contains concentrations below detection limits for at least half or more analysis of Zn, Mo, In, Sb, W, Pt, and Hg. The pyrite of sample RD-1have the highest and generally consistent values of Co and Ni, as well as As, Pb, and Bi. Some analyses also report the highest values of Sb, and Te, though they are variable.

Style 3 mineralization (sample RD-2)

Compared to other samples, pyrite from the phyllic-altered Revenue diatreme (sample RD-2, n = 4) has appreciable Cu (165 – 546 ppm), Zn (10.14 – 19.6 ppm), Ag (31.3 – 52 ppm), Au (2.306 – 4.46 ppm), and Pb (126-532 ppm), with relatively moderate levels of Co (2.3 – 11.92 ppm), Ni (1.94 – 64.7 ppm), Ge (2.88 – 3.82 ppm), and variable As (bdl – 37.5 ppm), Sb (0.5 – 5.06 ppm), and Bi (0.216 – 37.7 ppm) (Table 6). This pyrite typically contains low (< 2 ppm) Se, Mo, Cd, In, Sn, Te, W, and Hg. This pyrite contains concentrations below detection limits for at least half or more analysis of Cd and Pt. The Cu, Zn Ag, Au, and Pb values of this pyrite were the highest in comparison to others and generally consistent between analyses.

5.3.2.3 Pyrrhotite

Early style 1 mineralization (sample E-BSZ-2)

Compared to other samples, pyrrhotite from the early BSZ (Sample E-BSZ-2; n = 5) has appreciable Co (338.4±10.64 ppm) and Ni (435 - 517 ppm), relatively moderate Se (27.2 - 32.8 ppm) and Pb (2.43 - 5.91 ppm), variable Cu (0.88 - 2.6 ppm), and Bi (0.7 - 2.12 ppm) (Table 7). This pyrrhotite typically contains low (< 2 ppm) Ge, Mo, Ag, In, Sb, and W. This pyrrhotite contains concentrations below detection limits for at least half or more analysis of Zn, As, Mo, Pd, Cd, In, Sn, Te, W, Pt, Au, and Hg. In comparison to pyrrhotite in other samples,

Late style 1 mineralization (sample L-BSZ-2)

Compared to other samples, pyrrhotite from the late BSZ (sample L-BSZ-2; n = 3) has appreciable amounts of Mn (0.8 - 14.9 ppm), Ni (216 - 1540ppm), and variable Pb (2.5 - 4700ppm), Co (0.066 - 127.5 ppm), Cu (4.5 - 260 ppm), Ag (1.33 - 48 ppm), Bi (0.3148 - 86 ppm), Ge (1.38 - 2.31 ppm), and relatively low Cu (4.65±0.21 ppm), Ag (1.33 - 7.4 ppm), Se (6.7 - 10.6 ppm), and Pb (2.5 - 5.2 ppm) (Table 7). This pyrrhotite typically contains low (< 2 ppm) in Zn, Ge, As, Mo, Pd, Cd, In, Sn, Sb, Te, W, Pt, Au, and Hg. This pyrrhotite contains concentrations below detection limits for at least half or more analysis of Zn, As, Pd, Cd, In, Sn, Sb, W, Pt, and Hg. Additionally, this pyrrhotite has the highest concentration of Ni, Cu, and Ag, and the lowest abundances of Co, and Se in comparison to the pyrrhotite from other areas. One of the analysis, L-BSZ-2, is likely an inclusion due to the large Pb, Bi, and Ag values (Table 6).

Least altered QFP (sample QFP-1)

Compared to other samples, pyrrhotite from the least altered QFP (sample QFP-1; n = 4) has appreciable Co (712 - 762 ppm), Pb (2.07 – 85 ppm), and Bi (bdl – 13.56 ppm), with moderate levels of Ni (142.4 – 159.7 ppm), Cu (bdl – 6.3 ppm), Se (27.4 – 39 ppm), and Ag (0.247 – 5.56 ppm) (Table 7). This pyrite typically contains low (< 2 ppm) Ge, Sb,

Te, and Au. This pyrrhotite contains concentrations below detection limits for at least half or more analysis of Zn, As, Cd, In, Sn, Sb, W, Pt, Au, and Hg. One analysis (QFP-1 – Po – 1) has relatively high Ag, Pb, and Bi (Table 7), which is likely due to an inclusion.

Style 2 mineralization (WAu-3)

Compared to other samples, pyrrhotite from the WAu breccia (sample WAu-3; n = 5) has the highest value of Co (4.72 - 602 ppm) and Se (28.4 - 48.4 ppm), relatively moderate Cu (2.5 - 15 ppm), Ag (0.43 - 5.56 ppm) and Pb (0.38 - 5.85ppm), and relatively low Ni (33.9 - 45.6 ppm) (Table 7). This pyrrhotite typically contains low (< 2 ppm) Zn, Ge, As, Mo, Ag, Sb, Te, Au, and Bi. This pyrrhotite contains concentrations below detection limits for at least half or more analysis of Zn, As, Pd, Cd, In, Sn, Sb, W, Pt, Au, and Hg. This sample had the highest values for Co and Se, and lowest values for Ni in comparison to the pyrrhotite from other locations.

In all cases, there is a strong relation between Ag, Pb, Bi, and Sb enrichments occurring together. These may be the result of inclusions, as they do not always occur together in the same sample analyses, though the regular pattern occurs in all three minerals.

Table 5. Trace element composition of chalcopyrite for samples E-BSZ-2, L-BSZ-2, QFP-1, QFP-2, WAu-3, RD-1 and RD-2 obtained from LA-ICP-MS. Values reported are elemental ppm. bdl = below detection limits.

	Element and Isotope (ppm)																							
Sample / Analysis	Mg24	Al27	Ti47	Mn55	Co59	Ni60	Zn66	Ge72	As75	Se82	Mo95	Pd105	Ag107	Pd108	Cd111	In115	Sn118	Sb121	Te125	W182	Pt195	Au197	Hg202	Pb208	Bi209
E-BSZ-2-Ccp - 1	36	120	bdl	bdl	1.61	4.2	379	1.01	bdl	25.4	0	1610	48.2	19.8	5.3	11.4	0.165	0.66	bdl	bdl	bdl	0.041	bdl	0.92	0.89
E-BSZ-2-Ccp - 2	56	100	15	bdl	1.72	6	709	0.87	bdl	28.4	bdl	1530	47.8	35	7.3	15	0.34	0.33	bdl	bdl	bdl	0.041	bdl	2.68	0.8
E-BSZ-2-Ccp - 3	1710	2070	21	bdl	1.51	6.1	1130	bdl	bdl	30.4	bdl	1340	48.7	59	10.9	14.7	0.49	0.49	0.78	bdl	bdl	0.027	bdl	1.73	0.8
L-BSZ-2-Ccp - 1	1410	2000	11	bdl	0.142	bdl	563	bdl	bdl	13.6	0	1100	423	32	9.3	20.4	349	1.43	2.1	bdl	bdl	0.27	2	6.25	3.24
L-BSZ-2-Ccp - 2	1250	1300	20	bdl	0.11	bdl	433	bdl	bdl	26	0	1090	350	25	11.3	20.1	331	0.95	bdl	bdl	bdl	0.21	bdl	9.5	1.87
L-BSZ-2-Ccp - 3	880	940	bdl	bdl	bdl	bdl	850	bdl	bdl	32	0	1130	404	62	17.3	19.1	295	1.72	bdl	bdl	bdl	0.179	bdl	9.9	2.19
L-BSZ-2-Ccp - 4	360	1300	25	bdl	bdl	0.99	930	bdl	bdl	26	bdl	1250	384	72	17.2	21.9	352	1.17	bdl	bdl	bdl	0.073	bdl	7.2	1.99
L-BSZ-2-Ccp - 5	1700	2000	14	bdl	0.68	bdl	2200	bdl	bdl	16	0	830	449	150	49	21.7	298	0.7	bdl	bdl	bdl	0.146	bdl	13.6	5.04
QFP-1 - Ccp - 1	219	580	31	bdl	1.46	bdl	560	1.76	11.5	29.3	bdl	9.7	658	0.46	19.1	37.6	3.89	bdl	0.45	0.077	bdl	bdl	bdl	1.36	0.87
QFP-1 - Ccp - 2	180	280	34	bdl	2.71	bdl	938	1.5	bdl	40.7	0	11.43	703	0.7	28.9	41.27	3.43	0.58	0.6	bdl	bdl	bdl	bdl	1.46	1.19
QFP-1 - Ccp - 3	297	310	59	bdl	2.94	bdl	516	2	12.6	35.6	bdl	10.3	727	0.68	24.5	41.5	8.2	bdl	bdl	0.29	bdl	bdl	bdl	1.59	1.16
QFP-1 - Ccp - 4	1830	2230	52	bdl	2.73	bdl	671	1.77	bdl	38	0	10.4	680	0.38	25.3	42.2	2.48	0.52	bdl	bdl	bdl	bdl	bdl	2.19	2.1
QFP-2 - Ccp - 1	390	680	31	bdl	0.7	0.73	816	1.38	bdl	65	0.079	11.17	279	0.4	16.9	28.93	264	0.77	0.99	bdl	bdl	bdl	bdl	4.15	1.61
QFP-2 - Ccp - 2	570	330	45	bdl	1.2	0.82	1990	2.45	bdl	77.4	0	11.5	302.6	1.29	38.5	31.8	251.4	0.47	bdl	bdl	bdl	bdl	bdl	10	1.89
QFP-2 - Ccp - 3	38	300	66	bdl	0.335	0.54	494	1.39	bdl	54.9	bdl	10.17	279.6	0.26	10.6	25.01	258.1	0.48	bdl	bdl	bdl	0.0043	bdl	5.81	1.79
WAu-3-Ccp - 1	bdl	bdl	2.8	bdl	3.9	bdl	900	bdl	bdl	35.4	0	1390	16.8	95	24.4	152	385	0.168	0.78	bdl	bdl	0.023	bdl	1.68	0.17
WAu-3-Ccp - 2	bdl	13	2.6	bdl	3.7	bdl	782	bdl	bdl	33.8	bdl	1738	15.5	126	19.5	135	242	0.202	bdl	bdl	bdl	0.021	0.36	1.31	0.135
WAu-3-Ccp - 3	32	bdl	12	bdl	4.79	bdl	783	0.67	bdl	40.8	0	1630	16.7	84	19	155	448	bdl	bdl	bdl	bdl	0.022	0.49	2.6	0.222
WAu-3-Ccp - 4	44	200	12	bdl	0.036	bdl	840	0.82	bdl	38.9	0	1520	17.8	101	17.8	104	251	0.11	1.03	bdl	bdl	bdl	bdl	0.62	0.5
WAu-3-Ccp - 5	2110	58	bdl	bdl	0.109	bdl	549	bdl	bdl	18.3	0	1223	42.4	66	13.7	113.3	489	2.17	bdl	bdl	bdl	bdl	bdl	3.38	2.48
WAu-3-Ccp - 6	38	156	16	bdl	0.276	bdl	1060	0.81	1.46	34.3	0	1550	27.1	173	29.3	100.3	216	0.263	0.68	bdl	bdl	bdl	0.67	1.04	0.63
RD-1 - Ccp - 1	6900	10100	80	72	2.75	bdl	203000	1.57	bdl	bdl	bdl	12.1	33.3	119	4000	67.3	649	19.4	1.6	bdl	bdl	bdl	7.5	21	14.9
RD-1 - Ccp - 2	112	140	27	15.8	0.76	bdl	52000	bdl	bdl	bdl	bdl	11.62	15.1	29	960	34.9	583	12.78	1.57	bdl	bdl	bdl	2.07	12	6.51
RD-2 - Ccp - 1	330	1180	710	bdl	0.038	bdl	1430	3.6	bdl	18.5	bdl	12.23	5.14	1.06	20.7	19.69	1366	2.14	0.48	bdl	bdl	0.063	bdl	6.91	4.08
RD-2 - Ccp - 2	299	190	38	bdl	bdl	bdl	639	bdl	bdl	bdl	bdl	11.31	1.36	0.18	8	15.88	707	bdl	bdl	bdl	bdl	0.0042	bdl	2.82	2.49
RD-2 - Ccp - 3	520	1700	42	bdl	0.035	0.63	489	2.19	144	bdl	bdl	11.9	20	0.24	12	20.93	945	22.5	0.41	bdl	bdl	0.202	bdl	50.3	30
RD-2 - Ccp - 4	141	180	29	bdl	bdl	bdl	1043	3.4	14.5	bdl	bdl	11.58	7.31	0.48	14.3	23	1404	6.05	1.01	bdl	bdl	0.191	1.03	8.88	0.93
RD-2 - Ccp - 5	174	460	37	bdl	0.2	bdl	8600	2.6	168	bdl	0.062	11.8	17	4.8	149	25.01	1388	14.4	bdl	bdl	bdl	0.237	1.68	57.4	14.44

Table 6. Trace element composition of pyrite from samples E-BSZ-2, L-BSZ-2, QFP-1, QFP-2, WAu-3, RD-1 and RD-2 obtained from LA-ICP-MS. Values reported are elemental ppm. bdl = below detection limits.

	Element and Isotope (ppm)																								
Sample/Analysis	Mg24	Al27	Ti47	Mn55	Co59	Ni60	Cu65	Zn66	Ge72	As75	Se82	Mo95	Pd105	Ag107	Pd108	Cd111	In115	Sn118	Sb121	Te125	W182	Pt195	Au197	Hg202	Pb208	Bi209
E-BSZ-2-Py - 1	4300	99000	12	bdl	37.9	12.2	6.7	bdl	1	2040	47.8	bdl	bdl	2.42	0	bdl	0.0081	0.73	23.5	3.1	bdl	bdl	0.53	bdl	82	46.2
E-BSZ-2-Py - 2	54	340	9.7	bdl	15	0.97	0.55	bdl	bdl	2750	58.8	0	bdl	bdl	0	bdl	bdl	bdl	bdl	2.13	bdl	bdl	0.031	bdl	0.168	0.144
E-BSZ-2-Py - 3	130	45	260	bdl	158	4.92	0.61	bdl	1	2680	49.8	0	bdl	0.041	0	bdl	bdl	bdl	0.132	1.29	bdl	bdl	0.224	bdl	0.98	1.63
E-BSZ-2-Py - 4	95	1000	10.2	bdl	227	3.15	0.82	bdl	1.5	4660	63	0	bdl	bdl	0	bdl	bdl	bdl	bdl	2.3	bdl	bdl	0.33	bdl	0.154	0.168
E-BSZ-2-Py - 5	90	99000	6.6	bdl	71	1.09	1.04	bdl	0.87	3850	57.7	0	bdl	bdl	0	bdl	0.0024	bdl	0.22	1.62	bdl	bdl	0.253	bdl	0.85	1.3
L-BSZ-2 -Py - 1	30000	300	14	6.7	481	448	3.9	1.37	1.52	1.7	20.2	0	bdl	19.6	1.9	0.49	0.031	1.29	2.37	bdl	6.28	bdl	bdl	bdl	300	3.7
L-BSZ-2 -Py - 2	160	310	7.1	bdl	580	570	3.28	1.14	1.76	bdl	30.4	0	bdl	11	2.5	0.6	0.035	1.41	1.63	bdl	4.5	bdl	bdl	bdl	215	0.95
L-BSZ-2 -Py - 3	61	280	8	bdl	220	200	0.77	0.83	1.7	bdl	bdl	0	bdl	7.53	0	0.91	0.043	1.15	1.1	bdl	4.17	bdl	bdl	bdl	218.8	0.068
L-BSZ-2 -Py - 4	113	104	7	bdl	335	336	1.55	0.72	1.56	bdl	7.8	0	bdl	3.05	0	bdl	0.01	0.337	0.64	bdl	6.26	bdl	bdl	bdl	20.62	0.09
L-BSZ-2 -Py - 5	67	bdl	21	bdl	430	332	4.2	0.59	1.84	bdl	23.9	0	bdl	13.8	0	bdl	0.0076	bdl	0.81	bdl	5.94	bdl	bdl	bdl	148	1.01
QFP-1 - Py - 1	134000	608000	231000	3.8	74	14.7	730	35.2	1.9	2340	11.8	0.204	0.034	8.4	0.016	0.73	0.088	19.2	11.7	2.76	25	bdl	0.675	bdl	58.8	32.1
QFP-1 - Py - 2	450	690	77	bdl	13.11	1.12	1.58	bdl	1.88	3240	18.4	bdl	bdl	0.04	bdl	bdl	bdl	bdl	0.94	1.53	bdl	bdl	0.315	bdl	9.1	0.96
QFP-1 - Py - 3	155	5200	4900	bdl	105	19.4	1210	62	1.67	2430	17.9	1.16	0.027	1.48	bdl	1.09	0.045	0.73	10.21	2.64	0.141	bdl	0.559	bdl	97.2	12.44
QFP-2 - Py - 1	4700	101000	78	bdl	46.5	143	1.03	bdl	1.67	497	16.5	bdl	bdl	0.49	bdl	bdl	bdl	bdl	0.7	1.38	bdl	bdl	0.051	bdl	2.7	7.2
QFP-2 - Py - 2	1220	7600	75	bdl	472	119	0.89	bdl	1.92	752	24.9	bdl	0.0102	0.101	0.078	bdl	bdl	bdl	bdl	0.67	bdl	bdl	0.0083	bdl	1.11	3.87
QFP-2 - Py - 3	270	550	109	bdl	6.74	107	0.45	bdl	1.73	250.3	24.5	bdl	bdl	0.014	bdl	bdl	bdl	bdl	bdl	bdl	bdl	bdl	bdl	bdl	0.235	0.47
WAu-3-Py - 1	141	19	9.1	0.53	794	60.3	1.26	bdl	1.46	bdl	21.3	0	bdl	1.36	0	bdl	bdl	bdl	0.262	bdl	2.73	bdl	bdl	bdl	1.06	0.69
WAu-3-Py - 2	29	114	28	bdl	675	50.7	2.3	bdl	1.42	bdl	30.3	bdl	bdl	1.03	0	bdl	bdl	bdl	0.289	bdl	3.16	bdl	bdl	bdl	1.28	0.781
WAu-3-Py - 3	87	97	bdl	bdl	1079	86.4	1.3	bdl	1.14	41.7	46.9	0	bdl	2.06	0	bdl	0.0023	bdl	0.89	bdl	26.2	bdl	bdl	bdl	1.92	0.62
WAu-3-Py - 4	7100	bdl	bdl	3.1	877	67.8	0.57	bdl	1.24	bdl	41.3	0.076	bdl	0.233	0	bdl	bdl	bdl	0.189	0.54	1.74	bdl	bdl	0.47	2.04	1.45
WAu-3-Py - 5	46	24	16	bdl	275	14.6	0.55	bdl	1.01	6	31.8	0.086	bdl	0.145	0	bdl	bdl	bdl	0.212	bdl	0.72	bdl	bdl	bdl	2.16	0.4
WAu-3-Py - 6	49	41	9.2	bdl	1140	84.8	0.41	bdl	1.13	bdl	44.5	0.144	bdl	0.096	0	bdl	0.0027	bdl	0.424	bdl	5.29	bdl	bdl	bdl	2.81	0.623
RD-1 - Py - 1	5300	7200	380	bdl	3030	525	39.8	23.9	2.02	2970	3.3	bdl	bdl	1.82	bdl	0.076	bdl	0.36	17.4	1.32	0.017	0.0082	1.3	bdl	111	14.5
RD-1 - Py - 2	2770	43200	301	0.94	50.6	219	93.3	bdl	2.22	1575	11.8	1.03	bdl	5.27	bdl	0.085	0.0145	1.15	0.45	20.5	1.06	bdl	0.109	bdl	113.8	66
RD-1 - Py - 3	28	450	59	bdl	2880	117	1.9	4.2	1.86	1245	bdl	bdl	bdl	0.111	bdl	0.109	0.0048	bdl	bdl	13.3	bdl	bdl	0.168	bdl	8.1	2.17
RD-1 - Py - 4	75	111	72	bdl	4.93	253	7.1	0.29	1.88	177	4	bdl	bdl	0.125	bdl	bdl	bdl	bdl	bdl	8.2	bdl	bdl	0.0105	bdl	2.33	10.9
RD-1 - Py - 5	2820	5500	1260	bdl	2250	390	162	101.2	1.96	2580	6.3	0.6	bdl	5.58	bdl	0.59	bdl	4.88	43.4	0.82	1.75	bdl	0.79	bdl	273	38.9
RD-1 - Py - 6	137	149	51	bdl	1850	246	0.72	bdl	1.9	2369	3	bdl	bdl	bdl	bdl	bdl	bdl	bdl	bdl	0.25	bdl	bdl	0.067	bdl	0.086	0.342
RD-1 - Py - 7	102	1340	166	bdl	2710	425	0.37	bdl	1.72	1830	bdl	bdl	bdl	0.041	bdl	bdl	bdl	bdl	bdl	1.67	bdl	bdl	0.067	bdl	0.237	1.08
RD-2 - Py - 1	10000	17900	107	10.41	2.3	64.7	544	19.6	3.63	37.9	0.5	0.019	0.0112	51.4	bdl	0.254	0.255	0.365	5.06	0.34	0.88	bdl	2.68	0.86	126	37.7
RD-2 - Py - 2	148	99	109	6.62	8.11	22	546	11.97	3.51	bdl	bdl	0.0046	0.0114	52	bdl	0.117	0.511	1.53	0.79	0.28	0.451	bdl	2.679	0.52	403	9.4
RD-2 - Py - 3	375	207	87	11.63	6.26	1.94	165	17.19	3.82	6.5	2.1	0.042	bdl	31.3	bdl	bdl	0.4	1.42	0.5	0.28	0.826	bdl	2.306	bdl	532	0.216
RD-2 - Py - 4	190	1460	159	6.24	11.92	15.2	368	10.14	2.88	bdl	1.8	bdl	0.017	50.2	bdl	bdl	0.656	0.36	4.01	0.19	0.66	bdl	4.46	0.46	406.3	6.6

Table 7. Trace element composition (in ppm) of pyrrhotite from samples E-BSZ-2, L-BSZ-2, QFP-1 and WAu-3, obtained from LA-ICP-MS. Values reported are elemental ppm. bdl = below detection limits.

	Element and Isotope (ppm)																							
Sample/Analysis	Mg24	Al27	Ti47	Mn55	Co59	Ni60	Cu65	Zn66	Ge72	As75	Se82	Mo95	Pd105	Ag107	Pd108	Cd111	In115	Sn118	Sb121	Te125	W182	Pt195	Au197	Hg202	Pb208	Bi209
E-BSZ-2-Po - 1	120	460	11.1	bdl	349	461	2.6	bdl	1.25	bdl	28.7	0.012	bdl	0.96	0	bdl	0.0015	bdl	0.26	bdl	bdl	bdl	bdl	bdl	3.32	1.22
E-BSZ-2-Po - 2	13	68	20	bdl	350	436	0.88	bdl	1.68	bdl	32.8	0	bdl	0.37	0	bdl	bdl	bdl	0.41	bdl	bdl	bdl	bdl	bdl	3.85	1.53
E-BSZ-2-Po - 3	60000	80000	1310	3.1	330	435	1.28	bdl	1.8	bdl	27.2	0	bdl	0.73	0	bdl	bdl	bdl	0.25	bdl	0.011	bdl	bdl	bdl	2.43	0.7
E-BSZ-2-Po - 4	bdl	24	15	bdl	336	495	0.86	bdl	1.48	bdl	31.4	0	bdl	0.35	0	bdl	bdl	bdl	bdl	bdl	bdl	bdl	bdl	bdl	3.09	1.36
E-BSZ-2-Po - 5	160	570	18	3.5	327	517	2.6	bdl	1.55	bdl	29.5	0	bdl	0.41	0	bdl	bdl	0.113	0.46	bdl	0.021	bdl	bdl	bdl	5.91	2.12
L-BSZ-2-Po - 1	44000	6800	bdl	14.9	bdl	806	4.8	bdl	1.38	bdl	10.6	0.044	bdl	1.33	0	bdl	bdl	bdl	bdl	bdl	bdl	bdl	bdl	bdl	5.2	0.318
L-BSZ-2-Po - 2	3370	2500	16	3.5	1.5	1540	4.5	bdl	1.43	bdl	6.7	0.07	bdl	7.4	0	bdl	bdl	bdl	bdl	0.15	bdl	bdl	bdl	bdl	2.5	0.413
L-BSZ-2-Po - 3	370	110	bdl	bdl	127.5	216	260	bdl	2.31	bdl	8.6	0	2.9	48	0	bdl	bdl	bdl	bdl	0.17	bdl	bdl	0.191	bdl	4700	86
QFP-1 - Po - 1	990	5800	43	bdl	712	142.4	1.6	bdl	2.71	bdl	31.6	0.094	bdl	5.56	bdl	bdl	bdl	bdl	bdl	0.22	bdl	bdl	bdl	bdl	85	13.56
QFP-1 - Po - 2	29	41	33	bdl	729	149.5	6.3	bdl	1.93	bdl	27.4	0	0.021	0.43	bdl	bdl	bdl	bdl	bdl	0.87	bdl	bdl	0.0027	bdl	3.92	1.26
QFP-1 - Po - 3	38	73	44	bdl	728	154.6	1.5	bdl	1.67	bdl	28.9	0	bdl	0.247	bdl	bdl	bdl	bdl	bdl	0.17	bdl	bdl	bdl	bdl	2.07	bdl
QFP-1 - Po - 4	960	600	24	bdl	762	159.7	bdl	2.66	3.5	bdl	39	0	bdl	1.09	bdl	bdl	bdl	bdl	2.22	0.43	bdl	bdl	bdl	bdl	23.8	5.79
WAu-3-Po - 1	36	bdl	11.1	bdl	567	39.6	1.75	bdl	2	bdl	40.1	bdl	bdl	0.241	0	bdl	bdl	bdl	0.53	bdl	bdl	bdl	bdl	bdl	2.75	0.86
WAu-3-Po - 2	12	76	5.6	bdl	602	38.8	2.5	bdl	1.51	bdl	48.4	0.021	bdl	0.225	0	bdl	bdl	bdl	0.8	bdl	bdl	bdl	bdl	bdl	5.85	1.93
WAu-3-Po - 3	27	86	8.3	bdl	559	34.7	1.67	bdl	0.98	bdl	46.5	0	bdl	0.234	0	bdl	bdl	bdl	bdl	bdl	bdl	bdl	bdl	bdl	bdl	0.255
WAu-3-Po - 4	0	bdl	11.5	bdl	504	33.9	3.3	bdl	1.49	bdl	28.4	0	bdl	0.71	0	bdl	bdl	bdl	bdl	bdl	bdl	bdl	bdl	bdl	0.79	0.104
WAu-3-Po - 5	114	86	8	bdl	472	45.6	15	1.07	bdl	bdl	41.9	0	bdl	1.83	0	bdl	0.037	bdl	bdl	bdl	bdl	bdl	bdl	bdl	bdl	0.086

6.0 Discussion

Preliminary models for the Revenue mineralized systems following the hypothesis that of the early style 1 mineralization was over- printed by the late style 1 mineralization, then intruded by a breccia containing style 2 mineralization, and further crosscut by a diatreme that may have remobilized elements or may have developed its own mineralization. Consequently, following this evolution of mineralized systems, it is expected that distinct differences in the trace element chemistry and thermometry of mineral assemblages would be recognized, and/or that mineral chemistry of earlier events may be inherited or preserved in later generations of mineralization impacted by remobilization, reheating, or overprinting., possible trends in compositions or distinct groupings were expected. The involvement of QFP dykes in the development of mineralization styles were also questioned, as sources studies in the Dawson Range have spatially associated the mineralization with porphyritic dyke emplacement (Bineli-Betsi and Lentz, 2011; AMC 2018). Samples for both least altered and phyllic altered in the QFP and Revenue diatreme were used to determine the significance of phyllic-altered areas compared to relatively unaltered states and possible relations to other mineralization styles. Elemental groups (Co-Ni, Ag-Au-Te, and W-Sn) for minerals determined similar relations between one or two zones and distinct mineralization events with no or little clear correlation from one phase to the other. The following discussion tests these ideas by evaluating data types gathered in this study, reconciled with preliminary models for deposit development and magmatic-hydrothermal evolution.

6.1 Trace element data for main sulfide minerals

Trace elements in chalcopyrite, pyrite, and pyrrhotite (present in all styles of mineralization) provide a means to differentiate mineralization styles or mineralizing events that may be otherwise ambiguously related to one another. LA-ICP-MS data (Tables 5, 6 and 7) are summarized on ternary diagrams with the apices Co-Ni (mafic affinity), Ag-Au-Te (epithermal-porphyry affinity), and W-Sn (porphyry-skarn affinity).

Chalcopyrite demonstrated the most diverse and distinct compositional groupings between areas (Fig. 17). Early style 1 mineralization in the BSZ (sample E-BSZ-2) shows a enrichment in Co-Ni relative to W-Sn, hinting at a mafic magmatic influence on the fluid chemistry. In contrast, late style 1 mineralization in the BSZ (sample L-BSZ-2) shows a strong Au-Ag-Te affinity with some influence of W+Sn. Chalcopyrite from the QFP-1 sample shows enrichment in Ag-Au-Te relative to W+Sn, whereas chalcopyrite from sample QFP-2 shows very similar to, and nearly overlapping chemical composition with, late style 1 mineralization. This is in agreement with petrographic work showing that the vein crosscutting the QFP sample shared textural characteristics with the quartz-dolomite veins of late style 1 mineralization. Chalcopyrite from style 2 mineralization of the WAu breccia at locality of sample WAu-3 shows two separate compositional fields, both generally enriched in W+Sn, but with one field favouring the Co-Ni enrichment and the other favouring the Ag-Au-Te enrichment. This suggests two phases of chalcopyrite mineralization. The style 3 mineralization in the Revenue diatreme also show a W-Sn affinity, with the least altered samples occurring in a field between the two style 2 mineralization fields, and the style 3 mineralization occurring the furthest in the W+Sn section.

The genetic relations between styles of mineralization and the separate influence of QFP emplacement show that the early and late style 1 mineralization were derived from different fluids, with the former being more mafic magmatic in affinity and the latter being more similar to epithermal-porphyry precious metal systems. Additionally, the QFP dykes have similar compositions to the late style 1 mineralization, supporting the preliminary hypothesis that QFP dyke emplacement was genetically associated with Au mineralization. Differences between the two may be due to different scales or mechanisms of rock-water interaction affecting the mineral's chemical composition throughout crystallization. The increase in W-Sn abundance from style 2 to style 3 suggests a similar fluid source that was enriched, or became enriched, in these elements over time. Other noted features with respect to trace element composition include a general increase in Zn, Cd, and In abundance in chalcopyrite from the WAu breccia and Revenue diatreme, in comparison to the other locations which may be attributed to the sphalerite inclusions within chalcopyrite. The elements Pb and Ag are highest in chalcopyrite from the late BSZ location, supported by the occurrence of Ag-associate galena infilling fractures in the area (see Appendix 4B).

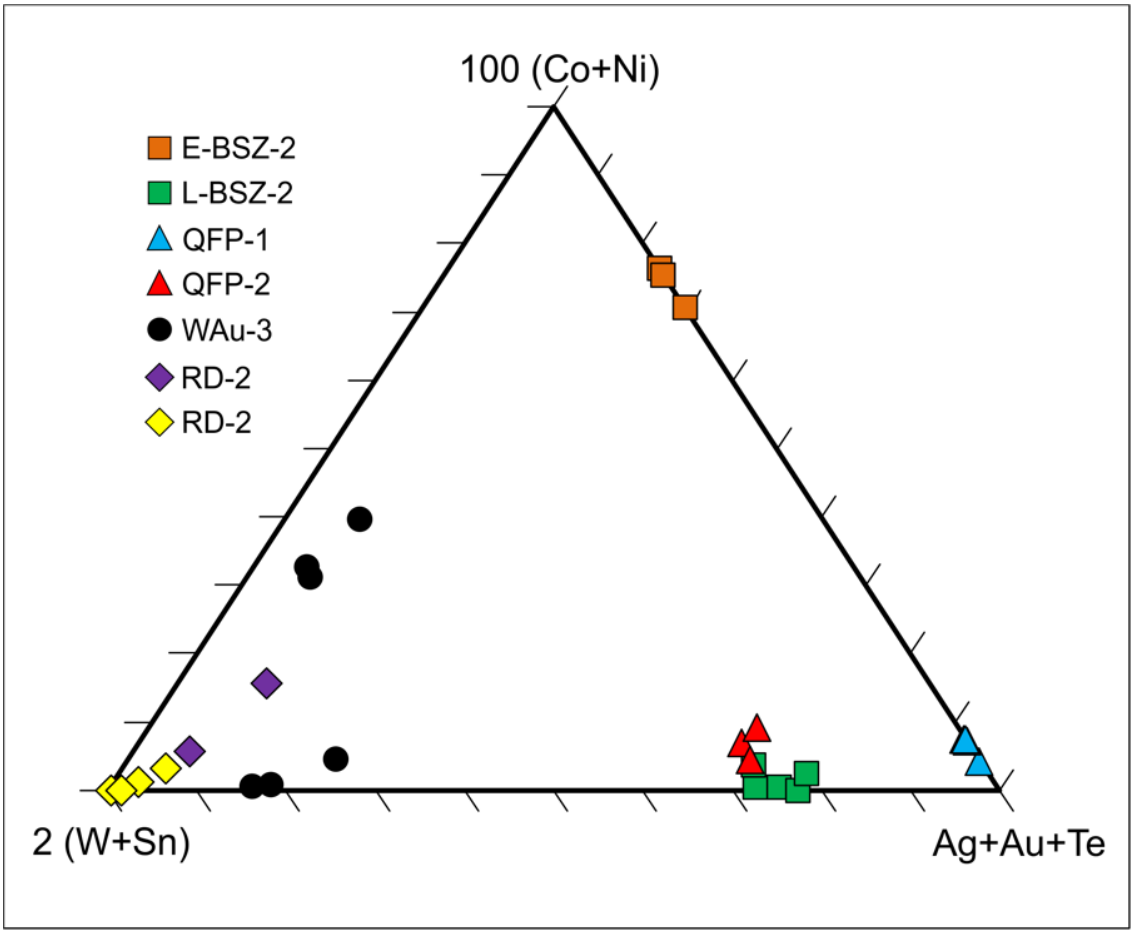

Figure 17. Chalcopyrite trace element compositions of samples analysed via LA-ICP-MS. Values bdl were treated as 0 ppm.

Pyrite demonstrates weaker compositional distinctions and illustrates a possible trend in the trace element that also follows the original hypothesis (Fig. 18). The early style 1 mineralization is shows enrichments in both Co-Ni and Ag-Au-Te along the Co-Ni to Ag-Au-Te join, tending towards the epithermal-porphyry apex. The late style 1 mineralization forms a distinct compositional domain in the center of the ternary that slightly favours the Ag-Au-Te affinity relative to other element enrichments. The QFP pyrite compositions are generally distinct with the least altered QFP (sample QFP-1) showing a large spread in data between the Ag-Au-Te and the W-Sn affinities. The large spread appears to be due to the presence of inclusions in pyrite (therefore not dissolved, homogeneously distributed elements in pyrite), though the number of data points may not be enough to state this conclusively. In comparison, the QFP-2 sample of cubic pyrite shows a compositional range of analyses along the Co-Ni and Ag-Au-Te segment with proximity to the Co-Ni apex. Pyrite from style 2 mineralization of the WAu breccia occurs in a field tending towards the Co-Ni apex, with one possible outlier occurring closer to the W-Sn apex. The disseminated pyrite of the least altered Revenue diatreme (RD-1) shows a compositional span along the Co-Ni to Ag+Au+Te join, with the majority closest to the Co-Ni apex. The style 3 mineralization of the Revenue diatreme shows pyrite occurring in a small field near the Ag-Au-Te apex.

A weak trend from early and late style 1 mineralization, as well as style 2, suggests a fluid source that evolved from an epithermal affinity to a mixed source and then to a Co-Ni dominant fluid (mafic magmatic association ?) over the course of mineralization. Style 2 mineralization appears similar to the least altered Revenue diatreme pyrite composition, though style 2 pyrite mineralization differs greatly from style 3 mineralization of the

Revenue diatreme sample RD-2, which has an epithermal-porphyry precious metal-like signature (the Au-Ag-Te association).

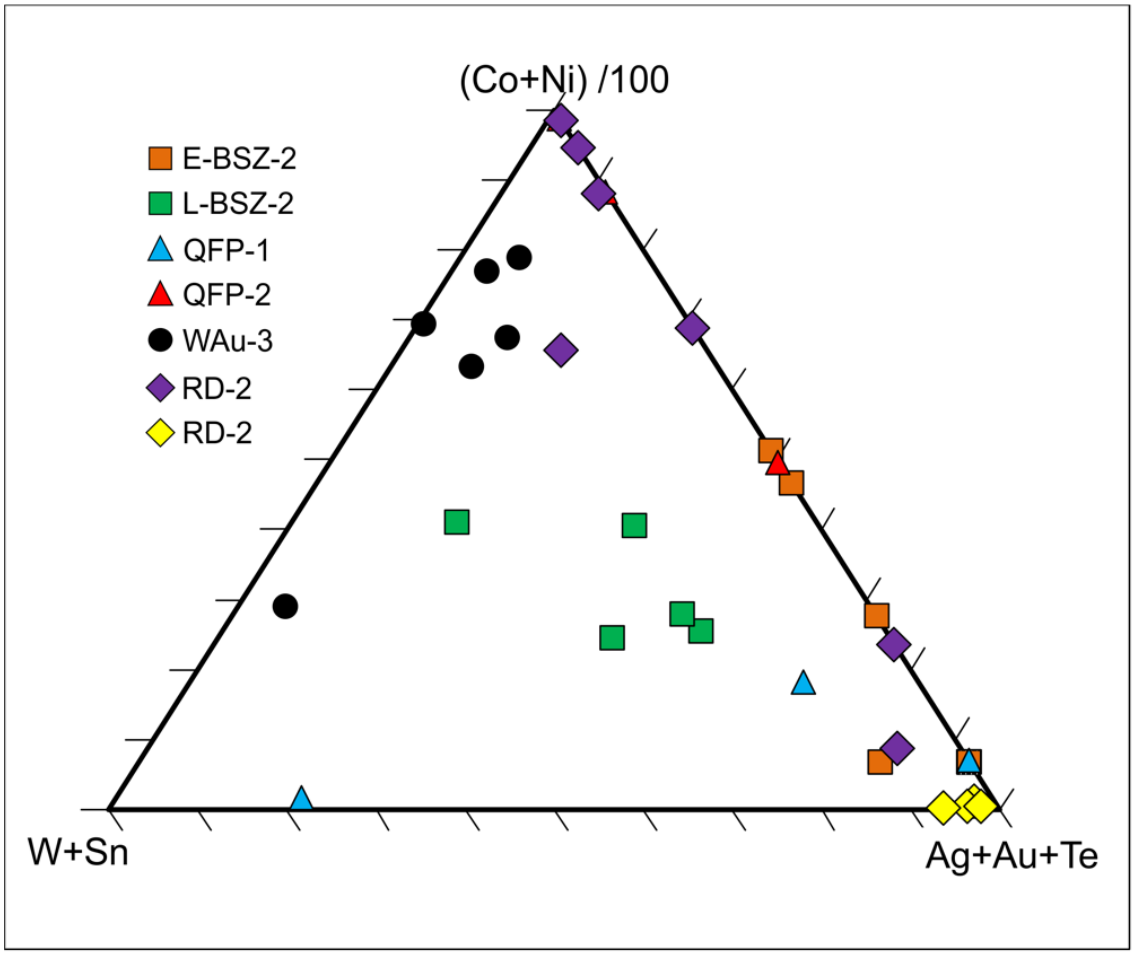

Figure 18. Pyrite trace element compositions of samples analysed by LA-ICP-MS. Values bdl were treated as 0 ppm.

The analyses of pyrrhotite showed less variation (Fig. 19). In the early style 1 mineralization, the analyses show a spread from the W-Sn and Co-Ni to the Co-Ni and the Ag-Au-Te segments. The late style 1 mineralization shows a spread along the Co-Ni to Ag-Au-Te segment, with one analysis occurring near the Ag-Au-Te apex. The QFP sample that contained pyrrhotite (sample QFP-1) shows a similar spread along the same region, though concentrated more in the Co-Ni region. Like the QFP sample, style 2 mineralization occurred on the Co-Ni and Ag-Au-Te segment with the analyses concentrated towards the Co-Ni end-members. Pyrrhotite occurs only in trace amounts in late style 1 mineralization, and the preference towards Au-Ag-Te demonstrates that this pyrrhotite is not remobilized from the early style 1 mineralization. Alternatively, the spread-out data may represent Au-Ag nugget effect in the late style 1 mineralization. Other notes from the trace element abundances show the late BSZ having the least amount of Se and Sn, and the highest amounts of Au. The results show the early style 1 mineralization occurring from a magmatic to skarn type of fluid, with all other mineralization deriving from a magmatic-epithermal fluids. More analyses would help constrain relationships and determine outliers.

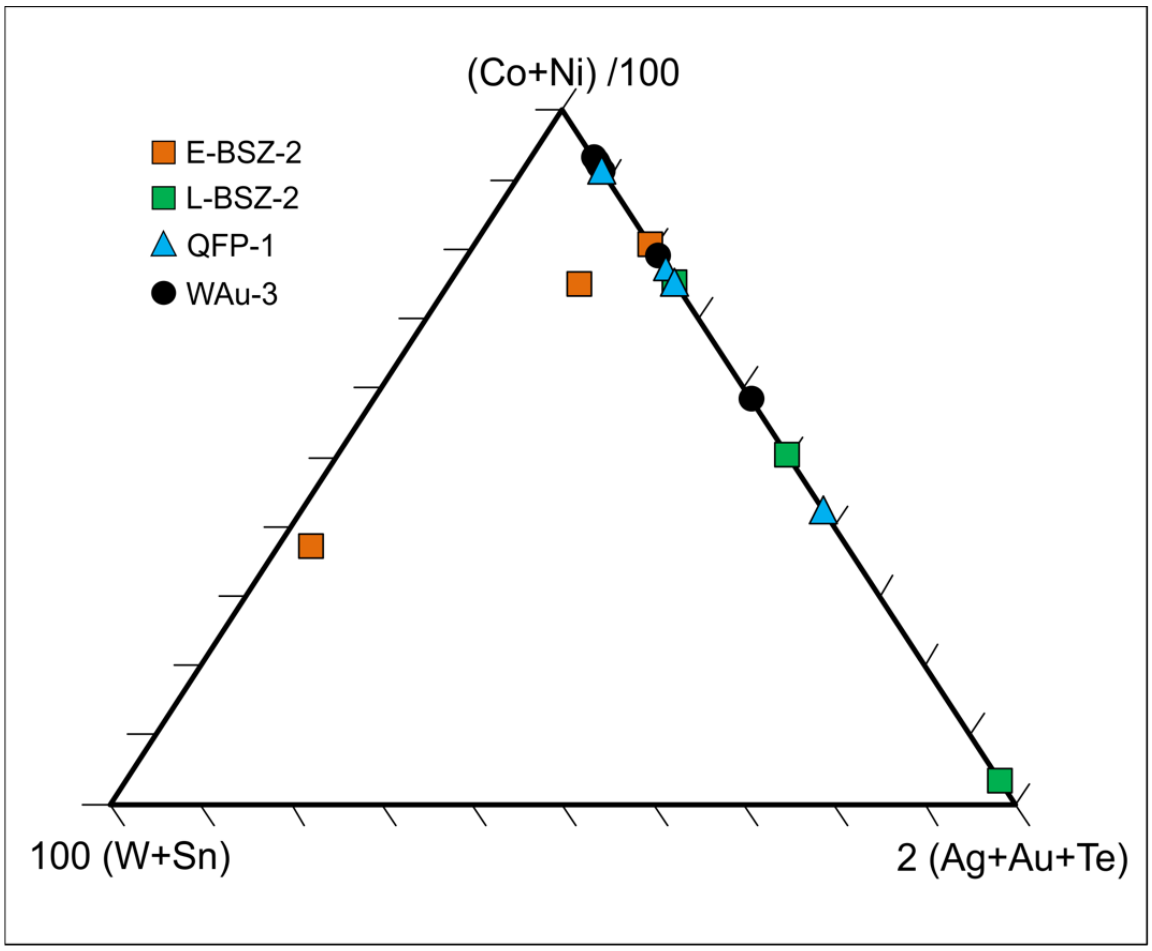

Figure 19. Pyrrhotite trace element compositions of samples representing the early style 1 mineralization, late style 1 mineralization and style 3 mineralization. Values bdl were treated as 0 ppm.

Throughout the analyses, the early style 1 is dominantly (early BSZ) magmatic in origin, the late style 1 mineralization (late BSZ) demonstrates a varying epithermal to magmatic origin, and the style 3 (WAu breccia) is influenced by skarn-type conditions when compared with each other. This may indicate that the mineralization style 1 has two metal and fluid sources that each have distinct chemical compositions, or that one source has changed in composition between mineralization events. Late style 1 mineralization crosscuts the phyllic-altered QFP. Style 2 and 3 share similar compositions in chalcopyrite, which may suggest a similar fluid source, with a separate overprinting fluid source related to pyrite deposition. The topic is discussed further in the paragenesis section.

6.2 Thermometry and barometry

6.2.1 Sphalerite thermometry

Thermometric determinations using the FeS content of sphalerite in equilibrium with pyrrhotite and/or pyrite was obtained from the late BSZ (L-BSZ-1) and from the WAu breccia (WAu-3). By plotting the calculated mole % of FeS obtained by EMPA on the composition-temperature plot from Scott (1983) for the Fe-Zn-S system (Fig. 20), the late BSZ yielded crystallization temperatures for sphalerite from 601-611°C whereas the WAu breccia yielded temperatures from 610 - 647°C.

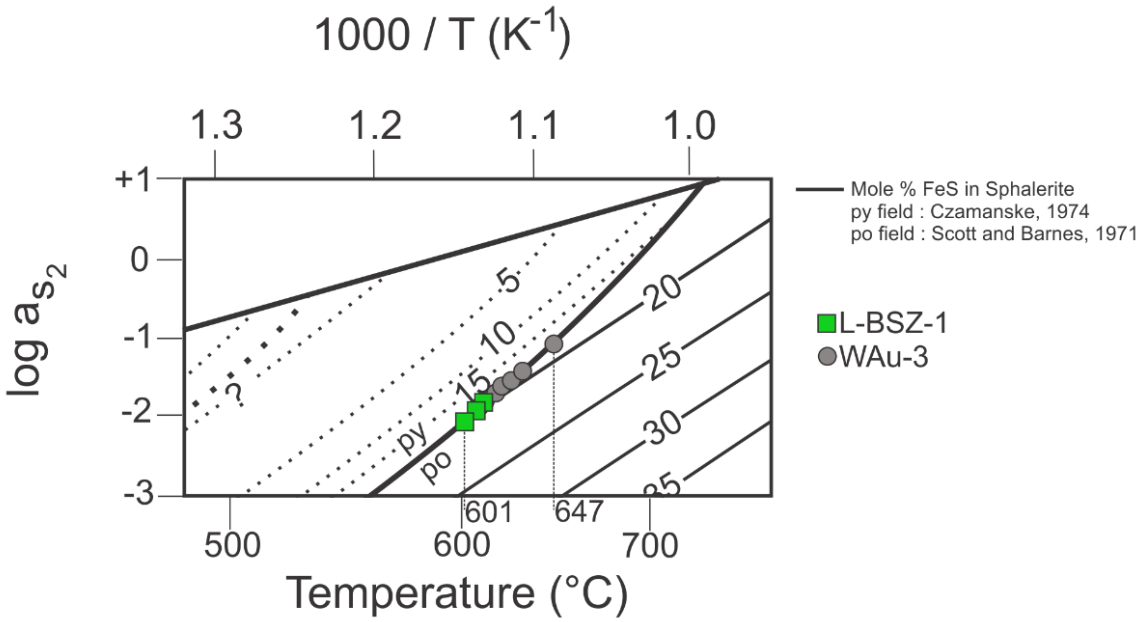

Figure 20. Sphalerite thermometry plot. Sphalerite grains in equilibrium with pyrite and pyrrhotite in the late style 1 mineralization (sample L-BSZ-1) and style 2 mineralization (sample WAu-3) yield compositions indicative of temperatures 601 - 611°C and 610 - 647°C, respectively. Adapted from Scott, 1983.

The sphalerite grains that yield the reported temperature range are texturally and compositionally similar in that they are subhedral to anhedral, and contain Sn-rich zones or inclusions. Bulk values of Sn determined by EMPA from sample WAu-3 range from bdl – 5.602 wt% Sn and values determined by SEM-EDS from three points in late BSZ sample L-BSZ-1 range from 0.17 – 1.43 wt%, and another point with a value of 0.98 wt% from late BSZ sample L-BSZ-2.

Similarly, SEM analysis of sphalerite in equilibrium with pyrrhotite and/or pyrite show Sn-rich areas with up to 11 wt% Sn in the late BSZ (L-BSZ-1) (Fig. 11G), 7.1-20.2 wt% Sn in sphalerite grains of the WAu breccia sample WAu-3, and one spot with 0.8 wt% Sn in Revenue diatreme sample RD-1. The high concentrations of Sn are restricted to specific spots and are likely areas containing Sn-rich microinclusions, or possibly some Sn in solid solution (e.g., as the mineral stannite occurring in solid solution with sphalerite; Cook et al., 2009). Overall, the Sn in the sphalerite does not appear to be homogeneous given the exsolution textures (Figs. 21AB) and the range in wt% composition. More thorough analysis via LA-ICPMS may be able to resolve the nature of its enrichment and homogeneity if transient count rates for Sn are continuous and without concentration "spikes" in signal intensity (Cook et al., 2009).

Both the sphalerite from L-BSZ-1 (Fig. 21A) and WAu-3 (Fig. 21B) are subhedral to anhedral and have diffuse boundaries with the pyrite and pyrrhotite. This may represent a disequilibrium texture, rending the temperatures calculated erroneous. In comparison, sphalerite grains elsewhere in sample WAu-3 are euhedral to subhedral (Fig. 21C), have distinct boundaries (Fig. 21D), and occur on the edges of chalcopyrite and/or massive pyrite grains, showing better textural evidence for equilibrium. These sphalerite grains do not report Sn in their trace mineral composition when analysed via SEM-EDS, nor show the

brighter greyscale areas typical of concentrated Sn when imaged in SEM-BSE (Fig. 21D). Unfortunately, microprobe analysis of the non-Sn-enriched sphalerite did not yield FeS values that could be used for thermometric estimates due to FeS values too low as a result of high Cu content (see Appendix 6).

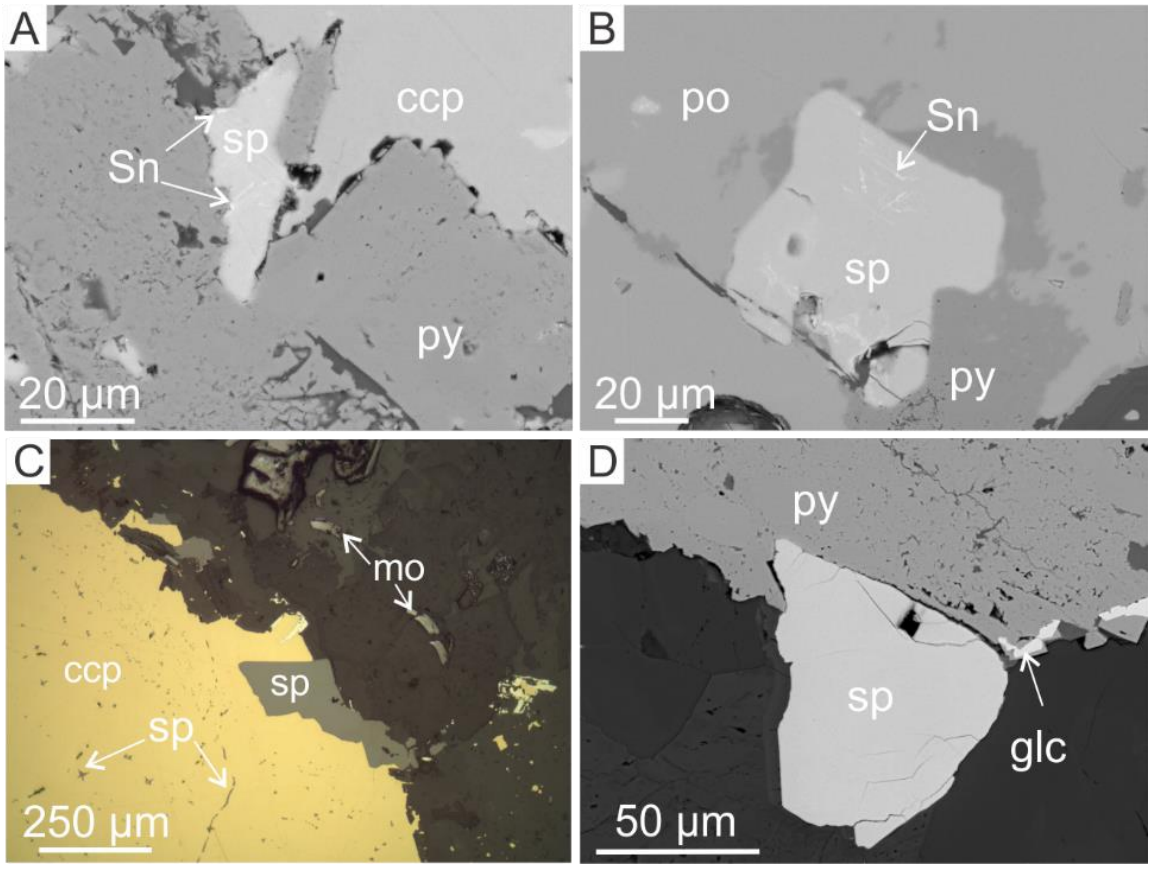

Figure 21. Comparison of sphalerite grains used in thermometry. A) SEM image of the analyzed sphalerite grain with heterogeneous concentrations of Sn in equilibrium with pyrite in the late BSZ, sample L-BSZ-1. B) SEM image of an analyzed sphalerite grain with concentrated enrichment of Sn surrounded by pyrite and pyrrhotite in the WAu breccia, sample WAu-3. C) Euhedral to subhedral sphalerite grain partially included in massive chalcopyrite, and smaller inclusions of sphalerite in massive chalcopyrite, sample WAu-3. D) SEM image of a sphalerite grain similar to that of C, showing distinct boundaries with pyrite and no enrichment of Sn, sample WAu-3.

Enrichments in Sn have been documented in sphalerite, particularly by Ono et al. (2003) in the epithermal polymetallic Suttsu deposit, Japan, that have a temperature range of . In that deposit, In-enriched sphalerite also shows minor amounts of Sn in the range of 1.8-4.3 wt%. Cook et al. (2009) document high levels of Sn (598-11703 ppm) in In-rich sphalerite from the Toyoha epithermal vein deposit, Japan (2009). The work of Cook et al. (2009) shows that from a range of deposit types, Sn in sphalerite is more enriched in epithermal deposits compared to skarn and stratabound (carbonate replacement deposits, VMS) deposits.

The enrichment of Sn in sphalerite commonly has a positive correlation to In, Ag, and Cu (Cook et al., 2009). Tin and Ag occur in solid solution at near equal proportions and are likely incorporated via a coupled substitution, with mechanisms that may involve vacancies depending on the oxidation state of Sn (Cook et al., 2009). Ohta (1995) notes the complexities of solid solutions in the Toyoha deposit involving the Ag-Cu-(Fe)-Zn-In-Sn-S system (Cook et al., 2009), leading to the identification sphalerite-stannite solid solution, a system that may be relevant to the samples in this study showing highly elevated Sn contents in sphalerite

To date there is no robust correlation between Sn composition in sphalerite and thermometry from Sn-enriched sphalerite in the Fe-Zn-S system, though Shimizu and Shikazono have proposed sphalerite and stannite (Cu_2FeSnS_4) as a means for thermometry (1985) where later studies have used this method with success (Kolodziejczyk et al., 2016). Unfortunately, the sole occurrence of stannite found in this study does not occur with sphalerite, but instead with galena and chalcopyrite (Appendix 4B).

6.2.2 Arsenopyrite thermometry

Arsenopyrite in equilibrium with pyrite from the sample QFP-2 was analyzed by EMPA and the determined As atomic % composition was used to estimate arsenopyrite crystallization temperature in equilibrium with pyrite using temperature-compositional data for the Fe-As-S system from Scott (1983). The temperature range for this mineralization was estimated to be between ~370 – 480 °C (Fig. 22). Multiple studies (Bineli-Betsi and Lentz, 2011; Northern Freegold Resources Ltd., 2015; Bineli-Betsi et al., 2016) propose that the breccia bodies located at the Revenue localitywere emplaced during the same events of the QFP dyke emplacements, and so the temperature of mineralization for these minerals may be compared, or used as a proxy for the temperature of mineralization for the Revenue diatreme.

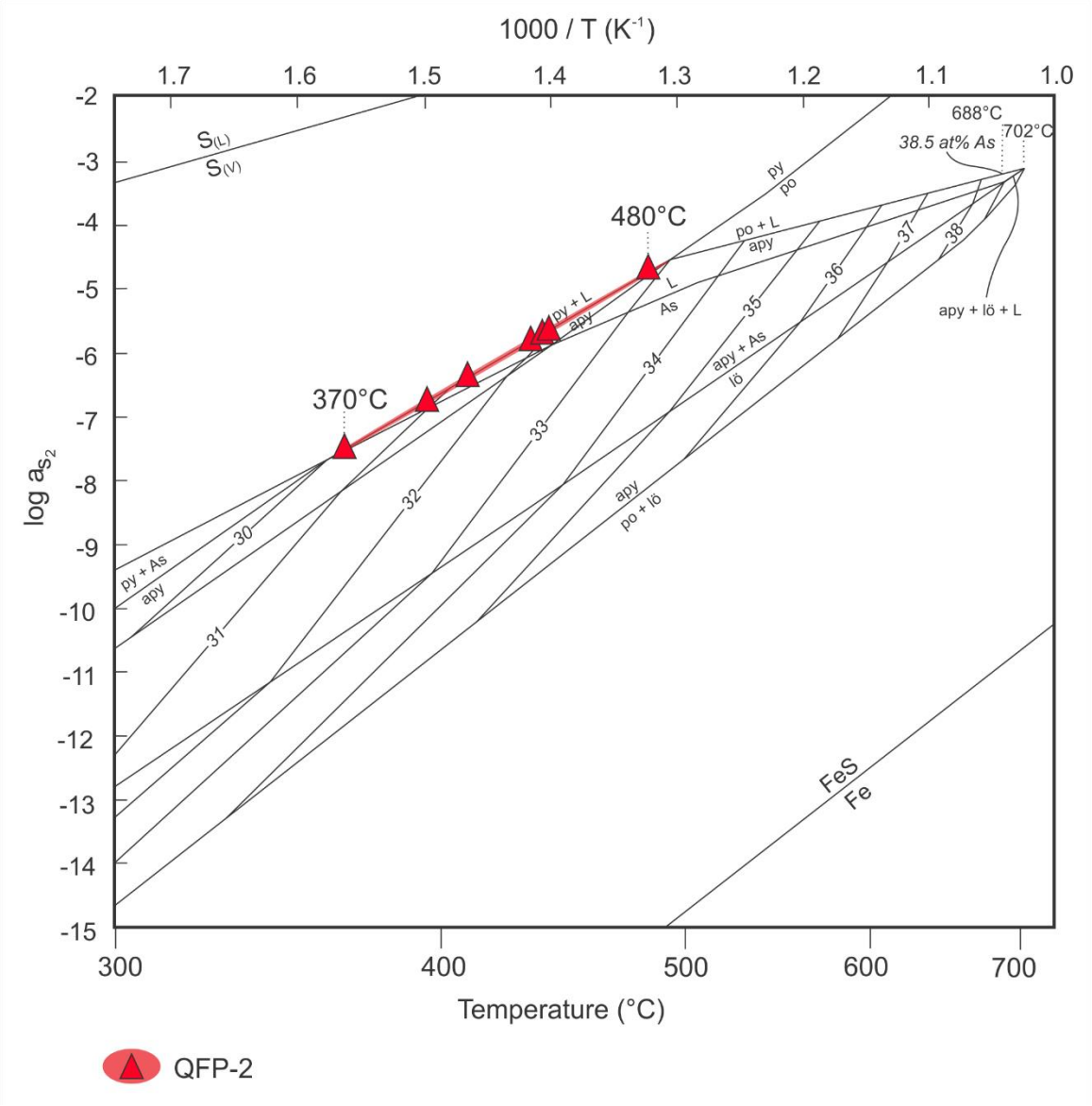

Figure 22. Arsenopyrite thermometry plot. Phase relations of the Fe-As-S system determined by the atomic percent (at %) of arsenopyrite grains, analyzed by electron microprobe. 12 analyses from QFP-2 were used to determine a window of temperatures along the arsenopyrite-pyrite equilibrium isopleth. Adapted from Scott, 1983.

6.2.3 Sulfarsenide thermometry

Plotting relative mole percent CoAsS-FeAsS-NiAsS compositions for arsenopyrite and glaucodot on an isothermal section ternary diagram for sulfarsenides (Klemm, 1965) (Fig. 23) provides a semi quantitative temperature constraint for mineralization from samples L-BSZ-2, QFP-2, WAu-2, WAu-3, and RD-2 representing the L-BSZ, QFP, WAu breccia, and Revenue diatreme respectively. Arsenopyrite from the L-BSZ-2 sample, analyzed by the SEM, yields temperatures of < 304°C. Arsenopyrite from the RD-2 sample, analyzed by SEM, yields a temperature of < 300°C. Typical arsenopyrite from the QFP-2 sample yield temperatures of < 300°C with some of the Co-Ni-rich arsenopyrite analysis yielding a higher T range from 387 to 644°C, with less confidence in the later due to wide spread in chemical composition. Glaucodot from the WAu-2 and WAu-3 samples, analyzed by Dalhousie microprobe, yields temperatures of 300 - 462°C. The plotted values are compared to field from sulfarsenides in various deposit settings (Fig. 23).

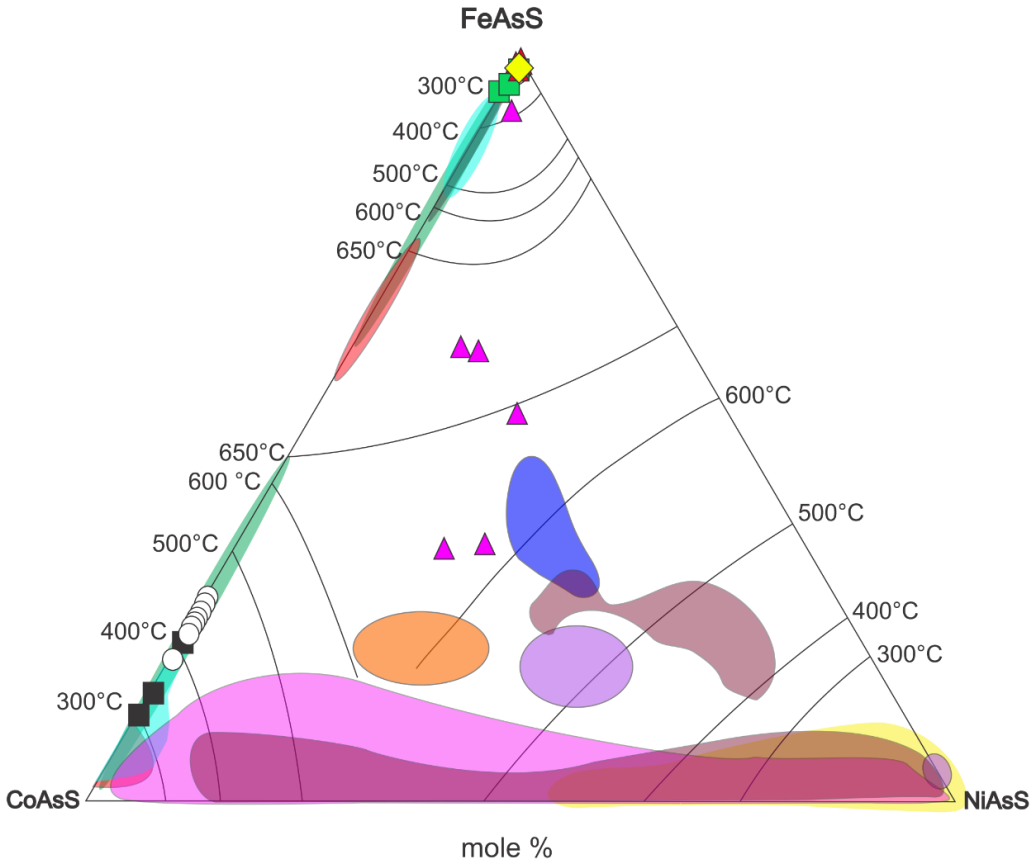

Samples	Minerals
L-BSZ-2*	apy
QFP-2*	apy
QFP-2	Co-Ni-apy
WAu-2	glc
WAu-3	glc
RD-2*	apy

Deposit fields

- Polymetallic - Copper Pass, Canada
- Polymetallic - Blanchet Island, Canada
- Pb-Zn-Ba-F Vein- Scar Crag, England
- Skuterud Cobalt - Modum, Norway
- Fe-W-Cu-Skarn - Traversella, Italy
- Ni-Cu-PGE - Sudbury Basin, Canada
- Magmatic Ni-Cu - Abitibi, Canada
- Rosie Ni - Western Australia
- Black Shales - San Juan de Plan, Spain
- NICO - NWT, Canada

Figure 23. Sulfarsenide thermometry plot. Sulfarsenide ternary using mole % Fe-Ni-Co, adapted by Klemm, 1965. Arsenopyrite grains from L-BSZ-2 and RD-2 were analyzed by SEM. Arsenopyrite grains from QFP-2 were analyzed by Toronto microprobe. Glaucodot from WAu-2 and WAu-3 samples were analyzed by Dalhousie microprobe. Sulfarsenide compositions from various types of deposits are compared with this studies results as fields, (Acosta-Góngora et al., 2015; Burke 2019; Dare et al., 2010; Fanlo et al., 2014; Godel et al., 2012; Grorud et al., 1997; Hanley 2007; Ixer et al., 1979; Klemm 1965; Nimis et al., 2014; Vander and Andre 1991). Values bdl were treated as 0 ppm. Note that arsenopyrite analyses detected via SEM from samples L-BSZ-2 and QFP-2 may appear obscured by sample labels for RD-2 arsenopyrite analyses.

Those that show compositional (and therefore, thermometric) similiary to the glaucodot of this study include the Scar Crag polymetallic arsenide-sulfarsenide vein in English Lake District (Ixer et al., 1979) and Fe-Cu-W-skarn of the Traversella deposit, Italy (Nimis et al., 2014). The Scar Crag occurrence is situated in lower Ordovician marine sediments of the Skiddaw slates and loosely classified as related to stratabound vein deposits (Stanley and Vaughan, 1982; Shepherd and Waters, 1984), though little documentation has been done to resolve the origin of the Scar Crag occurrence. More broadly, the English Lake District comprises multiple type of mineralization, including barite-fluorite vein mineralization, Carboniferous-age Zn-Pb vein mineralization, and tungstate-mineralization associated with peraluminous granites intruding deep marine sediment (Stanley and Vaughan, 1982; Shepherd and Waters, 1984). The English lake district is located roughly 50 km SE of the stratabound Alston Block mineralization of the Northern Pennines Orefield (Bouch et al., 2008), and may be genetically related (Ixer et al., 1979). The Traversella deposit have temperatures from 300 - 450°C using composition data from arsenopyrite and cobaltite mineralization from the sulfidation stage (Nimis et al., 2014), though the authors firmly note that there is no trace of glaucodot or gersdorffite found in samples. Additionally, authors make note of cobaltite paragenesis being further confined to ~300°C based on Fe-poor composition of monoclinic pyrrhotite, of which has temperature estimates of 225°C to 315°C (Nimis et al., 2014). Though mineralization styles from porphyry-style, polymetallic, and magmatic-derived Ni-Cu deposits were not plotted in similar locations, this may be a result of lack of studies in this region of work, or lack of accessible published literature.

6.2.4 Semi-quantitative fluid inclusion microthermometry

Fluid inclusions from late style 1 mineralized veins appear to comprise different generations. In the quartz-sulfide veins of sample L-BSZ-1, the dominant types of fluid inclusions were two phase (liquid "L" and vapour bubble "V"; at room T) generally rounded in shape, < 5 - 12 µm in diameter, with a ~25 to 40 vol.% vapour bubble, and showing some evidence of post-entrapment modification (stretching /necking down). These inclusions typically occur in trails, constituting secondary assemblages (Fig. 24A) or as "fields" of unclassified origin within grains. Primary or fluid inclusions (Fig. 24B) in quartz grains are 7 - 15 µm in size, and are three phase (L+V+ halite crystal "S_1") or four phase (L+V+S_1+dark solid particle "S_2"). Vapour bubbles comprise 1 - 5 vol.% and salt crystals range from 4.8 - 33.8 area% (see Appendix 6). The corresponding salinities range from 23.5 - 57.8 wt% NaCl equivalent. The average temperature of halite dissolution, corresponding to an average salinity of 40.8±9.0 wt% NaCl eq., indicates a minimum trapping temperature of ~333°C.

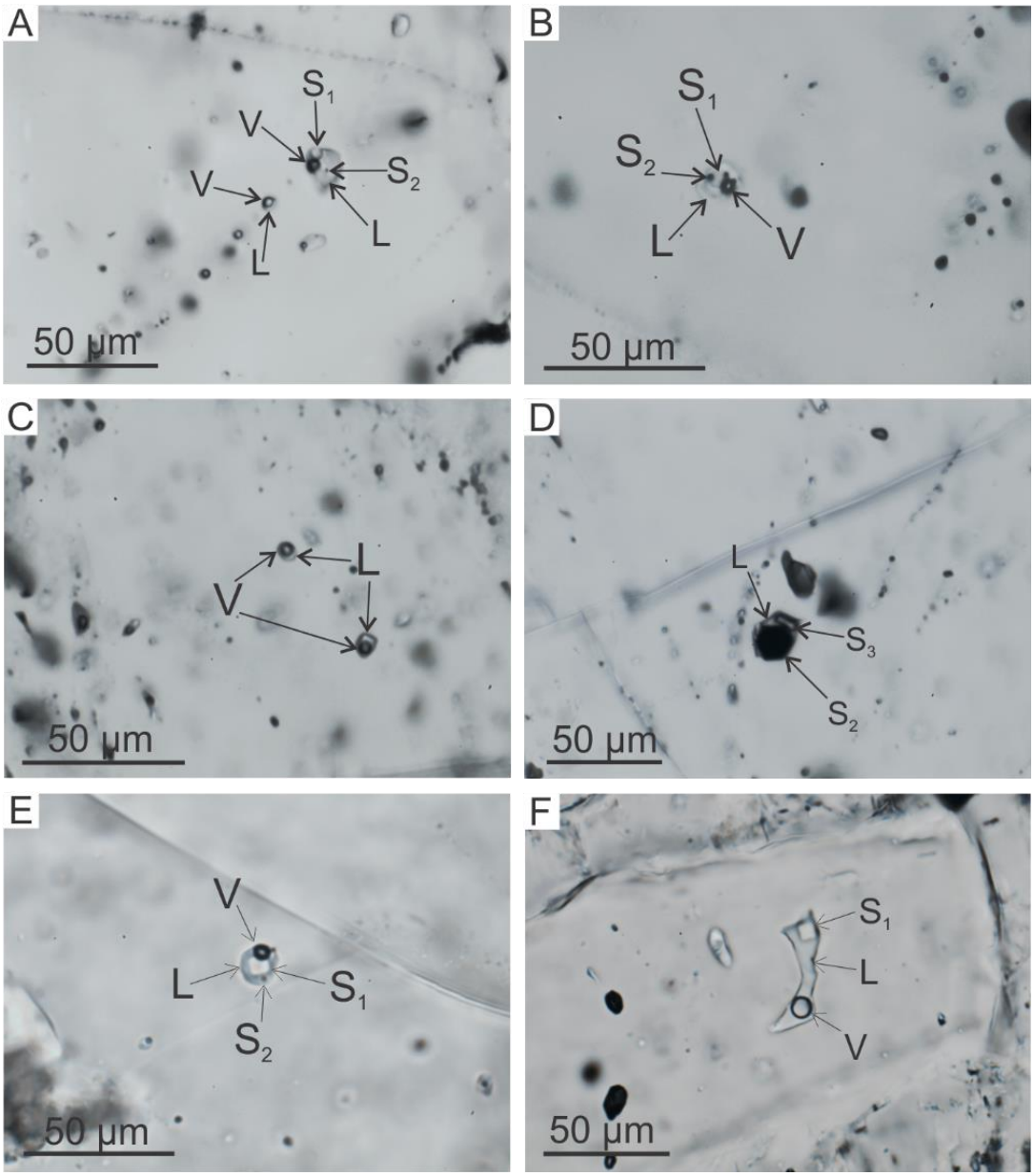

Figure 24. Fluid inclusion assemblages of samples L-BSZ-1 and WAu-3, observed in the late BSZ and the WAu Breccia respectively. A) Sample L-BSZ-1, Assemblage 3 FI#1; a four phase fluid inclusion with a salinity of 48.74 wt% NaCl eq and a trail assemblage of two phase (V+ L) fluid inclusions in the mineralized quartz vein. B) Sample L-BSZ-1, Assemblage 5 FI#2; a (primary) four phase fluid inclusion depicting a vapour bubble (V), a salt crystal (S_1), a dark sulfide solid (S_2) and a liquid (L) phase with a salinity of 32.16 wt% NaCl eq within the mineralized quartz vein. C) Sample L-BSZ-2; two phased (V+L) fluid inclusion assemblage within a quartz crystal suspended in the quartz dolomite vein. D) Sample L-BSZ-2; negative crystal shaped, three phase ($L+S_2+S_3$) fluid inclusion dominated by hexagonal sulfide grain (S_1) and unknown transparent grain (S_3). E) Sample WAu-3, Assemblage 3 FI#6; four phase fluid inclusion with a salinity of 46.86 wt% NaCl eq. F) Sample WAu-3; three phase ($V+L+S_1$) fluid inclusion assemblage within a hydrothermal apatite crystal in the quartz matrix. See Appendix 6 for data sets.

In the late style 1 mineralization sample L-BSZ-2, quartz grains are included in the mineralized dolomite veins. These quartz grains are characterized by two phase (L+V) fluid inclusion assemblages containing inclusions that are generally < 10 µm, rounded, with vapour bubbles comprising ~30 to 60 vol.% occurring in trails of secondary origin or "fields" of unknown origin (Fig. 24C), and may demonstrate necking down. Rarely, quartz grains have fluid inclusions that show negative crystal phase and contain sulfides and other unknown solid phases (S_3) within the liquid (Fig. 24D). There are no three phase fluid inclusions in the quartz-sulfide veins of sample L-BSZ-2.

Fluid inclusions assemblages found in the WAu breccia sample WAu-3 are predominantly hosted in quartz (i) of the matrix and rarely in apatite grains. Assemblages of interest are three phase ($L+V+S_1$), or four-phase ($L+V+S_1+S_2$) (Fig. 24E). Fluid inclusions of the anhedral quartz are composed of two phase secondary and pseudosecondary inclusion assemblages, and primary, three to four phase inclusions ($L+V+S_1+S_2$). The primary inclusions typically have high salt crystal volumes and so thermometry work can be approximated using the salt volume proportion compared to experimental equations for high salinity brines (J. Hanley, communication, 2018). Primary fluid inclusions measure 3 - 15 µm and may show negative crystal shape. Bulk halite area% range from 4.6 - 21.7 area%, with an average of 11.4±4.4 area%. Using the equation below, salinity yield 22.4 - 46.9 wt% NaCl eq, with an average of 34.0±6.3 wt% NaCl eq. Using the calibration of Bodnar and Vityk (1995) temperature of final halite dissolution related to salinity the average 34.0 wt% NaCl eq converts into a minimum entrapment temperature (from halite dissolution) of ~240°C.

Fluid inclusion assemblages may contain sub-µm-sized grains of an opaque solid, possibly sulfides (Figs. 24E). Other occurrences of large solid phases are noted in

assemblages 2 and 7, where a > 25 area% salt "mass" was observed. This is caused by salt crystals present in the cooling fluids being accidentally trapped within fluid inclusions, and then additional salt precipitating onto them as the inclusions cool, leading to an anomalously large salt crystal volume at room temperature. The estimated minimum trapping temperatures (> 445°C) for these inclusions were not included in the thermometry study, as their bulk salinity compositions do not reflect the true nature of the fluid at the time of entrapment.

In euhedral apatite, represented by WAu-3 assemblage #5 (Fig. 24F), fluid inclusions are three phase ($L+V+S_1$) and may be pinched in some areas. Of the two measured inclusions, salt crystals account for 6.7 and 8.5 vol% salt, corresponding to 27.3 and 30.3 wt% NaCl eq. Minimum entrapment temperatures for these inclusions are range from 73 to 171°C, based on halite size and corresponding halite dissolution temperatures. On the other end of the apatite grain, an assemblage of two phase (L+V) fluid inclusions are more uniform in phase ratios and show relatively high V:L ratios.

6.2.5 Comparisons of thermometry

The various thermometry methods are summarized in Figure 25 below. Sphalerite derived temperatures are very high in comparison to the sulfarsenide thermometry in the mineralized zones BSZ and WAu Breccia, up to 300 °C difference for sample L-BSZ. As for arsenopyrite data, the QFP area may show a temperature constrained between 363°C and 381°C using the sulfarsenide and arsenopyrite-pyrite methods together (Fig. 22), though the temperatures for the Co-Ni-enriched arsenopyrite are very high, ranging from 387 to 644°C with some analysis falling out of range of the plot (Fig. 23). Glaucodot thermometry from the WAu breccia was further constrained using fluid inclusion salinity-

T estimates (for halite dissolution), constraining mineralization in the range from 300 to 394°C.

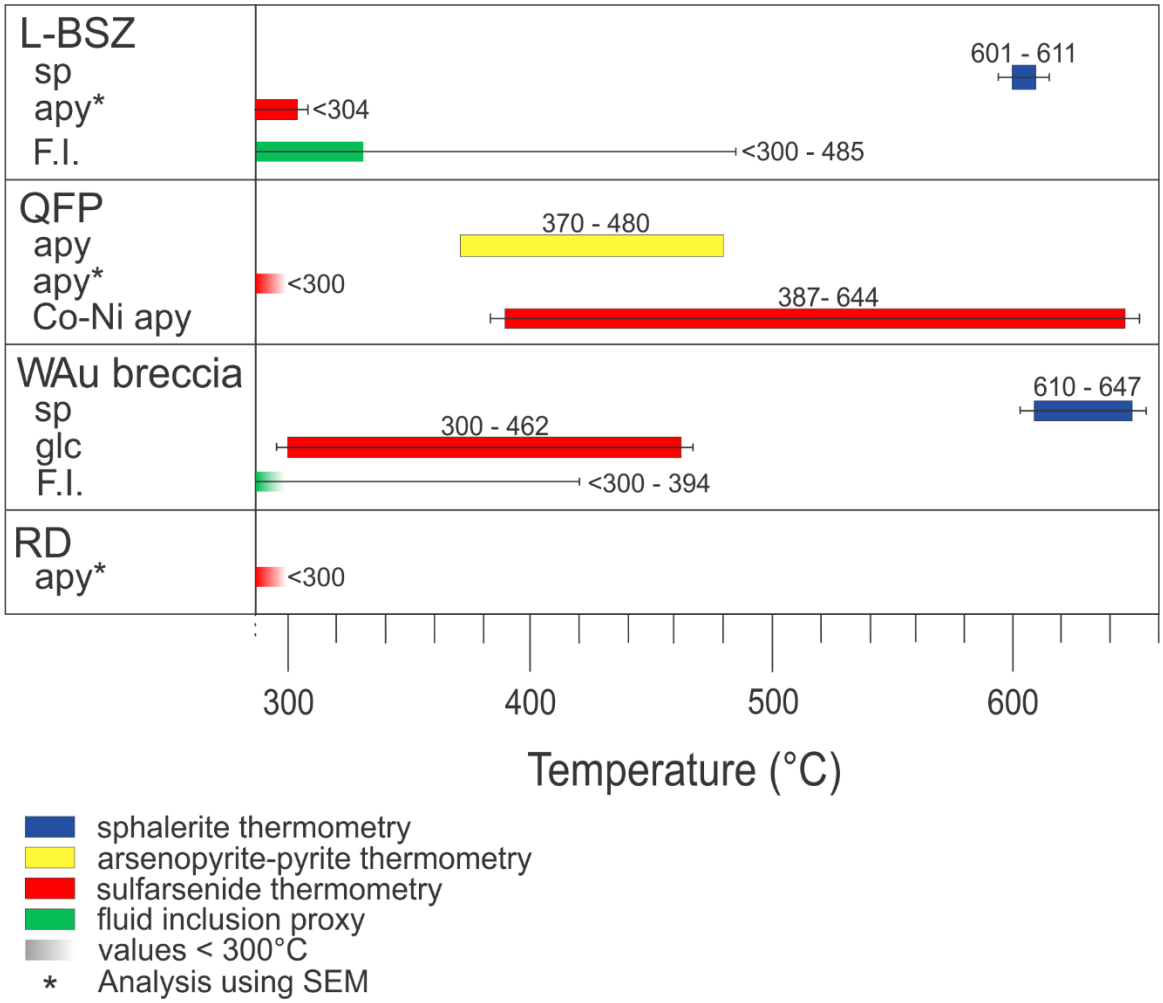

Figure 25. Thermometry summary plot of various zones using sphalerite, arsenopyrite, and glaucodot analyzed from three different methods, and fluid inclusion proxies with error bars. Sulfide data collected from EMPA unless otherwise stated.

6.2.6 Sphalerite barometry

Using sphalerite thermometry derived from mole% FeS and pairing data with Scott's barometry diagram (1983), a pressure constraint is applied for the late style 1 and style 2 mineralization of the BSZ and the WAu breccia, respectively, at deep emplacements of < 10 km (Fig. 26).

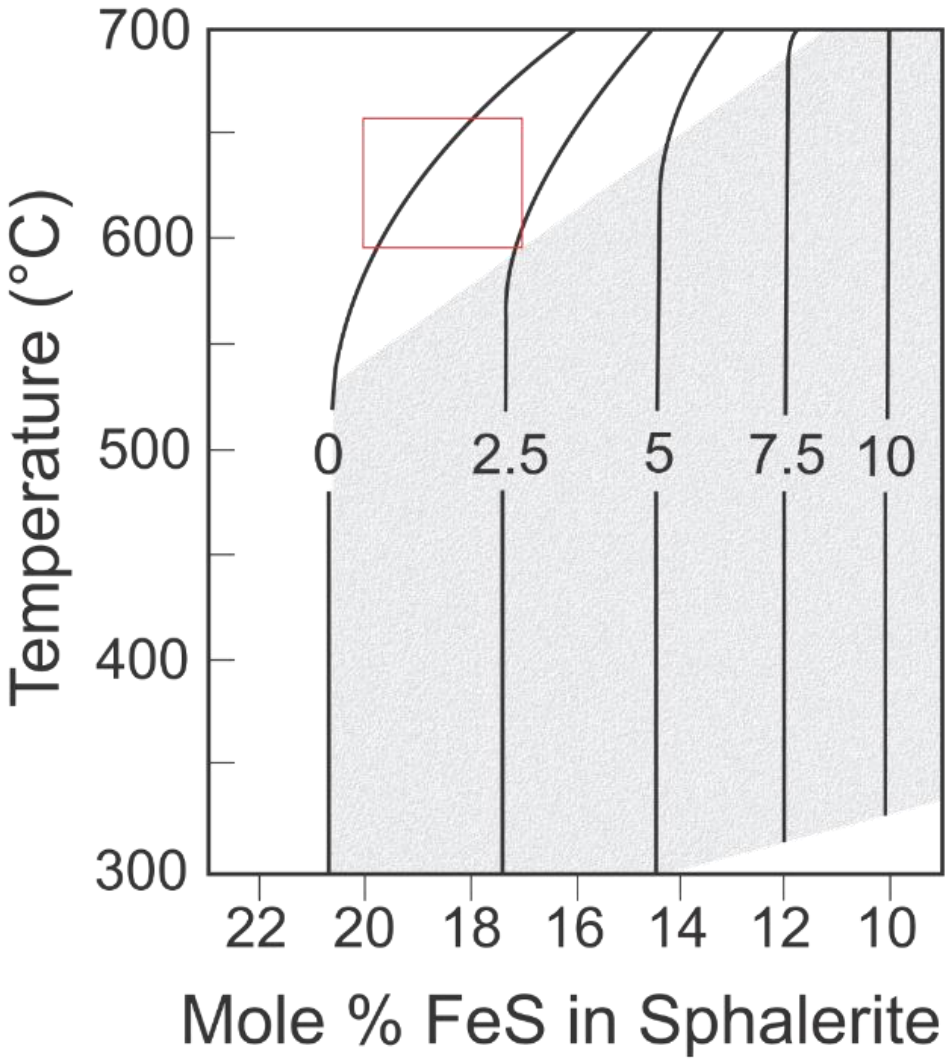

Figure 26. Sphalerite barometry plot relating molee% FeS to temperature and pressure in kbar. Red box is representative of the mole % FeS in sphalerite in addition to the thermometry derived form same sphalerite grains for L-BSZ-2 and WAu-3. Modified from Scott, 1983.

6.3 Paragenetic sequence

6.3.1 Summary of petrography

In summary, the host Revenue granite is a biotite monzogranite with predominantly disseminated sulfides accounting for ~1% modal volume sulfides. The early style 1 mineralization is dominantly biotite-altered stockwork associated with quartz (ii)-sulfide veins (~2% vol) and trace galena, sphalerite, and ilmenite. In both the host rock and early style 1, pyrrhotite is the dominant sulfide with lesser chalcopyrite, and minor amounts of pyrite. The associated alteration is dominated by fine-grained biotite and anhedral rutile.

The QFP dykes show variable intensities of mineralization associated with differing alteration intensities. Mineralization associated with the relatively unaltered areas is similar to early mineralization style 1, in that sulfides are disseminated and predominantly comprised of pyrrhotite → pyrite → chalcopyrite with chlorite-rutile alteration in the groundmass and some alteration of pyrrhotite to marcasite. The strongly altered sample mineralization is dominated by quartz (ii)-carbonate-chalcopyrite-molybdenite-rutile veins in a phyllic-altered host, which is similar to the late mineralization style 1. Chalcopyrite trace element compositions confirm that the QFP was crosscut by late style 1 mineralization.

The later mineralization style 1 consists of quartz (ii)-dolomite-sulfide veining that is dominated by chalcopyrite, lesser pyrite that is altered to marcasite, and trace to no pyrrhotite. Pyrite is categorized by pyrite (i) being smooth faced and sub-euhderal and pyrite (ii) being anhedral masses that show "picked" textures or masses of very fine-grained pyrite crystals that show colloform textures. While galena and sphalerite abundancy increases, molybdenite and arsenopyrite are introduced to the system. Trace Ag and

electrum occur with galena as fracture infill in pyrite masses. Sphalerite may show enrichment of Sn. Petrography shows two types of veining in this area: i) quartz-chalcopyrite-pyrite±molybdenite±rutile veining, and a later dolomite-chalcopyrite-pyrite-molybdenite±sphalerite±galena± trace minerals arsenopyrite, stannite, and electrum which crosscut quartz crystals from earlier veining. This sulfide assemblage is associated with phyllic alteration in the wallrocks and breakdown of euhedral rutile, chlorite, and apatite forming white clays, dolomite, siderite, and Sn-rich rutile needles.

Mineralization style 2, located in the WAu breccia, occurs in a quartz-carbonate-sulfide matrix. Alteration assemblages are more advanced than those seen in late style 1 mineralization. Plagioclase crystals are completely replaced by fine-grained white clays and turbid, anhedral siderite. Carbonate-rutile-K-spar-hydrothermal apatite assemblages occur on the margins of the quartz matrix. Mineralization is predominantly comprised of pyrite (ii) infilling spaces between pyrite (i), chalcopyrite and molybdenite, with localized ferberite-scheelite and glaucodot, and areas with coarse-grained bladed galena, Bi-enriched galena, electrum, and euhedral sphalerite.

The Revenue diatreme has variable mineralization depending on the intensity of alteration, which may be related to the distance from Revenue diatreme-granite contact. In the least altered sample, mineralisation is dominantly cubic pyrite (possible As-enriched zones; see Appendix 4E) with rutile, and rarely pyrite-sphalerite-galena-chalcopyrite-rutile. In a sample closer to contact, net-textured chalcopyrite mantled by pyrite-marcasite is dominant with inclusions of galena, sphalerite, rutile, as well as massive, fractured marcasite patches. Both locations have carbonate-rutile alteration, with W zonation in new rutile.

6.3.2 Mineral paragenesis

A summary paragenetic scheme of mineralization is shown in Figure 27, comparing relative mineral precipitation timing within each style of mineralization. Common paragenetic sequences show pyrrhotite, molybdenite, and sphalerite occurring relatively early in the sequences. Chalcopyrite, galena, and some sphalerite form throughout mineralization, as they appear as earlier than pyrite but may also form interstitial to pyrite suggesting multiple generations. In general, pyrite and rutile form relatively late in all styles of mineralization. Marcasite forms late, similar to pyrite, or may occur as a later alteration of pyrite and pyrrhotite when the system is under different conditions. Carbonate minerals occur late in the sequences with respect to mineralization, as they typically form crosscutting veins and fracture infills. When present Au occurs late in the sequence as electrum (Ag+Au) in the late style 1 and style 2 mineralization, with the latter being accompanied by calcite.

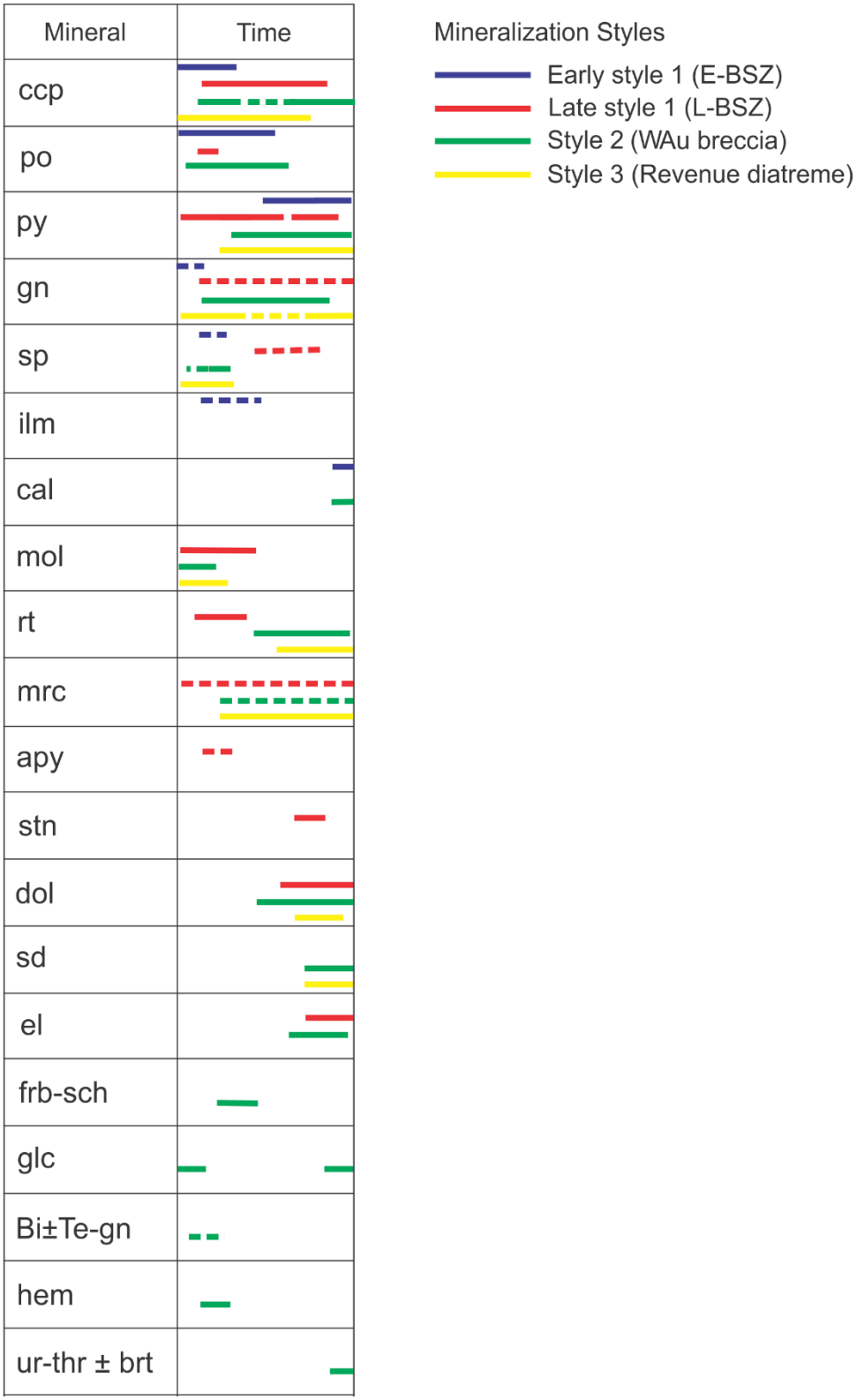

Figure 27. Comparison of mineral paragenesis of each mineralization style. Dashed lines representing uncertainties in time placement.

6.3.3 Sequence of mineralization events

Field observations show that the early style 1 mineralization of the BSZ in the Revenue granite is crosscut by the WAu breccia. Both the WAu breccia and the style 1 mineralization are then crosscut by the Revenue diatreme. This provides a preliminary basis for paragenesis of early style 1, followed by style 2, followed by style 3.

The early style 1 mineralization in the BSZ is associated with potassic alteration. This potassic alteration is overprinted by chlorite, rutile, and in some cases sulfides and calcite replacing predominantly biotite crystals. The alteration of biotite to chlorite±rutile is also observed in the least-altered QFP dyke, which strengthens theargument of the timing of QFP occurring after early style 1 mineralization, and before other mineralization and associated alteration.

Timing of QFP dykes are interpreted from petrographic and field observations. In the petrographic study, mineralization similar to late style 1 is found to vein through a QFP sample, though no chemical analyses has yet to confirm the possible genetic relation. If they are of similar mineral chemistry, this would establish QFP dykes as pre- to syn- style 1 mineralization. Additionally, fragments of QFP found in the WAu breccia suggest that the QFP dykes are pre- to syn- brecciation. Under this hypothesis, the QFP dykes would have formed likely before, or during, the early formation of both late style 1 and style 2 mineralization.

In the BSZ, late style 1 mineralization and associated alteration crosscuts the early style mineralization (Fig. 4D-F). The associated alteration shows a sequence where chlorite is altered to white clays, fine-grained anhedral dolomite is overprinted by more cubic siderite, rutile and apatite crystals are digested, and new rutile needles and euhedral apatite

crystals form. This demonstrates a previous chlorite-including alteration altered to a phyllic alteration assemblage overprinted by an argillic (illite+carbonate) assemblage.

In the WAu breccia, style 2 mineralization is associated with pervasive argillic (illite-carbonate-rutile-apatite) alteration, with no remnant textures observed in thin section. The intense alteration suggests a later timing relative to late style 1 mineralization, or fluid chemistry that has a larger alteration effect.

The diatreme and associated mineralization style 3 clearly crosscuts mineralization style 2, but shows no connection to the late style 1 mineralization. Alteration assemblages remain dominated by phyllic alteration, comparable to that of the WAu breccia.

6.4 Global mineralization comparison

The Revenue occurrence is currently classified as a Co-Au±Mo porphyry deposit as it demonstrates sheeted vein base-metal mineralization closer to the apparent core and epithermal-like polymetallic mineralization as an outwards extension into the BSZ, with associated potassic alteration overprinted by phyllic and then argillic alteration assemblages. Additionally, the Revenue occurrence is located in geological settings of island arc and extensional tectonics, like the Cu-Au porphyry deposits of the Dawson Range and in British Columbia (Kirkham and Sinclair, 2016; and references therein). The previously mentioned early pyrite-potassic alteration assemblages overprinted by later polymetallic epithermal type mineralization and associated phyllic alteration suggest that the Revenue occurrence is a telescoped system in which continuous uplift during porphyry development allowed for epithermal fluids to crosscut and mineralize as overprints to the earlier phases as it became shallowly emplaced.

Brathwaite et al. (2001) report a telescoped Cu-Mo-Au porphyry occurrence in the Thames District of New Zealand, where quartz-magnetite veins associated with hypersaline (50 – 84 wt% NaCl equivalent, corresponding to 450 to >600 °C) fluids and magnetite-K-feldspar potassic alteration are overprinted by propylitic and intermediate argillic alteration composed of quartz-chlorite-epidote-rutile-pyrite-calcite. Phyllic alteration associated with pyrite-chalcopyrite-molybdenite mineralization overprints earlier phases as veins and disseminated. This assemblage includes characteristic Cu-Mo-Au porphyry minerals such as bornite, chalcocite, and covellite, molybdenite, and inclusions of sphalerite in the dominant pyrite (Brathwraite et al., 2001; Kirkham and Sinclair, 2016). Final mineralization of quartz-sulfide-gold-anhydrite veins associated to argillic alteration cross-cut all earlier phases, contain sphalerite and galena, have temperatures from 190 to 320°C from comparisons with similar occurrences in the area (Brathwaite et al., 2001). Late carbonate as calcite or siderite with kaolinite infill fractures with. The Revenue deposit shares similarities in terms of frequent overprinting of mineralization and alteration assemblages in a similar order, with an absence of magnetite and anhydrite.

Porphyries with an absence of magnetite and anhydrite and occurrence of pyrrhotite as a major sulfide may be categorized as a subclass of porphyry deposits called *reduced porphyry deposits* (Rowins, 2000). These porphyries develop through reduced magmatic oxidation states, and are associated with ilmenite-bearing, reduced I-type granitoids with fluid inclusions rich in CH_4. Proposed mechanisms of reduced I-type granitoid formation involve magmas that were originally generated as I-type partial melts but that became strongly contaminated (and thus reduced) during assimilation of graphitic metasedimentary rocks during ascent (Auge and Brimhall, 1988; Rowins, 2000). Metal transportation involve Cu and Au transported by vapour phases following fluid boiling and subsequent

transport of metals up to several kilometers away from source porphyry magmas (Rowins 2000). This provides a possible mechanism for overprinting mineralization types in a small extent. Rowins (2000) describes 17 Mile Hill (Australia) which has similar mineralization as in the study area consisting of pyrite, pyrrhotite, chalcopyrite, marcasite, and rare sphalerite and galena in the center of quartz±carbonate±K-feldspar veins or disseminated in wallrocks in the absence of magnetite, hematite, and anhydrite. Fluid inclusion data from Rowins et al. (1993) report salinities up to 38 wt% NaCl equivalent, and mineralization temperatures ranging from 142° - 611°C, with an average at 350°C. This is comparable to fluid inclusion data in this study, with salinities up to 46.9 wt% NaCl equivalent and average temperatures around 238°C. Liberty Bell, Fort Knox, and Shot Gun porphyry deposits located in the Alaskan region of the Tintina Gold belt are also likely reduced porphyry deposits (Rowins 2000). Hart (2007) also makes note of Dublin Gulch deposit in Yukon as a reduced intrusion-related gold system.

6.5 Possible fluid sources involved at the Revenue occurrence

The small spatial extent of varying mineralizing events and their position in relation to a dilation zone within the Big Creek Fault originally suggested a genetic link between mineralization styles. In actuality, the fluid sources are diverse responsible for mineralization styles considering the contrasting trace element chemistry in conjunction with differing fluid inclusion salinities between style 1 and style 2 mineralization. Differences in the trace element composition of early and late style 1 mineralization may be explained by a common magmatic source undergoing changes in the composition during fluid exsolution. Alternatively, it is also possible that the two styles were sourced from different magmas entirely given the contrasting mineralogy.

If the system is interpreted to be a reduced porphyry, fluids associated to the late style 1 epithermal polymetallic mineralization were derived from a distant porphyry source, having travelled through the Big Creek Fault or structures associated with QFP dykes. The skarn-porphyry-affinity style 2 mineralization crosscuts the early style 1 mineralization at the center of the Revenue Granite, rather than on the flanks of the pluton like most skarn deposits. This suggests that the fluids responsible for mineralization style 2 are derived from an unknown pluton either at depth or distal to the WAu breccia location.

7.0 Conclusion

Petrograpahic, thermometric, and trace element compositional studies of the mineralization styles of the Revenue occurrence illustrate a multiphase overprinting porphyry system with main characteristics summarized below: “WAu”

1) There are 3 distinct mineralization styles
    - Style 1: an early phase represented by quartz-base metal sulfide veins associated with potassic alteration and a later, quartz-dolomite-polymetallic sulfide veins associated with phyllic alteration
    - Style 2: massive polymetallic + W mineralization in a quartz±carbonate matrix associated with pervasive argillic alteration in the “WAu” breccia
    - Style 3: replacement-style mineralization near contact of Revenue diatreme and host granite
2) Thermometry constrained mineralization conditions consistent with a high T (~400 – 600°C) porphyry environment:

- Sphalerite-pyrite-pyrrhotite thermometry gave temperatures from 601 to 611 °C for late style 1 mineralization in the BSZ and from 610 to 647 °C for mineralization style 2 in the WAu breccia zone.
- Arsenopyrite-pyrite equilibrium thermometry gave temperatures from ~370 to 480°C for late style 1 mineralization in a phyllic-altered QFP dyke.
- Sulfarsenide ternary thermometry, indicating temperatures of < 300°C for phyllic-altered QFP, < 304°C for late style 1 of the BSZ, 300 to 462°C for style 2 in the WAu breccia, and < 300°C for style 3 in the Revenue diatreme.
- High salinity fluid inclusion temperature proxies for late style 1 and style 2 mineralization constrain temperatures to minimum of 485°C and < 394°C, respectively.

3) The results of the main trace element chemistry allow differentiation of early and late style 1 and style 2 mineralization whereby early style 1 has mafic magmatic (Co-Ni) affinities, late style 1 has epithermal-porphyry precious (Ag-Au-Te) metal affinities, and style 2 has skarn-porphyry (W-Sn) affinities relative to each other.
4) Paragenesis

    Early style 1 mineralization in the BSZ of the Revenue granite was crosscut by QFP dykes, and subsequent late style 1 veining in the BSZ and style 2 in the WAu breccia. The emplacement of the Revenue diatreme and associated mineralization style 3 are the final major events in the Revenue occurrence.

This study has provided a framework for the paragenesis of three major mineralization styles, supported by thermometry, mineralogical and textural studies, and trace element fingerprinting of major sulfides. To gain a deeper understanding of the Revenue occurrence, further studies on a variety of themes would be beneficial. Detailed fluid

inclusion work on quartz phases from various styles of mineralization would strengthen the mineral thermometry of each style of mineralization and constrain more robust barometric values for mineralization. Decrepitate mound fluid inclusion analyses on L-BSZ-1 and WAu-3 may reveal the identity of unknown solid phases and confirm that the high salinity fluid inclusions are the mineralizing fluids rich in ore metals. Additional trace element work on style 1 mineralization may determine a sub-mineralization style differentiating quartz-sulfides veins from quartz-dolomite-sulfide veins. Investigations into the sources and mechanisms of Sn-enrichment in sphalerite observed in the late style 1 and style 2 mineralization may provide a stronger connection between the two mineralization events. Lastly, isotopic studies of sulfur, in conjunction with additional laser ablation mapping, would constrain sources of mineralizing fluids and better explain genetic and temporal relationships between mineralization styles.

Acknowledgements

I would like to thank Dr. Jacob Hanley and Dr. Erin Adlakha for providing me the opportunity to develop my academic and research skills, for their support, patience, and guidance, and for funding this research project. Thank you to Dr. Tony Baressi for providing me the opportunity to work on this project and contribute to the Triumph Gold Corporation team, and for funding samples and data collection. Thank you to the Triumph Gold Corporation geologists and supervisors for their knowledge and support. Thank you to Dr. Xiang Yang for assistance with the SEM-EDS analysis, Dr. Yanan Liu and Dan McDonald for assistance with the EPMA analysis, Brandon Boucher and Kevin Neyedley for assistance with LA-ICPMS analysis, and Cathy Sedge for assistance with the TerraSpec analysis. I would also like to thank my family, friends, and all staff and students of the Saint Mary's University Department of Geology for their encouragement and aid throughout the project.

References

Acosta-Góngora, P., Gleeson, S. A., Samson, I. M., Ootes, L., & Corriveau, L. (2015). Gold refining by bismuth melts in the iron oxide-dominated NICO Au-Co-Bi (±Cu±W) deposit, NWT, Canada. *Economic Geology*, *110*(2), 291-314.

Allan, M. M., Mortensen, J. K., Hart, C. J. R., Bailey, L. A., Sanchez, M. G., Ciolkiewicz, W., ... & Rusk, B. G. (2013). Magmatic and metallogenic framework of west-central Yukon and eastern Alaska. *Tectonics, Metallogeny, and Discovery: The North American Cordillera and Similar Accretionary Settings: Society of Economic Geologists Special Publication, 17*, 111-168.

AMC Mining Consultants (Canada) Ltd. (2018). Technical Report Describing Updated Diamond Drilling, Metallurgical Testing and Mineral Resources on the Klaza Property, Yukon, Canada. June 2018.

Ague, J. J., & Brimhall, G. H. (1988). Magmatic arc asymmetry and distribution of anomalous plutonic belts in the batholiths of California: Effects of assimilation, crustal thickness, and depth of crystallization. Geological Society of America Bulletin, 100(6), 912-927.

Bacon, C.R., & Lanphere, M.A. (1996). Late Cretaceous age of the Middle Fork Caldera, Eagle Quadrangle, east-central Alaska, in Moore, T.E., and Dumoulin, J.A., eds., Geologic studies in Alaska by the U.S. Geological Survey, 1994: U.S. Geological Survey, Bulletin 2152, p. 143–147.

Bineli-Betsi, T. B., & Lentz, D. R. (2010). The nature of "quartz eyes" hosted by dykes associated with Au-Bi-As-Cu, Mo-Cu, and Base-metal-Au-Ag mineral occurrences in the Mountain Freegold region (Dawson Range), Yukon, Canada. *Journal of Geosciences*, *55*(4), 347-368.

Bineli-Betsi, T. B., & Lentz, D. (2011). Petrochemistry of subvolcanic dike swarms associated with the Golden Revenue Au–Cu and the Stoddart Mo–Cu±W mineralizations (Dawson Range, Yukon Territory, Canada) and implications for ore genesis. *Ore Geology Reviews*, *39*(3), 134-163.

Bineli-Betsi, T. B., Lentz, D., McInnes, B., & Evans, N. J. (2012). Emplacement ages and exhumation rates for intrusion-hosted Cu–Mo–Sb–Au mineral systems at Freegold Mountain (Yukon, Canada): assessment from U–Pb, Ar–Ar, and (U–Th)/He geochronometers. *Canadian Journal of Earth Sciences*, *49*(5), 653-670.

Betsi, T. B., Lentz, D., Chiaradia, M., Kyser, K., & Creaser, R. A. (2013). Genesis of the Au–Bi–Cu–As, Cu–Mo±W, and base–metal Au–Ag mineralization at the Mountain Freegold (Yukon, Canada): constraints from Ar–Ar and Re–Os geochronology and Pb and stable isotope compositions. Mineralium Deposita, 48(8), 991-1017.

Bineli-Betsi, T., Lentz, D. R., & Mcfarlane, C. (2016). The Nucleus deposit: superposed Au–Ag–Bi–Cu mineralization systems at Freegold Mountain, Yukon, Canada. *Resource Geology*, *66*(4), 419-454.

Bouch, J., Naden, J., Shepherd, T., Young, B., Benham, A., McKervey, J., & Sloane, H. (2008). Stratabound Pb-Zn-Ba-F mineralisation in the Alston Block of the North Pennine Orefield (England): origins and emplacement.

Brathwaite, R. L., Simpson, M., Faure, K., & Skinner, D. (2001). Telescoped porphyry Cu-Mo-Au mineralisation, advanced argillic alteration and quartz-sulphide-gold-anhydrite veins in the Thames District, New Zealand. *Mineralium Deposita*, *36*(7), 623-640.

Burke, J.S. (2019). The origin of polymetallic Ni-Co-As-Bi-Sb(-Ag-U) veins in the East Arm basin and southern Slave Province, Northwest Territories (unpublished master's thesis). Saint Mary's University, Halifax, Nova scotia, Canada.

Carlson, G.G., 1987. Geology of Mount Nansen (115I/3) and Stoddart Creek (115I/6) map areas Dawson Range, Central Yukon. Exploration and Geological Services Division, Yukon Region, Indian and Northern Affairs Canada, Open File 1987-2, 181 p., two map sheets, scale 1:30000

Choi, S. G., & Youm, S. J. (2000). Compositional variation of arsenopyrite and fluid evolution at the Ulsan deposit, southeastern Korea: a low-sulfidation porphyry system. *The Canadian Mineralogist*, *38*(3), 567-583.

Cook, N. J., Ciobanu, C. L., Pring, A., Skinner, W., Shimizu, M., Danyushevsky, L., S.E. Bernhardt, & Melcher, F. (2009). Trace and minor elements in sphalerite: A LA-ICPMS study. *Geochimica et Cosmochimica Acta*, *73*(16), 4761-4791.

Dare, S. A., Barnes, S. J., Prichard, H. M., & Fisher, P. C. (2010). The timing and formation of platinum-group minerals from the Creighton Ni-Cu-platinum-group element sulfide deposit, Sudbury, Canada: Early crystallization of PGE-rich sulfarsenides. *Economic Geology*, *105*(6), 1071-1096.

Eaton, W.D., 1982. Nat Joint Venture, geological and geochemical report, Nitro 1-24 Claims (Archer, Cathro & Associates (1981) Ltd.). Yukon Energy, Mines and Resources Assessment Report 091438, 26 p.

Fanlo, I., Subías, I., Gervilla, F., Paniagua, A., & García, B. (2004). The composition of Co–Ni–Fe sulfarsenides, diarsenides and triarsenides from the San Juan de Plan deposit, central Pyrenees, Spain. *The Canadian Mineralogist*, *42*(4), 1221-1240.

Foster, H.L. (1970). Reconnaissance geologic map of the Tanacross quadrangle, Alaska: U.S. Geological Survey, Miscellaneous Geologic Investigations Series Map I-593, scale 1:250,000.

Foster, H.L. (1976). Geologic map of the Eagle quadrangle, Alaska: U.S. Geological Survey, Miscellaneous Geologic Investigations Series Map I-922, scale 1:250,000.

Friend, M.A., Allan, M.M., & Hart, C.J.R. (2018). New contributions to the bedrock geology of the Mount Freegold district, Dawson Range, Yukon (NTS 115I/2, 6 and 7). In: Yukon Exploration and Geology 2017, K.E. Macfarlane (ed.), Yukon Geological Survey, p. 47-68.

Godel, B., González-Álvarez, I., Barnes, S. J., Barnes, S. J., Parker, P., & Day, J. (2012). Sulfides and sulfarsenides from the Rosie nickel prospect, Duketon greenstone belt, Western Australia. *Economic Geology*, *107*(2), 275-294.

Godwin, C. I. (1976). Alternative interpretations for the Casino Complex and Klotassin batholith in the Yukon crystalline terrane. *Canadian Journal of Earth Sciences*, *12*(11), 1910-1916.

Gordey, S.P., and Makepeace, A.J. (comp.), 2003, Yukon digital geology, v. 2.0: Geological Survey of Canada, Open File 1749, Yukon Geological Survey, Open File 2003-9(D), 2 CD-ROMs.

Gordey, S.P., and Ryan, J.J., 2005, Geology, Stewart River area (115N, 115O and part of 115J), Yukon Territory: Geological Survey of Canada, Open File 4970, scale 1:250,000.

Grorud, H. F. (1997). Textural and compositional characteristics of cobalt ores from the Skuterud Mines of Modum, Norway. *Norsk Geologisk Tidsskrift*, *77*(1), 31-38.

Hanley, J. J. (2007). The role of arsenic-rich melts and mineral phases in the development

of high-grade Pt-Pd mineralization within komatiite-associated magmatic Ni-Cu sulfide horizons at Dundonald Beach South, Abitibi subprovince, Ontario, Canada. *Economic Geology*, *102*(2), 305-317.

Hart, C. J. (2007). Reduced intrusion-related gold systems. *Geological Association of Canada, Mineral Deposits Division*, *5*, 95-112.

Hem, S. R., Makovicky, E., & Gervilla, F. (2001). Compositional trends in Fe, Co and Ni sulfarsenides and their crystal-chemical implications: Results from the Arroyo De La Cueva deposits, Ronda peridotite, Southern Spain. *The Canadian Mineralogist*, *39*(3), 831-853.

Ixer, R. A., Stanley, C. J., & Vaughan, D. J. (1979). Cobalt-, nickel-, and iron-bearing sulpharsenides from the north of England. *Mineralogical Magazine*, *43*(327), 389-395.

JDS Energy & Mining, Inc. (2016). NI 43-101 Feasibility Study Technical Report for the Coffee Gold Project, Yukon Territory, Canada. January 2016.

Kirkham, B. V., and Sinclair W.D. (1996). Porphyry copper, gold, molybdenum, tungsten, tin, silver. *Geology of Canadian mineral deposit types*, 421-446.

Klemm, D. D. (1966). Synthesen und Analysen in den Dreickdiagrammen FeAsS-CoAsS-NiAsS und FeS2-CoS2-NiS2. Neues Jahrb. *Mineral. Abh.*, *103*, 205-255.

Kołodziejczyk, J., Pršek, J., Voudouris, P., Melfos, V., & Asllani, B. (2016). Sn-bearing minerals and associated sphalerite from lead-zinc deposits, Kosovo: An electron microprobe and LA-ICP-MS study. Minerals, 6(2), 42.

MacKenzie, D., Craw, D., and Finnigan, C., 2014. Structural controls on alteration and mineralization at the Coffee gold deposits, Yukon. In: Yukon Exploration and Geology 2013, K.E. MacFarlane, M.G. Nordling, and P.J. Sack (eds.), Yukon Geological Survey, p. 119-131.

MacWilliam, K. R. G. (2018). The geology and genesis of the Coffee gold deposit in west-central Yukon, Canada: implications for the structural, magmatic, and metallogenic evolution of the Dawson Rage, and gold deposit models (T). University of British Columbia. Retrieved from https://open.library.ubc.ca/collections/ubctheses/24/items/1.0371172

Mortensen, J. K., Appel, V. L., & Hart, C. J. (2002). Geological and U-Pb age constraints on base and precious metal vein systems in the Mount Nansen area, eastern Dawson Range, Yukon. *Yukon Exploration and Geology*, 165-174.

Murakami, H., & Ishihara, S. (2013). Trace elements of Indium-bearing sphalerite from tin-polymetallic deposits in Bolivia, China and Japan: A femto-second LA-ICPMS study. Ore Geology Reviews, 53, 223-243.

M3 Engineering & Technology Corporation. (2013). Form 43-101F1 Technical Report Feasibility Study for the Casino Project, Yukon, Canada. January 2013.

Nimis, P., Dalla Costa, L., & Guastoni, A. (2014). Cobaltite-rich mineralization in the iron skarn deposit of Traversella (Western Alps, Italy). *Mineralogical Magazine*, *78*(1), 11-27.

Northern Freegold Resources Ltd. (2015). *Technical Report on the Freegold Mountain Project, Yukon, Canada, Resource Estimates*. Vancouver, BC: Campbell, J., Sexton, A., Armitage, A., & Studd, D.

Northern Freegold Resources Ltd. (2017). *Geology and Exploration Potential of Revenue and Nucleus* (Reduced). Barresi, T., Bradford, J. & Halle, J.

Ohta, E. (1995). Common features and genesis of tin-polymetallic veins. Resour. Geol.,

187-195.
Ono, S., Hirai, K., Matsueda, H., & Kabashima, T. (2004). Polymetallic mineralization at the Suttsu vein-type deposit, southwestern Hokkaido, Japan. *Resource Geology*, *54*(4), 453-464.
Oriolo, S., Oyhantçabal, P., Wemmer, K., & Siegesmund, S. (2017). Contemporaneous assembly of Western Gondwana and final Rodinia break-up: Implications for the supercontinent cycle. *Geoscience Frontiers*, *8*(6), 1431-1445.
Rowins, S. M., Groves, D. I., McNaughton, N. J., Brown, P. E., McLeod, R. L., & Hall, D. (1993). Evidence of unusually carbonic and reduced ore fluids in the Late Proterozoic 17 Mile Hill porphyry copper–style deposit. In Telfer district, Western Australia: 2nd National Meeting of the Specialist Group in Economic Geology: Geological Society of Australia Abstracts (Vol. 34, pp. 68-70).
Rowins, S. M. (2000). Reduced porphyry copper-gold deposits: A new variation on an old theme. *Geology*, *28*(6), 491-494.
Ryan, J.J., Colpron, M., and Hayward, N., 2010, Geology, southwestern McQuesten and parts of northern Carmacks, Yukon: Geological Survey of Canada, Canadian Geoscience Map 7 (preliminary version), scale 1:125,000.
Sánchez, M.G., Allan, M.M., Hart, C.J.R., and Mortensen, J.K., 2013, Orogen-perpendicular magnetic segmentation of the western Yukon and eastern Alaska cordilleran hinterland: Implications for structural control of mineralization, in MacFarlane, K.E., Nordling, M.G., and Sack, P.J., eds., Yukon exploration and geology 2012: Yukon Geological Survey, p. 133–146.
Scott, S. D. (1983). Chemical behaviour of sphalerite and arsenopyrite in hydrothermal and metamorphic environments. *Mineralogical magazine*, *47*(345), 427-435.
Shepherd, T. J., & Waters, P. (1984). Fluid inclusion gas studies, Carrock Fell tungsten deposit, England: Implications for regional exploration. Mineralium Deposita, 19(4), 304-314.
Shimizu, M., & Shikazono, N. (1985). Iron and zinc partitioning between coexisting stannite and sphalerite: a possible indicator of temperature and sulfur fugacity. Mineralium Deposita, 20(4), 314-320.
SKR Consulting. (2008). Technical Report on Minto Mine, Yukon (Project No. 2Cs018.007). June 2008.
Stanley, C. J., & Vaughan, D. J. (1982). Copper, lead, zinc and cobalt mineralization in the English Lake District: classification, conditions of formation and genesis. Journal of the Geological Society, 139(5), 569-579.
Staples, R.D., Gibson, H.D., Berman, R.G., Ryan, J.J., and Colpron, M., in press, A window into the Early to mid-Cretaceous infrastructure of the Yukon-Tanana terrane recorded in multi-stage garnet of west-central Yukon, Canada: Journal of Metamorphic Geology.
Tafti, R., Mortensen, J. K., Emond, D. S., & Lewis, L. L. (2003). Early Jurassic porphyry (?) copper (-gold) deposits at Minto and Williams Creek, Carmacks copper belt, western Yukon. *Yukon exploration and geology*, 289-303.
Tempelman-Kluit, D., 1984. Geology, Laberge and Carmacks, Yukon Territory. Geological Survey of Canada, Open File 1101, scale 1:250000, 2 sheets.
Vander Auwera, J., & André, L. (1991). Trace elements (REE) and isotopes (O, C, Sr) to

characterize the metasomatic fluid sources: evidence from the skarn deposit (Fe, W, Cu) of Traversella (Ivrea, Italy). *Contributions to Mineralogy and Petrology*, *106*(3), 325-339.

Vityk, M. O., & Bodnar, R. J. (1995). Textural evolution of synthetic fluid inclusions in quartz during reequilibration, with applications to tectonic reconstruction. Contributions to Mineralogy and Petrology, 121(3), 309-323.

Wagner, T., & Lorenz, J. (2002). Mineralogy of complex Co-Ni-Bi vein mineralization, Bieber deposit, Spessart, Germany. *Mineralogical Magazine*, *66*(3), 385-407.

Zajzon, N., Szentpéteri, K., Szakáll, S., & Kristály, F. (2015). The origin of the Avram Iancu U–Ni–Co–Bi–As mineralization, Băiţa (Bihor) metallogenic district, Bihor Mts., Romania. *International Journal of Earth Sciences*, *104*(7), 1865-1887.

Appendices

Appendix 1: list of abbreviations for mineralized zones and minerals

Minerals	Abbreviation
albite	ab
allanite	aln
andesine	andes
anorthoclase	ano
apatite	ap
arsenopyrite	apy
barite	brt
bioite	bt
carbonate	cb
calcite	cal
cassiterite	cst
chalcopyrite	ccp
chlorite	chl
dolomite	dol
electrum	el
ferberite	frb
galena	gn
glaucodot	glc
hematite	hem
illite	ilt
ilmenite	ilm
kaolinite	kln
K-feldspar	kfs
marcasite	mrc
molybdenite	mol
monzanite	mnz
muscovite	ms
oligoclase	olg
plagioclase	pl
pyrite	py
pyrrhotite	po
quartz	qz
rutile	rt
scheelite	sch
siderite	sd
sphalerite	sp
stannite	stn
thorite	thr
titanite	ttn
urainite	urn
xenotime	xtm
zircon	zrn

Appendix 2: Regional mineralization comparison

As previously stated in the introduction, the Revenue occurrence is located in the Dawson Range portion of the Tintina Gold belt adjacent to the Carmacks Copper Belt. Deposits in the area are commonly located along the Big Creek Fault, or off-shoots of the dominant fault, and may have QFP dykes of the Casino Pluton cross-cutting properties and associated to mineralization (Allan et al., 2013; Betsi et al., 2016). Below are five recognized mineral occurrences and deposits situated in the Dawson Range, organized spatially closest to Revenue to further away in the NW direction.

Nucleus

The Nucleus deposit, situated ~3 Km west of Revenue, is defined as a "superposed Ag-Au-Bi-Cu mineralized system" that has two non-genetic mineralization styles of i) skarn and sulfide replacement (~182 - 191 Ma) and ii) vein-controlled, breccia and disseminated mineralization (75.8 - ~76.2 Ma; Bineli-Betsi et al., 2013, 2016). The skarn mineralogy and abundance of pyrrhotite in both skarn and vein-controlled mineralization share characteristics with reduced Au skarns and reduced Au-Co porphyries (Bineli-Betsi et al., 2016). Skarn mineralization has been compared to the Minot Cu-(Au) deposit aged at 182 ± 1 Ma, and is interpreted to have a blind intrusions as fluid sources. Bineli-Betsi et al. justify the vein-controlled mineralization style to be a low sulfidation deposit formed at levels between classic porphyry and epithermal deposits owing to the mineralization textures and mineral chemistry (2016). Key characteristic of the Nucleus deposit are shared with the Revenue deposit for example, arsenopyrite thermometry in the vein-controlled mineralization has nearly the same temperature range as the QFP in this study at 340-491°C, native Au grains may be associated with Bi and depletion in Ag, and elevated Fe

content in sphalerite (Bineli-Betsi et al., 2016). Mechanisms of mineralization are attributed to precipitation upon cooling and neutralization of magmatic-hydrothermal fluids in the skarn mineralization and cooling of hydrothermal fluids in vein-controlled mineralization (Bineli-Betsi et al., 2016).

Klaza

The Klaza Project, located ~20 km south of the Revenue deposit (Fig. 1), is an Au-Ag breccia/sheeted vein classified as a Carbonate Base Metal deposit, subclass of epithermal deposits (AMC Consulting, 2018). The Klaza deposit is closely related and situated immediately north of the Mount Nansen Camp. Host rocks of the Dawson Range Batholith and Mount Nansen Volcanic are later cross-cut by west oriented Casino Plutonic suite volcanic, which are hypothesized to be the heat source for hydrothermal cells associated to mineralization and dated to 78.2 – 76.3 Ma by Mortensen et al. (2002). Like Revenue, mineralization occurs in veins and breccias with strong associated and possibly controlled by QFP dykes. Here, the mineralization shows weak zonation of a Cu-Mo porphyry core extending to sheeted veins and breccias that host base metals and precious metals including disseminated to semi-massive pyrite, arsenopyrite, galena, sphalerite, stibnite, jamesonite, and precious metals as native Au and electrum and gangue minerals include quartz, carbonates, and barite (AMC Consulting, 2018). Mineralization in hydrothermal channels are associated to potassic and sericitic alteration, with weak argillic alteration occurring in the host rocks (AMC Consulting, 2018). Magnetite is replaced by sulfides in mineralized structures. The CBM deposit models include processes of rising mineralized fluids mixing with colder bicarbonate waters (AMC Consultants, 2018).

Minto and Carmacks Copper

The Minto and Carmakcs Copper (formally Williams Creek) deposits lie north of the Revenue occurrence ~33 km (Fig. 1) and are situated in intrusive plutons age dated to 198-197 Ma (Tafti and Mortensen, 2003). The Minto mine is a loosely defined as a Cu-Au porphyry deposit, with characteristics that are shared with alkali porphyry copper, magnetite skarn, and iron-oxide copper gold deposits (SKR Consulting, 2008). Mineralization at Minto is predominantly chalcopyrite with zones enriched in bornite and Au-Ag associated to potassic alteration consisting of magnetite and biotite (Tafti and Mortensen, 2003; SKR Consulting, 2008). Mineralization is associated with occurs as disseminate grains, along foliation planes in gneiss host rocks, or as semi-massive textures intergrown with silicate minerals (Tafti and Mortensen, 2003). At Carmacks Copper, Cu mineralization is predominantly supergene Cu-oxides (SKR Consulting, 2008). Mineralization at this site also includes rare amounts of molybdenite and pyrrhotite, posing an unknown source of sulfide minerals (Tafti and Mortensen, 2003). Authors hypothesize the deposit formed as an early-stage porphyry deposit due to Cu mineralization associated with potassic alteration, but suggest that "porphyry system development was arrested due to deep (~8.5 km) conditions based on magmatic epidote occurrences" (Tafti and Mortensen, 2003). Occurrences of pyrrhotite continue to be unexplained with suggestions of forming syngenetic to schist in the area (SKR Consulting, 2008).

Casino

The Casino Deposit, located 95 km WNW (Fig. 1), has similar history and mineralization to the Revenue complex. The complex is characterized by supergene and hypogene mineralization, with a focus on hypogene porphyry-style mineralization and intrusive contact-breccia mineralized zones (M3 Engineering & Technology Corporation, 2013). Both hypogene mineralization (porphyry and breccia) are genetically linked to hydrothermal fluids from the Casino Plutonic Suite (M3 Engineering & Technology Corporation, 2013), dated to ~74. 4+/-0.28 Ma. Mineralization is postulated to be affected by the dominant Casino Creek Fault that runs through the property and a parallel fault, called the Patton Fault (M3 Engineering & Technology Corporation, 2013).

Like Casino, Revenue-Nucleus areas have remnant oxide cap present, though at a much less extent than that of Casino due to erosion (M3 Engineering & Technology Corporation, 2013). The main comparison in this study is between the mineralization style and associated alterations of the hypogene and associated intrusive breccia. Hypogene mineralization includes an early mineralization of disseminated pyrite-chalcopyrite-molybdenite+/-sphalerite+/-bornite, associated with potassic biotite-K-Feldspar-magnetite alteration (M3 Engineering & Technology Corporation, 2013). Differing from that, the Revenue occurrence includes major pyrrhotite and trace galena rather than molybdenite and bornite in the early mineralization and does not include magnetite in the alteration, instead rutile. The later mineralization event includes increased Au, Cu, molybdenite, and W values in the surrounding phyllic altered section (M3 Engineering & Technology Corporation, 2013), which is comparative to late style 1 mineralization at Revenue. Additionally, phyllic alteration at Casino includes tourmaline which is not present at Revenue. The intrusive breccia mineralization has similar mineralogy to the WAu breccia,

with the addition of bornite and tetrahedrite (M3 Engineering & Technology Corporation, 2013). Both breccia locations have increased pyrite:chalcopyrite phases, abundant sphalerite and galena, and introduction of coarse-grain Native Au and bismuth bearing minerals and local geochemical anomalies in W (M3 Engineering & Technology Corporation, 2013). Alteration of breccias differ, where the intrusive breccias of the Casino complex are potassically altered and the breccias at Revenue are pervasively phyllic to argillic altered. Additionally, the intrusive breccias at Casino are large in extent and volume, whereas the WAu breccia at Revenue is mapped to relatively small based on current knowledge. The Casino complex deposit model follows the hydrothermal fluids in the Casino Plutonic Suite mobilized through structures from the intrusive breccias at the contact zone of pluton and host rocks, resulting in highest grade mineralization characterized by chalcopyrite nad molybdenite in the contact breccias and lower grades characterized by dominant pyrite as one moves towards the core porphyry zone and into the host rock (M3 Engineering & Technology Corporation, 2013).

The Casino Complex and Revenue occurrence share similarities in paragenesis and mineralization, though there are discrete differences in mineralogy and implied hydrothermal and mineral sources, where porphyry mineralization event, intrusion breccia mineralization, and then explosive breccias crosscutting previous units. Differently, late porphyry dykes cross-cut all units, where at Revenue QFP dykes occurred earlier in the sequences.

Coffee

The Coffee Project/ Coffee Gold Deposit is an Au deposit located ~125 km NW of Revenue occurrence (Fig. 1). The deposit formed ~98 Ma, soon after the emplacement of the Coffee Creek granite during the mid-cretaceous extension tectonics in the region. Extension activated dextral strike-slip faults hat are considered splays of the regional dominant Big Creek Fault. Mineralization occurs predominantly in the Sulphur Creek felsic gneiss and biotite schist, with strong spatial associations with fracture cross-cutting Carmacks Groups dacite and andesite dykes. Here, mineralization is structurally controlled fracture and polyphase breccia deposit where Au occurs associated to arsenian pyrite predominantly in matrixes to polyphase breccias, as fine-grained disseminations, or as biotite replacement. Mineralization is associated to illite, Fe-carbonate, and silica alteration. Arsenian pyrite forms from CO_2-As-Sb fluids.

Revenue occurrence shares few similarities to the Coffee complex, though the occurrence of sulfide-carbonate-rutile replacement of biotite are recorded in the Revenue granite host rock (Fig. 8G,H), illite-Fe-carbonate also occur in mineralization styles of high Au (late style 1, style 2), and breccias with sulfide matrices, though the composition of sulfides differs greatly.

In summary, there are broad similarities in terms of mineralization assemblages and associated phyllic alteration, and most deposits are described as being within the porphyry-family. It is interesting that Klaza is so close and has the same geology associated to mineralization, and yet this type of porphyry shows “normal” characteristic of porphyries including magnetite in potassic alteration, whereas Revenue does not have magnetite but instead pyrrhotite. Revenue also does not include bornite in the samples collected for this

study, though this Cu-rich mineral is regularly mentioned in technical reports and research papers on regional deposits. Additionally, most of the occurrences have magnetite and or biotite that is being replaced by sulfides. Similar alteration of biotite to sulfides is observed at Revenue in the least altered granite sample. Like Casino, increased Au±W occurs in strong phyllic altered section like that of the WAu breccia at Revenue.

Appendix 3: Data collection parameters for LA-ICP-MS

LA		
Model		Resonetics RESOlution M-50 with S-155 Laurin Technic cell
Wavelength		193 nm
Pulse duration (FWHM)		20ns
Repetition rate		3.0 Hz
Spot diameter		24 µm
Energy density		~3 J/cm2

ICP-MS		
Model		Agilent 7700x with dual external rotary pumps
Forward power		1500W
Sampling depth		4.0 to 5.0 mm
Gas flow rates:		
	Carrier (He)	300 mL/min
	Make up (Ar)	930 mL/min
ThO+/Th+		<0.1
U+/Th+ (NIST 610)		1.05

Data acquisition and reduction parameters	
Total sampling time	30s background, 30s transient signal
Detector mode	Dual mode
Data reduction software	Iolite platform on Igor Pro 6
Internal standardization	Fe wt% (from SEM-EDS)
Primary (calibration) standards	MASS-1
Secondary (QC) standard	NIST610, Po724
Isotopes determined (dwell time in ms)	56Fe, 24Mg, 27Al, 32S, 33S, 47Ti, 55Mn, 57Fe, 59Co, 60Ni, 65Cu, 66Zn, 72Ge, 75As, 82Se, 95Mo, 105Pd, 107Ag, 108Pd, 111Cd, 115In, 118Sn, 121Sb, 125Te, 182W, 195Pt, 197Au, 202Hg, 208Pb, 209Bi.
Quadrupole settling time	5 ms
Analysis time	background (30s), ablation (10s, 50s), washout (5s)

Appendix 4: Additional descriptions from petrography section

Appendix 4A: Early style 1 mineralization, Blue Sky Zone

Fine-grained biotite occurs much like in the Revenue granite assemblage (Fig. A-4A-A) though as denser concentrations of stockwork stringers or line boundaries between quartz (ii) and plagioclase crystals (Figs. A-4A-A,B,C). These patches are typically spatially associated with chlorite, rutile, apatite and zircon (Fig. A-4A-D,E,F), and partially or completely surround metallic minerals (Fig. A-4A-F). Chlorite is anhedral and may partially surround metallic minerals in association with calcite, and partially alters biotite grains (Fig. A-4A-E,F).

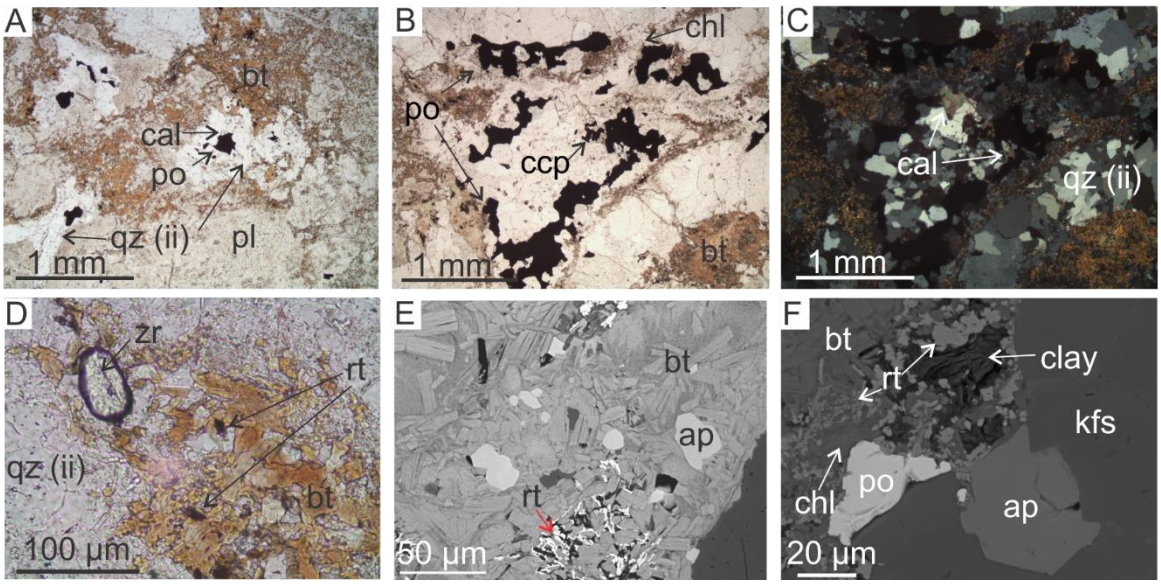

Figure A-4A. Alteration and minor minerals of the BSZ early style 1 mineralization. A) Representative potassic biotite alteration occurrence in the early BSZ, where biotite forms in patches adjacent to quartz-sulfide veins. B) Secondary biotite lining quartz-sulfide areas. C) Quartz (ii) veining in the early BSZ, associated with the mineralization. D) Zircon crystals and fine-rained rutile occurring in fine-grained biotite. E) SEM image of fine-grained biotite including apatite and fine-grained anhedral rutile. F) SEM image fine-grained biotite altered to chlorite and clay, partially including pyrrhotite and apatite.

Appendix 4B: Late style 1 mineralization, Blue Sky Zone

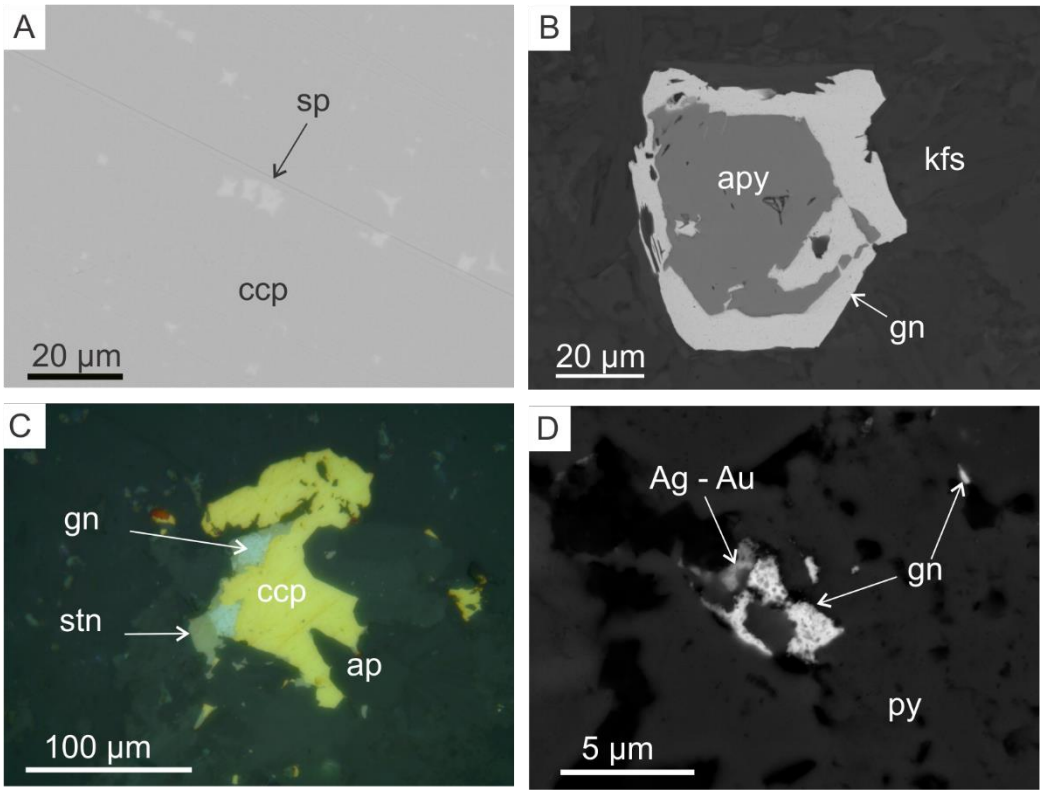

Figure A-4B-1. Trace minerals of the BSZ late style 1 mineralization. A) Sample L-BSZ-1; BSE image of X-shaped sphalerite microinclusions within anhedral chalcopyrite. B) Sample L-BSZ-2; BSE image of disseminated trace arsenopyrite mantled by galena. H) Sample L-BSZ-2; trace stannite occurring with galena and chalcopyrite. I) Sample L-BSZ-2; trace Ag-Au and galena occurring in fractures and interstitial to pyrite (i-ii).

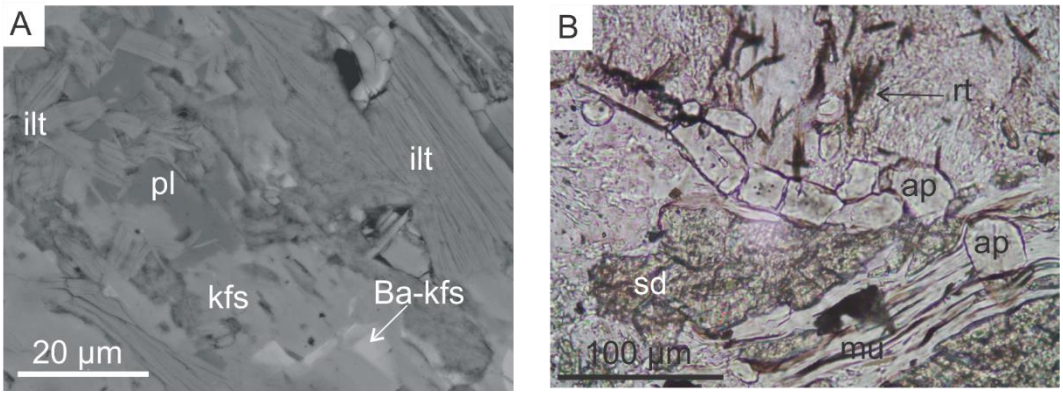

Figure A-4B-2. Alteration assemblage of the BSZ late style 1 mineralization. A) SEM close-up of clay alteration, in which illite crystals overprint primary plagioclase and K-feldspar. Some K-feldspar may have Ba-enrichment. B) Alteration assemblage apatite grains included by coarse-rained muscovite and anhedral siderite. Rutile needles form adjacent.

Appendix 4C: Quartz-feldspar porphyry dykes

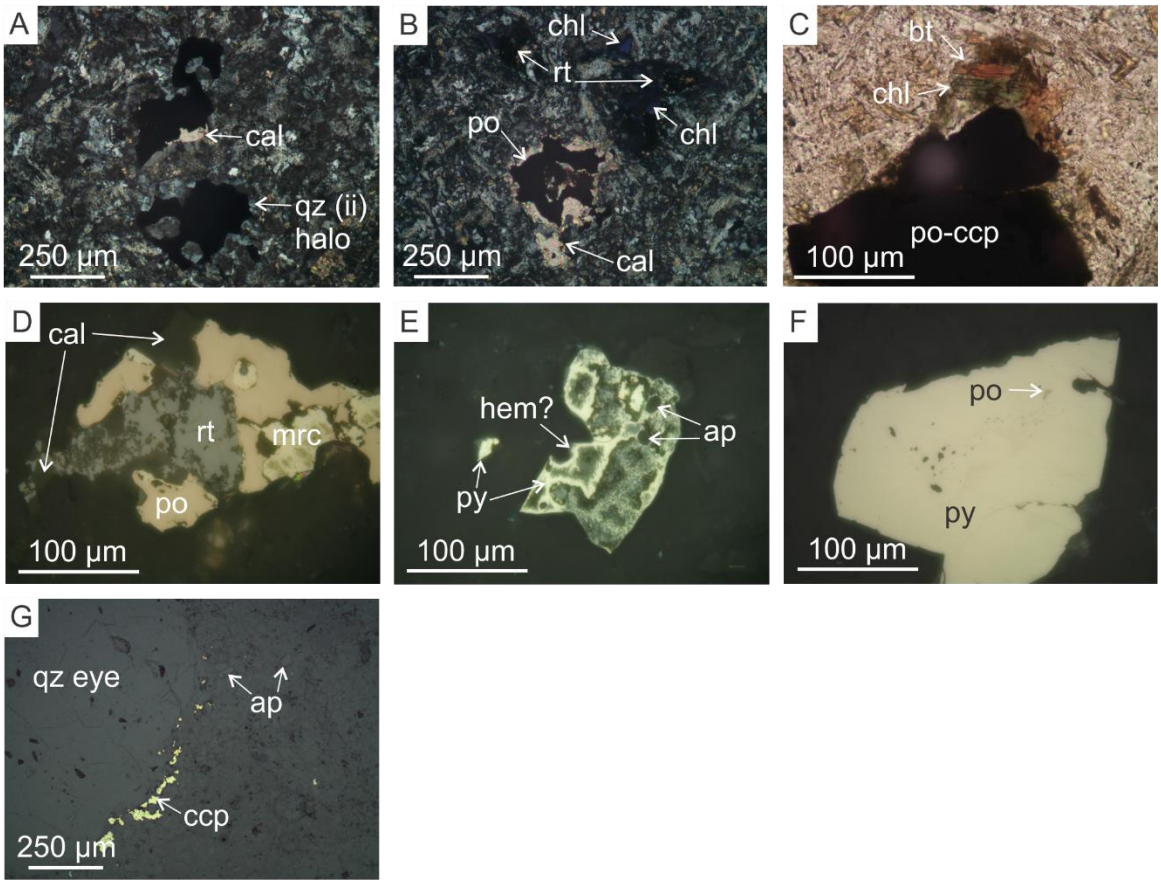

Figure A-4C. Additional petrography from the QFP dykes. A) Calcite and a quartz (ii) halo completely or partially surrounding sulfides. B) Chlorite partially or completely surrounding rutile. C) Biotite altered to chlorite on edges of mineralization. D) Pyrrhotite occurring post marcasite and anhedral rutile. E) Rare disequilibrium texture of pyrite and hematite. F) Small inclusions of pyrrhotite within subhedral pyrite. G) Chalcopyrite disseminated in QFP matrix, forming along quartz-eye margin.

Appendix 4D: WAu breccia

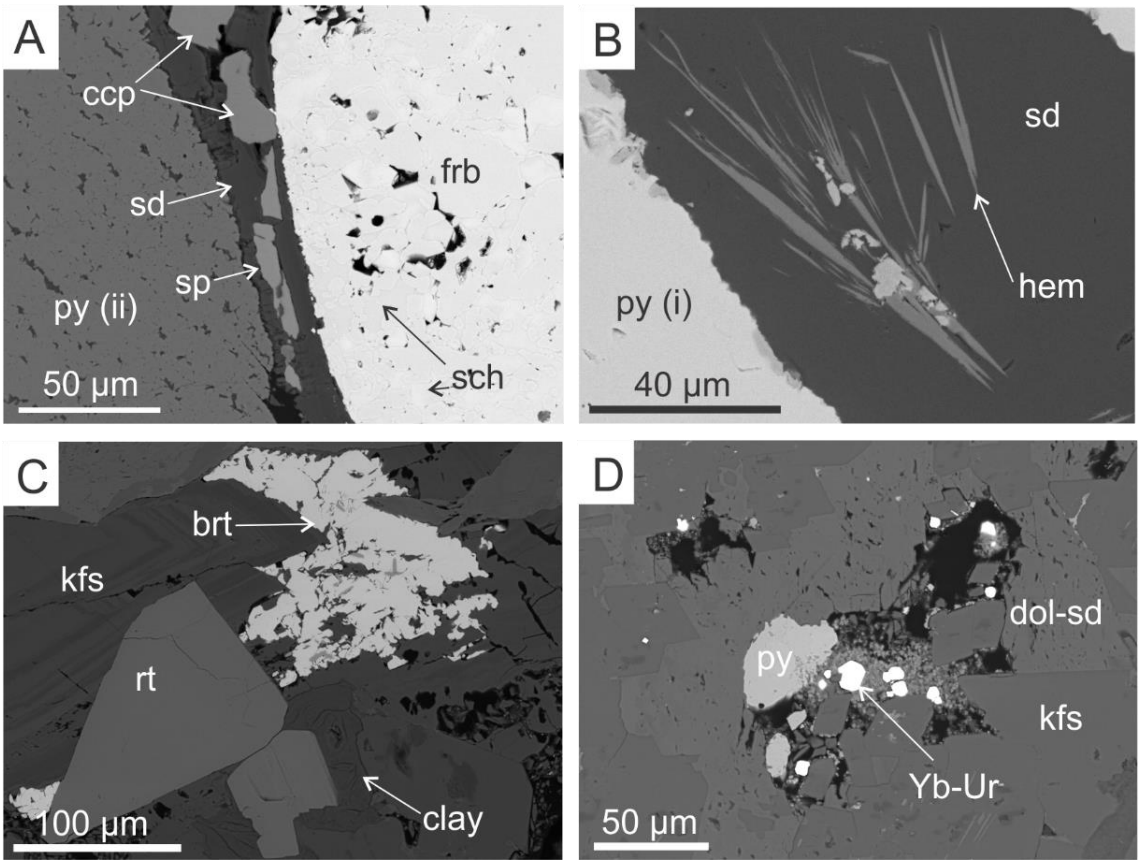

Figure A-4D. Additional petrography in the WAu breccia style 2 mineralization. A) Sphalerite and chalcopyrite forming between massive pyrite (ii) and ferberite-scheelite, suspended din siderite lining. B) Acicular hematite interstitial to massive pyrite in siderite infill. C) Late barite in matrix after K-feldspar and rutile. D) Disseminated trace pyrite and uraninite with REE mineral.

Appendix 4E: Revenue diatreme

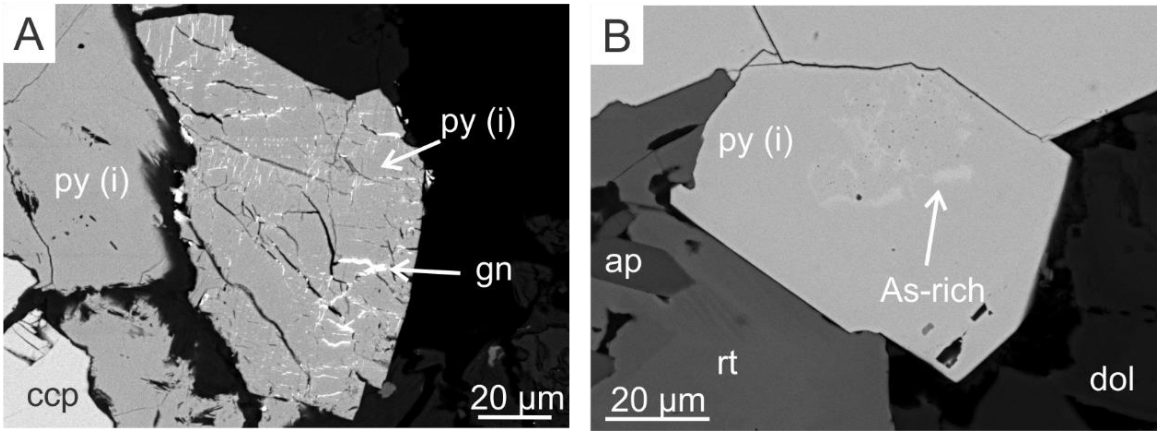

Figure A-4E. Trace mineral occurrences in the Revenue diatreme. A) As-enrichment in pyrite cubes. B) Late galena fracture infilling pyrite.

Appendix 5: Clay alteration mineralogy

The use of infrared hyperspectral imaging with a TerraSpec3® was used for mineral identification of clays in representative rocks. Clay mineralization from previous reports identified much of the clay content at the Revenue occurrence as illite and smectite (Northern Freegold Resources Ltd., 2015; 2017) with lesser amounts of kaolinite, biotite, and chlorite.

Appendix 5A: Revenue granite

In the Revenue granite host rock, clay composition is an intimate mixture of smectite, kaolinite, and biotite depicted in Figure A-5-1. These peaks do not coincide perfectly with reference material, though the deep water feature of ~1910 nm is characteristic of smectite and the tail end resembles that of kaolinite. This reading is not concurrent with petrographic work in conjunction with SEM data, as the white clay content is descriptive of illite. The doublet absorption bands at ~2201 and 2250 nm are characteristic of Al-OH and Mg-OH bonds, respectively. The presence of magnesium indicates biotite and/or chlorite, which is consistent in the petrographic works of this study though neither biotite nor chlorite have dominant signature in this sample. Pseudoreflectance for different readings yield slightly higher values than reference material with a maximum hull nearing 0.285 compared to the reference 0.25. The second complete peak in the spectra shows a greater reflectance than the main hull, which may be indicative of an intimate mixture of clay compositions. The samples show nearly the same signature with the same absorption bands but a difference in pseudoreflectance. The difference in pseudoreflectance between the two samples may be due to analysis for one analysis coming

from a rounded part of the sample block, thus the reflected light may have dispersed and not detected.

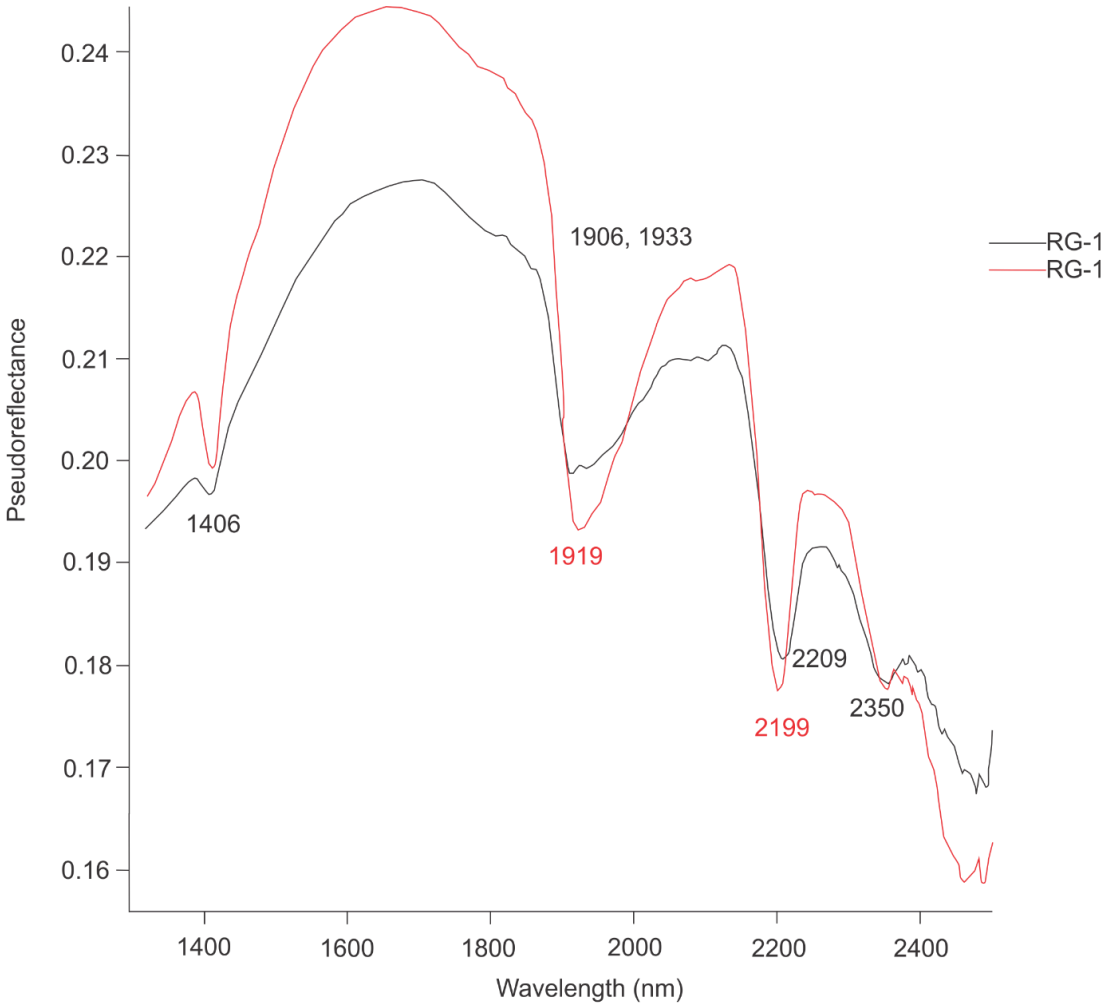

Figure A-5A. TerraSpec® spot analysis of Revenue granite (sample RG-1) obtained two sides of the sample block. Both analysis show a similar signature but with different pseudoreflectance values. A doublet of absorption bands at 2201 nm and 2250 nm is the most distinct feature. Wavelength measured in nanometers (nm). Pseudoreflectance measured out of 1.

Appendix 5B: Early style 1 mineralization, Blue Sky Zone

In the early BSZ, clay minerals are identified to be a mix of illite and biotite (Fig. A-5B). This is consistent with the petrographic work in this study and findings in Northern Freegold Resources Ltd., 2015, 2017). The signature is similar to that of sample RG-1 (Figure 16) with a deep water feature, a doublet absorption band at ~2201 and ~2250 nm, and a jagged tail end, though the depth of absorption bands ~2205 nm is deeper in these samples. The doublet absorption bands do not show similar reflectance ratios with respect to each other and may be a result of intimately mixed clay compositions. Readings E-BSZ-2 show similar pattern though the absorption bands are different widths, resulting in the spectral analysis overlapping in one area. This may be due to slightly different clay compositions from one area to the next. The pseudoreflectance of these readings were half that of reference figures, with maximum amplitudes reaching 0.24 instead of the expected 0.36 to 0.55.

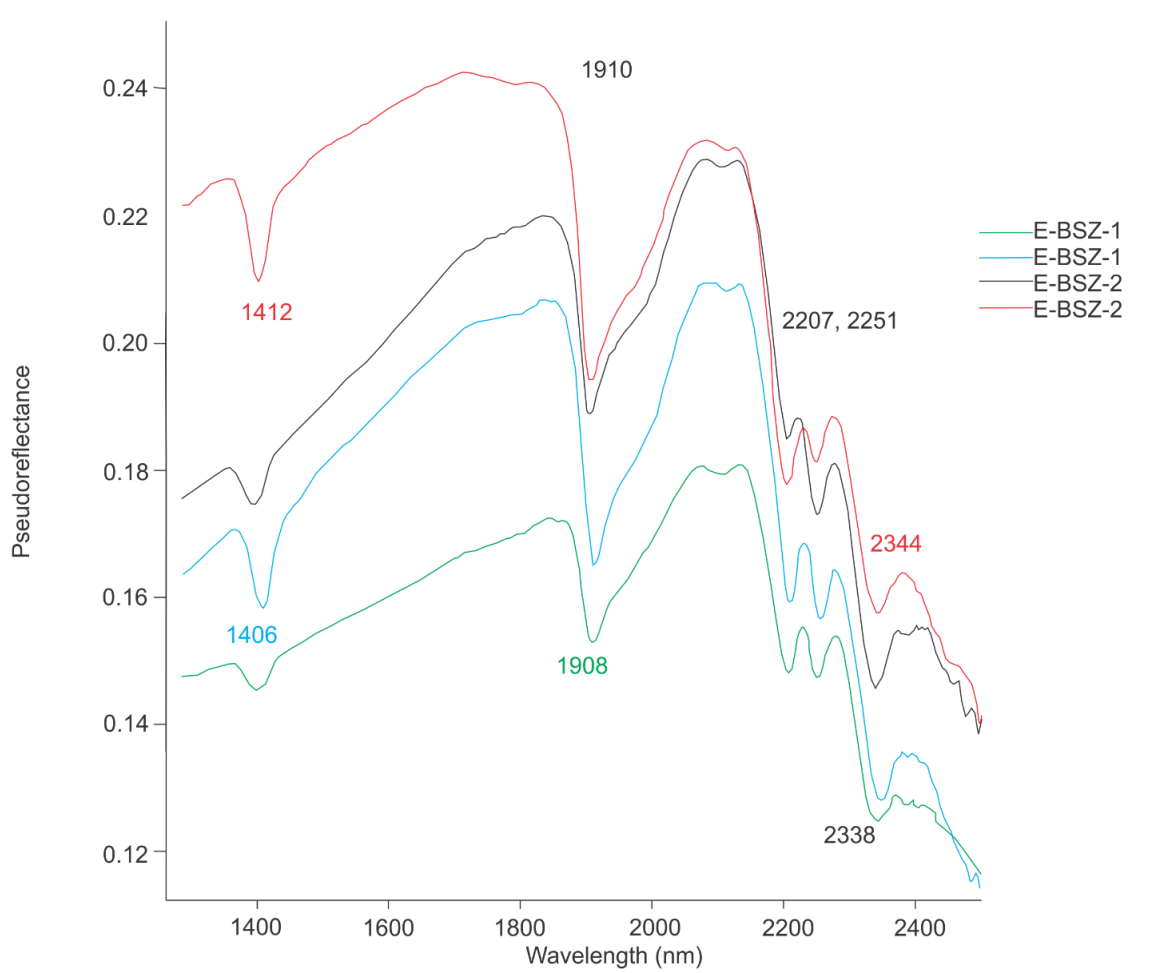

Figure A-5B. TerraSpec® spot analysis of early BSZ (samples E-BSZ-1 and E-BSZ-2) with two analyses per block due to differing reflectance and signatures past 2400 nm. Prominent absorption bands were plotted and colour-coded to the corresponding signature. All analyses show a doublet of absorption bands near 2205 nm and 2251 nm. Wavelength measured in nanometers (nm). Pseudoreflectance measured out of 1.

Appendix 5C: Late style 1 mineralization, Blue Sky Zone

The late BSZ has similar clay mineral compositions as the low-grade porphyry with a primary illite signature and lesser amounts of possible biotite (phlogopite) observed at the 2249 nm absorption band in sample L-BSZ-3 (Fig. A-5C). These mineral identifications are consistent with those report by on-site geologists (Northern Freegold Resources Ltd., 2015, 2017). A water spectral feature is again observed near 1916 nm absorption band, which suggests the presence of smectite in the clay assemblage, or that the illite-biotite clays are extremely hydrous. Low pseudoreflectance may be a result of poor placement the TerraSpec probe on a rounded surface.

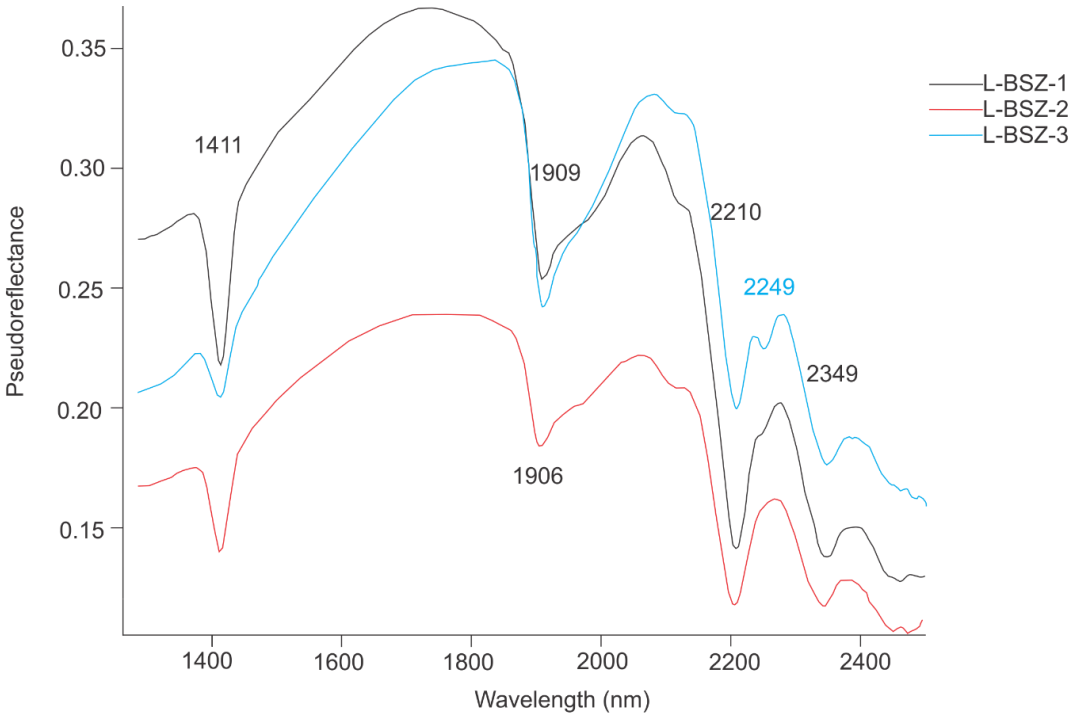

Figure A-5C. TerraSpec® spot analysis of late BSZ (samples L-BSZ-1, L-BSZ-2, and L-BSZ-3). Prominent absorption bands 1411 nm, ~1910 nm, 2210 nm, and 2349 nm are labeled in the same colour of corresponding analysis, with an additional absorption band at 2249 nm recorded for sample L-BSZ-3. Wavelength measured in nanometers (nm). Pseudoreflectance measured out of 1.

Appendix 5D: QFP dykes

The QFP dykes have clay compositions that are primarily illite and chlorite for QFP-1 and illite for QFP-2 (Fig. A-5D). These findings are consistent with reference material, in which chlorite was abundant in QFP-1 samples and plagioclase phenocrysts of both samples were altered. Slight variation in the trough of absorption bands differ 10 nm in width, as exemplified in the ~1410nm feature.

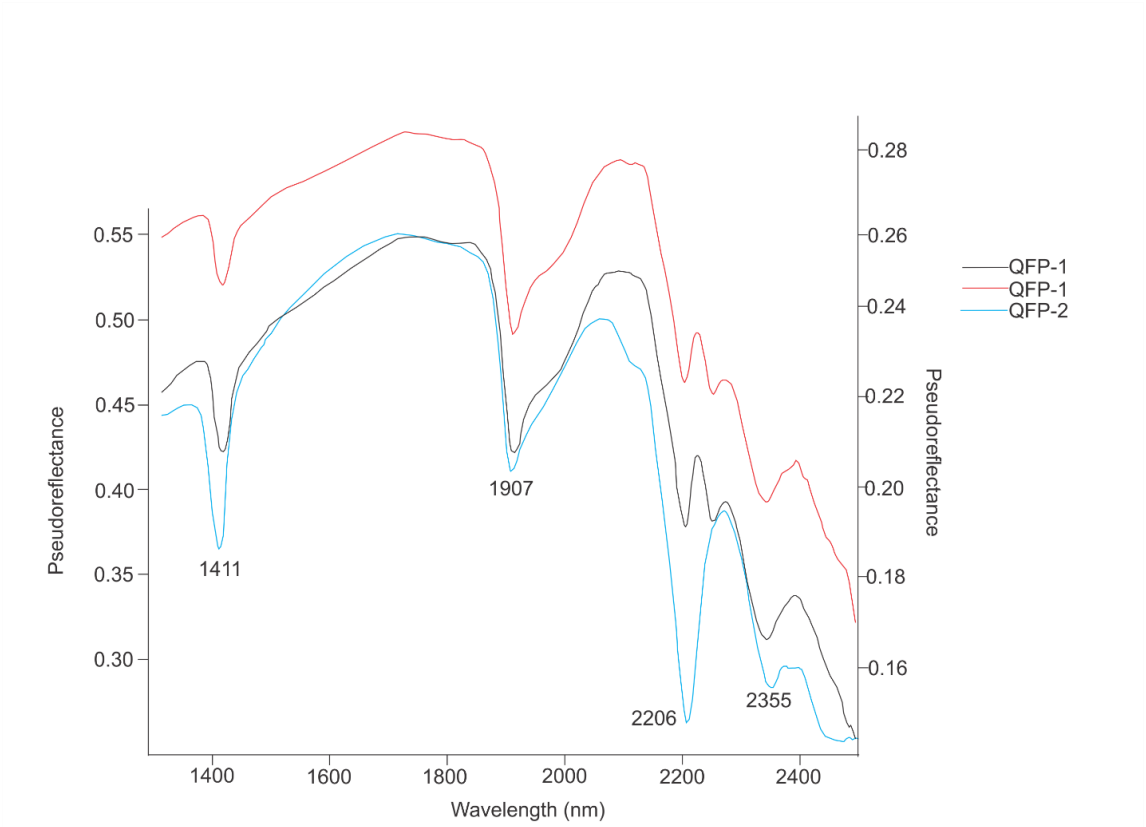

Figure A-5D. TerraSpec® spot analysis for QFP using sample QFP-1 (pseudoreflectance on right axis) and QFP-2 (pseudoreflectance on left axis). Samples show prominent absorption bands that differ slightly between 2206 and 2355 nm, where QFP-1 has additional dip at 2256nm. Sample QFP-1 also shows a minor absorption band doublet at 2206 nm and 2256 nm whereas QFP-2 does not show a doublet. Wavelength measured in nanometers (nm). Pseudoreflectance measured out of 1.

Appendix 5E: Style 2 mineralization, WAu breccia

The WAu breccia, represented by samples WAu-1 and WAu-2, is characterized by illite-muscovite signatures with minor kaolinite signatures at wavelengths 2300-2400 nm (Fig. A-5E). The absorption band ~1406 nm is shallow from 2 - 7 % pseudoreflectance which may be a mixture of clay compositions. This is consistent with pertrogrpahic work where coarse-grained muscovite occurs with dolomite-siderite in the groundmass (Figs. 15 E-I). In the Northern Freegold Resources Ltd. technical reports (2015, 2017) the WAu breccia is described to be altered by silicification and sericitization of kaolinite-illite, though no prominent signature for silica is present.

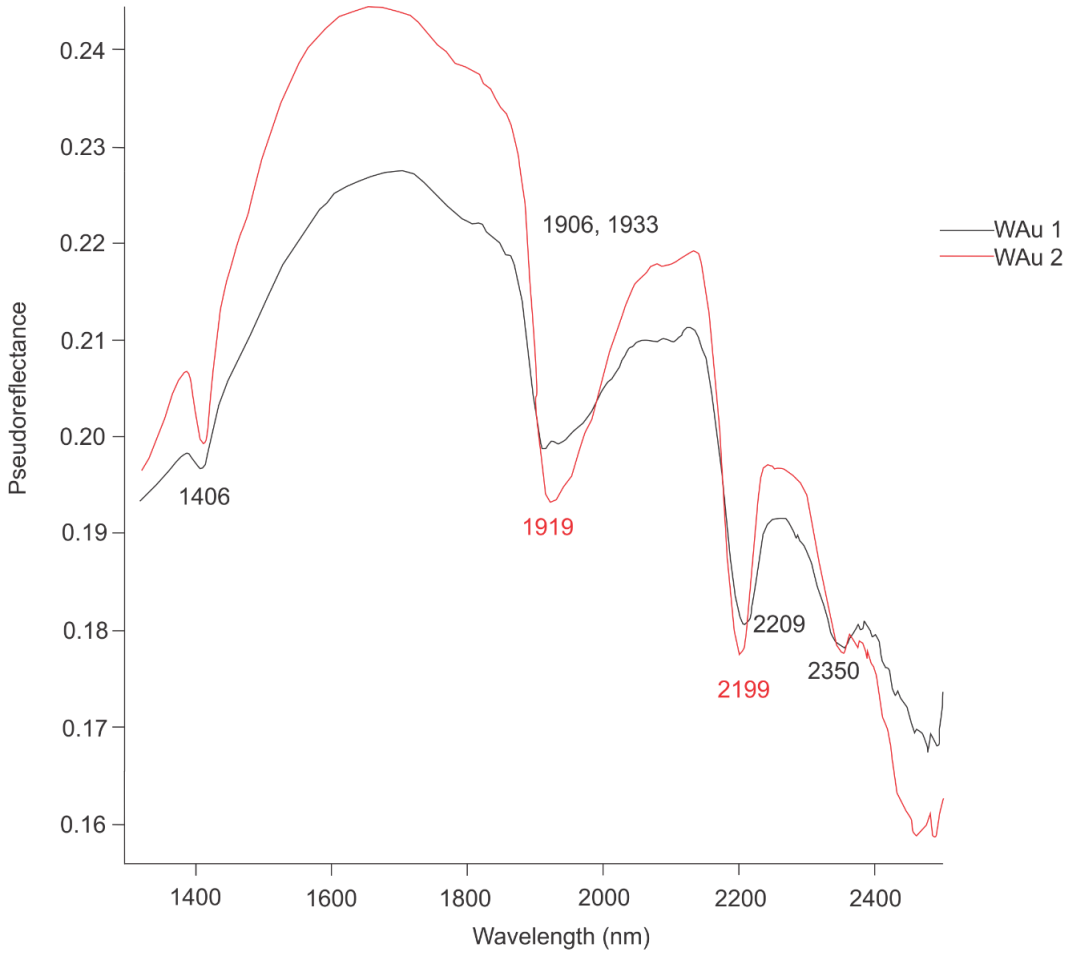

Figure A-5E. TerraSpec® spot analysis analysis of WAu breccia (samples WAu-1 and WAu-2). Prominent absorption bands are labeled in the same colour of corresponding analysis, with 1406 nm, ~1910 nm, ~2205 nm and 2350 nm acting as indicator absorption bands. Wavelength measured in nanometers (nm). Pseudoreflectance measured out of 1.

Appendix 5F: Style 3 mineralization, Revenue diatreme

The Revenue diatreme, represented by RD-1 and RD-2, has clay compositions that are primarily illite with secondary kaolinite or muscovite features occurring in readings RD-2 on the tail end (Fig. A-5F). These findings are consistent were in line with reference material (Northern Freegold Resources Ltd., 2015, 2017). No Mg-OH absorption band is present, which is consistent with petrographic work in this study. Slight variation in the trough of absorption bands differ 2 to 9 nm in width, as exemplified in the water feature near ~1910 nm and the Al-OH feature ~2210 nm. Again, the difference in pseudoreflectance is likely a result of poor placement of the TerraSpec probe on an uneven surface during analysis.

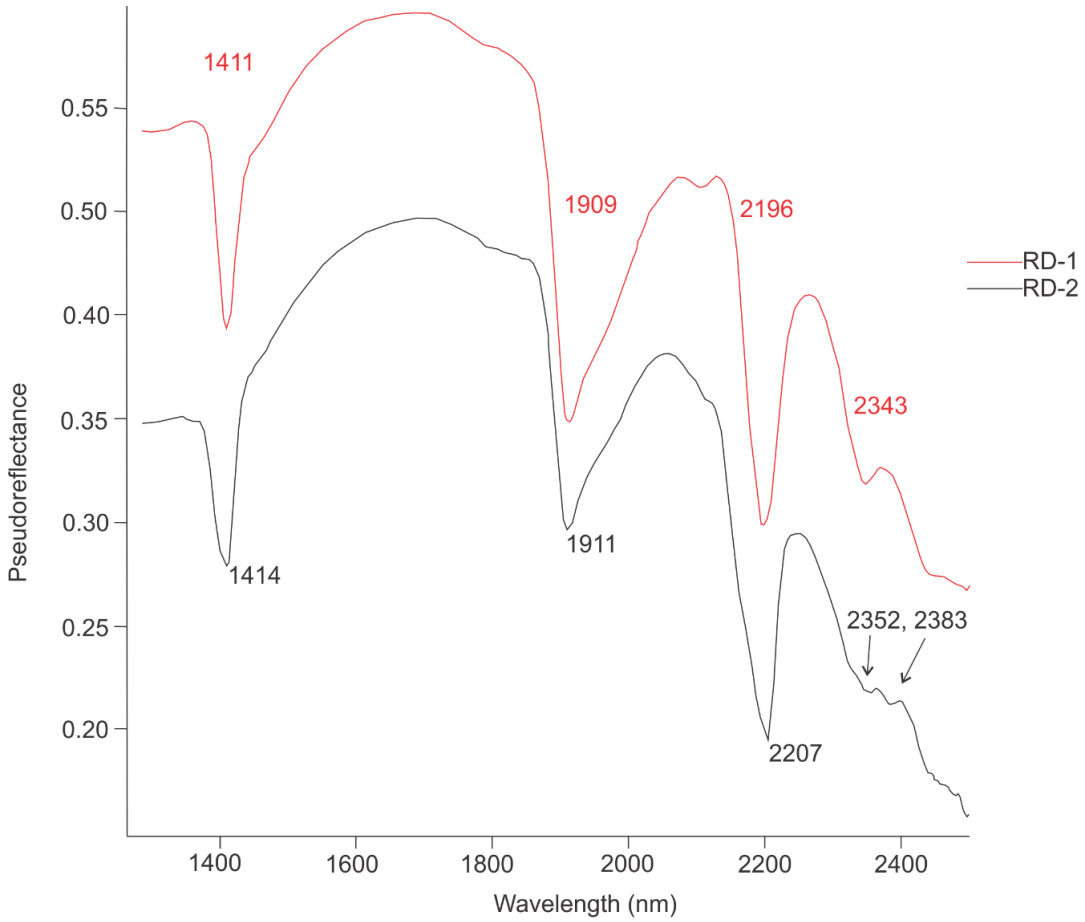

Figure A-5F. TerraSpec® spot analysis for Revenue diatreme (samples RD-1 and RD-2). Samples show prominent absorption bands that differ slightly with RD-2 absorption bands occurring 2 to 9 nm higher. Sample RD-2 also shows a minor absorption band doublet at 2352 nm and 2383 nm whereas RD-1 does not show a doublet. Wavelength measured in nanometers (nm). Pseudoreflectance measured out of 1.

Between all analysed areas the infrared spectra reflectance has prominent peaks that do not exactly match reference material for suspect minerals, has low pseudoreflectance values for the clay mineral composition, and had deep water features (Fig. A-5G). Many readings also show absorption bands at ~2205 nm, ~2250 nm, and ~2350 nm. All samples show an absorption band near ~1405 to ~1415 that corresponds to hydroxyl. Readings also show absorption bands at ~1910 nm denoting the presence of water, meaning that the all clay compositions include smectite or illite, or are extremely hydrous.

The loss of biotite, marked by the Mg-OH absorption band at ~2250 nm suggests that the early, early BSPZ, characterized by dense potassic alteration in the form of biotite stock-work, was overprinted by later illite-kaolinite-muscovite alteration. The characteristic absorption bands for biotite (pholophite) from reference material include 2245 nm, 2322 nm, 2378 nm, and 2439 nm, which all respond to the Mg-OH molecular group. No analysed absorption bands are exactly in line with the reference material, though a common absorption band of ~2250 nm.

Variances in psuedoreflectance may be a result of different placement on the probe from each analysis, with some samples having an irregular and curved surface, which may have decreased the amount of light reflected.

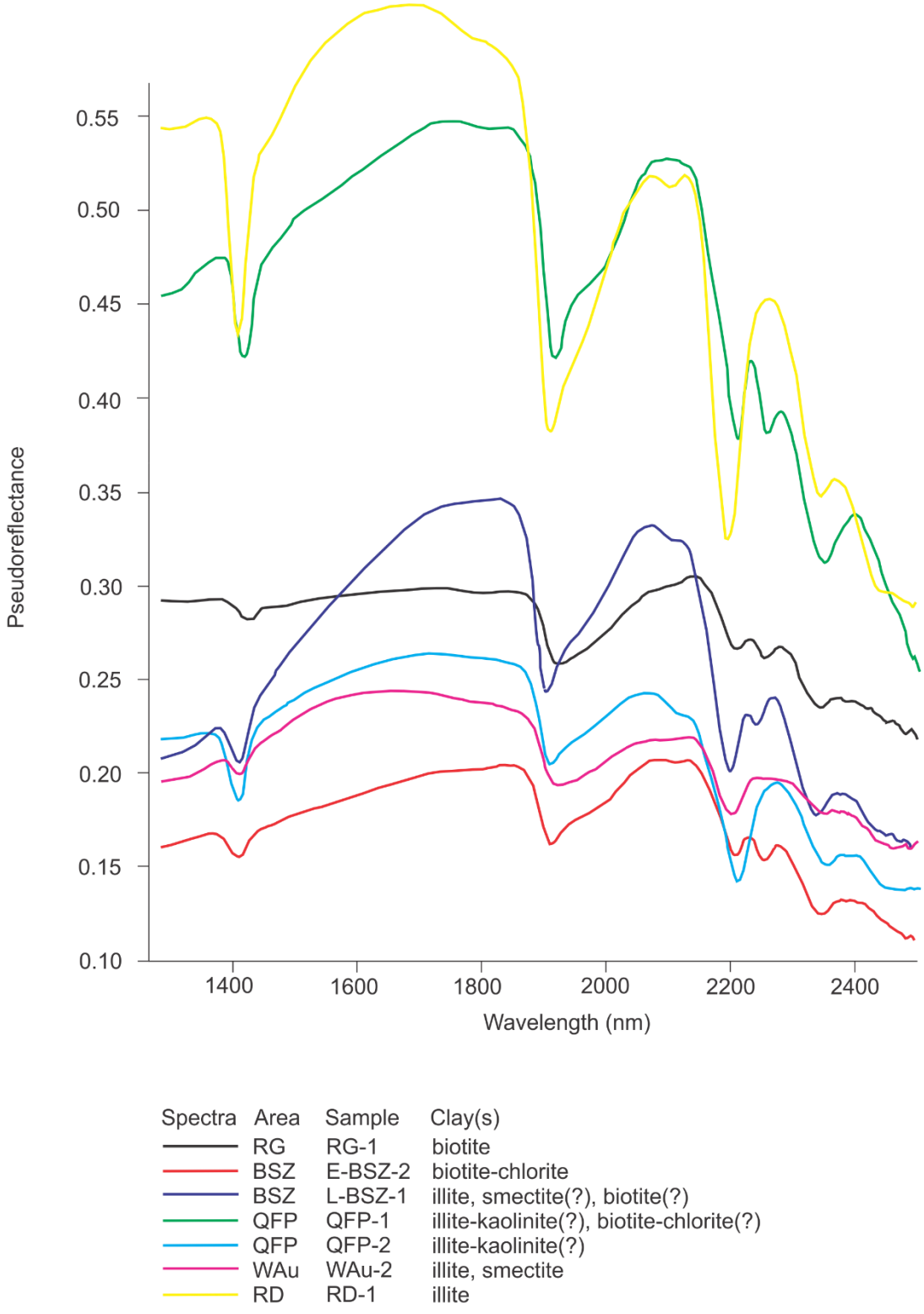

Figure A-5G. Summary Terraspec spectra using representative samples from Revenue granite, BSZ, QFP, WAu breccia, and Revenue diatreme.

Appendix 6: Mineral chemistry (EMPA, LA-ICP-MS, fluid inclusions)

Table A6-1. Chemical analysis of sphalerite in contact with pyrite and/or pyrrhotite in wt% for samples L-BSZ-1, L-BSZ-2, WAu-3, and RD-1. Obtained from EMPA. D.L. = detection limit. bdl = below detection limit.

Sample and point	Fe	Fe(D.L.)	Cu	Cu(D.L.)	As	As(D.L.)	Si	Si(D.L.)	Zn	Zn(D.L.)	Co	Co(D.L.)	Ni	Ni(D.L.)	S	S(D.L.)	Pb	Pb(D.L.)	Sn	Sn(D.L.)	Cd	Cd(D.L.)	In	In(D.L.)	Total
RD-1-Sp-1	4.209	0.037	3.859	0.052	bdl	0.035	bdl	0.011	56.846	0.040	bdl	0.014	bdl	0.020	32.446	0.018	bdl	0.060	bdl	0.029	0.408	0.065	0.07	0.038	97.858
RD-1-Sp-2	4.297	0.036	3.546	0.052	bdl	0.035	bdl	0.011	57.85	0.040	bdl	0.015	bdl	0.020	32.81	0.017	bdl	0.060	bdl	0.030	0.454	0.065	0.069	0.038	99.035
RD-1-Sp-3	4.386	0.036	4.051	0.050	bdl	0.034	bdl	0.011	56.95	0.040	bdl	0.015	bdl	0.020	32.808	0.018	bdl	0.060	bdl	0.029	0.437	0.065	0.088	0.038	98.728
RD-1-Sp-4	4.355	0.034	4.511	0.051	bdl	0.034	bdl	0.011	55.978	0.040	bdl	0.014	bdl	0.020	32.696	0.018	bdl	0.060	bdl	0.030	0.417	0.065	0.08	0.038	98.059
RD-1-Sp-5	5.695	0.035	2.666	0.050	bdl	0.036	bdl	0.011	56.994	0.040	bdl	0.014	bdl	0.020	32.392	0.017	bdl	0.060	bdl	0.029	0.418	0.064	0.08	0.038	98.257
RD-1-Sp-6	7.162	0.035	1.622	0.051	bdl	0.035	bdl	0.011	55.875	0.040	bdl	0.014	bdl	0.020	32.531	0.017	bdl	0.059	bdl	0.029	0.583	0.064	0.071	0.037	97.858
RD-1-Sp-7	7.807	0.037	0.733	0.050	bdl	0.035	bdl	0.011	56.346	0.039	bdl	0.014	bdl	0.020	32.906	0.018	bdl	0.059	bdl	0.030	0.637	0.065	0.075	0.038	98.505
RD-1-Sp-8	7.953	0.034	0.09	0.050	bdl	0.035	bdl	0.011	56.89	0.039	bdl	0.014	bdl	0.020	32.492	0.018	bdl	0.060	bdl	0.029	0.669	0.064	0.079	0.037	98.194
RD-1-Sp-9	5.354	0.037	3.559	0.051	bdl	0.035	bdl	0.011	57.138	0.040	bdl	0.014	bdl	0.020	32.594	0.018	bdl	0.060	bdl	0.029	0.096	0.064	0.09	0.037	98.842
L-BSZ-1-Sp-1	11.614	0.036	1.681	0.052	bdl	0.035	bdl	0.011	51.27	0.039	0.045	0.014	bdl	0.020	32.75	0.020	bdl	0.061	0.512	0.030	0.929	0.065	0.115	0.041	98.926
L-BSZ-1-Sp-2	10.918	0.037	3.862	0.050	bdl	0.034	bdl	0.011	48.755	0.040	0.04	0.014	bdl	0.020	32.462	0.021	bdl	0.061	1.432	0.031	0.887	0.066	0.178	0.043	98.54
L-BSZ-1-Sp-3	11.337	0.038	1.582	0.051	bdl	0.034	bdl	0.011	51.498	0.039	0.038	0.014	bdl	0.020	32.53	0.021	bdl	0.061	0.17	0.030	0.942	0.065	0.249	0.039	98.349
L-BSZ-2-Sp-1	5.335	0.000	3.938	0.000	bdl	0.004	bdl	0.000	56.157	0.000	0.023	0.005	bdl	0.000	33.034	0.000	0.021	0.000	bdl	0.000	1.084	0.010	0.07	0.000	99.769
L-BSZ-2-Sp-2	6.314	0.034	5.266	0.052	bdl	0.035	bdl	0.011	53.122	0.040	0.017	0.014	bdl	0.021	32.202	0.020	bdl	0.061	bdl	0.030	0.927	0.065	0.061	0.039	97.916
L-BSZ-2-Sp-3	6.408	0.034	4.642	0.052	bdl	0.034	bdl	0.011	53.197	0.040	bdl	0.014	bdl	0.020	31.82	0.021	bdl	0.059	0.127	0.030	0.653	0.066	0.058	0.039	96.936
L-BSZ-2-Sp-4	6.671	0.035	3.849	0.052	bdl	0.035	bdl	0.011	53.564	0.040	bdl	0.015	bdl	0.021	32.363	0.021	bdl	0.059	0.978	0.030	1.12	0.066	0.065	0.042	98.678
WAu-3-Sp-1	10.963	0.035	0.257	0.052	bdl	0.035	bdl	0.011	53.771	0.039	0.047	0.014	bdl	0.020	32.477	0.020	bdl	0.060	bdl	0.031	0.695	0.065	0.432	0.037	98.649
WAu-3-Sp-2	10.749	0.035	0.272	0.011	bdl	0.039	bdl	0.014	53.967	0.020	0.055	0.021	bdl	0.061	32.339	0.031	bdl	0.065	bdl	0.038	0.767	0.000	0.383	0.000	98.536
WAu-3-Sp-3	10.63	0.035	0.138	0.052	bdl	0.034	bdl	0.011	53.979	0.039	0.062	0.014	bdl	0.020	32.801	0.021	bdl	0.061	bdl	0.030	0.673	0.065	0.259	0.038	98.548
WAu-3-Sp-4	11.111	0.035	7.297	0.012	bdl	0.040	bdl	0.014	42.563	0.020	0.055	0.021	bdl	0.060	31.678	0.033	bdl	0.067	5.602	0.054	0.505	0.000	0.061	0.000	98.904
WAu-3-Sp-5	10.832	0.035	0.137	0.051	bdl	0.035	bdl	0.011	54.137	0.040	0.059	0.014	bdl	0.020	32.398	0.021	bdl	0.060	bdl	0.030	0.734	0.064	0.24	0.038	98.539
WAu-3-Sp-6	10.091	0.035	0.23	0.011	bdl	0.039	bdl	0.014	54.599	0.020	0.042	0.021	bdl	0.060	32.829	0.030	bdl	0.064	bdl	0.038	0.919	0.000	0.129	0.000	98.858
WAu-3-Sp-7	13.269	0.034	0.137	0.050	bdl	0.035	bdl	0.011	51.858	0.039	0.055	0.014	bdl	0.020	31.967	0.020	bdl	0.059	bdl	0.030	0.789	0.064	0.148	0.038	98.229
WAu-3-Sp-8	10.39	0.033	0.636	0.052	bdl	0.034	bdl	0.011	53.165	0.039	0.061	0.014	bdl	0.020	32.397	0.021	bdl	0.059	bdl	0.031	0.759	0.065	0.479	0.038	97.899
WAu-3-Sp-9	10.513	0.000	0.938	0.000	bdl	0.004	bdl	0.000	52.846	0.000	0.091	0.005	bdl	0.000	32.833	0.000	bdl	0.000	bdl	0.000	0.696	0.010	0.521	0.003	98.489
WAu-3-Sp-10	6.623	0.034	6.104	0.050	bdl	0.035	bdl	0.011	52.417	0.040	0.018	0.015	bdl	0.020	32.596	0.021	bdl	0.060	bdl	0.029	0.628	0.064	0.114	0.038	98.509
WAu-3-Sp-11	6.19	0.035	5.247	0.053	bdl	0.036	bdl	0.011	53.528	0.040	0.026	0.014	bdl	0.020	32.482	0.020	bdl	0.059	bdl	0.030	0.642	0.065	0.107	0.038	98.226

Table A6-2. Sphalerite thermometry data using mol% Fe from EMPA to determine mol% FeS. Values in yellow indicate samples with < 2 wt% Cu and values in green are those plotted for sphalerite thermometry in this study.

Sample and point	Fe	FeS
RD-1-Sp-1	3.726	7.453
RD-1-Sp-2	3.761	7.521
RD-1-Sp-3	3.846	7.693
RD-1-Sp-4	3.841	7.681
RD-1-Sp-5	5.021	10.042
RD-1-Sp-6	6.319	12.638
RD-1-Sp-7	6.832	13.664
RD-1-Sp-8	6.999	13.997
RD-1-Sp-9	4.689	9.378
L-BSZ-1-Sp-1	10.120	20.239
L-BSZ-1-Sp-2	9.597	19.193
L-BSZ-1-Sp-3	9.936	19.871
L-BSZ-2-Sp-1	5.347	10.694
L-BSZ-2-Sp-2	5.590	11.181
L-BSZ-2-Sp-3	5.730	11.460
L-BSZ-2-Sp-4	5.887	11.774
WAu-3-Sp-1	9.590	19.180
WAu-3-Sp-2	9.424	18.848
WAu-3-Sp-3	9.281	18.561
WAu-3-Sp-4	9.912	19.823
WAu-3-Sp-5	9.487	18.973
WAu-3-Sp-6	8.796	17.593
WAu-3-Sp-7	11.649	23.297
WAu-3-Sp-8	9.155	18.311
WAu-3-Sp-9	10.674	21.348
WAu-3-Sp-10	5.812	11.624
WAu-3-Sp-11	5.453	10.905

Table A6-3. Normalized trace arsenopyrite composition in mol %, obtained for sample QFP-2 via EMPA, University of Toronto.

Point	Fe	Fe(D.L.)	Cu	Cu(D.L.)	As	As(D.L.)	Co	Co(D.L.)	Ni	Ni(D.L.)	S	S(D.L.)	Pb	Pb(D.L.)	Total
Typical arsenopyrite															
QFP-2-A1-apy-1	31.64	0.12	bdl	0.19	29.24	0.08	0.32	0.06	0.15	0.07	38.64	0.07	bdl	0.04	100
QFP-2-A2-apy-1	31.98	0.12	bdl	0.16	32.38	0.08	0.25	0.06	bdl	0.08	35.39	0.07	bdl	0.03	100
QFP-2-A2-apy-2	32.47	0.11	0.25	0.18	32.84	0.08	0.15	0.07	bdl	0.08	34.29	0.08	bdl	0.03	100
QFP-2-A2-apy-3	32.35	0.11	bdl	0.21	31.99	0.08	0.09	0.06	bdl	0.07	35.58	0.07	bdl	0.03	100
QFP-2-A2-apy-4	33.60	0.13	bdl	0.18	31.93	0.08	0.19	0.05	bdl	0.07	34.28	0.07	bdl	0.03	100
QFP-2-A2-apy-5	33.09	0.15	bdl	0.18	30.86	0.08	0.14	0.05	bdl	0.08	35.91	0.07	bdl	0.04	100
QFP-2-A2-apy-7	31.44	0.11	bdl	0.15	29.30	0.08	0.24	0.05	bdl	0.07	39.02	0.07	bdl	0.04	100
QFP-2-A2-apy-8	33.93	0.12	bdl	0.19	32.99	0.08	0.07	0.05	bdl	0.07	33.01	0.07	bdl	0.03	100
QFP-2-A2-apy-10	33.23	0.14	bdl	0.18	30.19	0.08	0.12	0.05	bdl	0.07	36.47	0.07	bdl	0.03	100
QFP-2-A2-apy-12	32.00	0.12	bdl	0.19	32.12	0.08	0.12	0.05	bdl	0.07	35.76	0.07	bdl	0.03	100
QFP-2-A2-apy-13	33.42	0.14	bdl	0.18	31.22	0.08	0.06	0.05	bdl	0.07	35.30	0.07	bdl	0.03	100
QFP-2-A3-apy-1	31.82	0.14	bdl	0.18	35.48	0.08	1.47	0.05	0.84	0.08	30.39	0.07	bdl	0.03	100
Co-Ni-rich arsenopyrite															
QFP-2-A3-apy-Ni-1	20.34	0.13	bdl	0.20	36.26	0.08	8.77	0.07	4.09	0.08	30.49	0.08	0.04	0.03	100
QFP-2-A3-apy-Ni-2	11.67	0.16	bdl	0.21	38.83	0.08	12.46	0.07	9.56	0.08	27.47	0.07	bdl	0.04	100
QFP-2-A3-apy-Ni-3	12.84	0.12	0.33	0.20	23.25	0.07	15.81	0.06	9.07	0.07	38.59	0.07	0.11	0.03	100
QFP-2-A3-apy-Ni-4	17.89	0.15	0.28	0.22	41.01	0.09	8.33	0.07	7.95	0.09	24.54	0.07	bdl	0.04	100
QFP-2-A3-apy-Ni-5	21.80	0.14	0.88	0.21	29.48	0.08	8.69	0.05	5.21	0.08	33.91	0.07	0.03	0.03	100

Table A6-4. Glaucodot compositions in mole % obtained from EPMA at Dalhousie University.

Sample	Fe	S	As	Co	Ni	Total
WAu-2	2.99	29.19	22.31	45.53	bdl	100.00
WAu-2	8.42	35.91	18.21	37.25	0.22	100.00
WAu-2	4.01	27.12	23.12	45.62	0.14	100.00
WAu-2	5.77	28.27	22.93	42.54	0.50	100.00
WAu-3	6.12	28.05	23.94	41.34	0.53	100.00
WAu-3	6.09	28.68	23.70	40.99	0.53	100.00
WAu-3	5.16	28.10	23.24	42.96	0.49	100.00
WAu-3	7.41	28.31	24.63	38.99	0.66	100.00
WAu-3	6.58	28.40	23.43	40.91	0.66	100.00
WAu-3	7.30	28.45	23.83	39.81	0.62	100.00
WAu-3	7.43	28.26	23.87	39.82	0.59	100.00
WAu-3	7.44	27.87	24.71	39.27	0.70	100.00
WAu-3	6.57	27.93	24.07	40.87	0.56	100.00
WAu-3	6.44	28.25	23.71	41.10	0.44	100.00
WAu-3	6.13	28.25	23.68	41.39	0.44	100.00
WAu-3	6.64	27.87	24.01	40.80	0.60	100.00
WAu-3	6.86	27.80	24.54	40.18	0.61	100.00
WAu-3	6.54	27.49	24.29	41.08	0.62	100.00

Table A6-5. Endmember composition for sulfarsenide ternary using glaucodot compositions obtained from EPMA at Dalhousie University. Values bdl were treated as "0".

Sample	Fe	Co	Ni
WAu-2	6.16	93.84	0.00
WAu-2	18.34	81.18	0.00
WAu-2	8.06	91.65	0.00
WAu-2	11.83	87.16	0.01
WAu-3	12.76	86.14	0.01
WAu-3	12.79	86.09	0.01
WAu-3	10.62	88.38	0.01
WAu-3	15.74	82.86	0.01
WAu-3	13.66	84.97	0.01
WAu-3	15.29	83.41	0.01
WAu-3	15.53	83.24	0.01
WAu-3	15.70	82.83	0.01
WAu-3	13.68	85.14	0.01
WAu-3	13.43	85.65	0.01
WAu-3	12.78	86.31	0.01
WAu-3	13.81	84.94	0.01
WAu-3	14.40	84.32	0.01
WAu-3	13.56	85.16	0.01

Table A6-6. Fluid inclusion temperature proxies for sample WAu-3 using salt volume, estimated salinity using halite area % vs salinity calibration, and temperature calculations (after Bodnar and Vityk, 1995).

Sample WAu-3	Halite Area %	Salinity (eq NaCl wt%)	Ts	Minimum Salinity	Ts min	Maximum Salinity	Ts max
Assemblage 1							
FI 1	19.10	44.11	368	41.34	338	46.89	395
FI 2	5.36	24.16	NA	21.12	NA	27.19	69
FI 3	9.97	32.42	210	29.53	147	35.30	259
FI 4	8.13	29.43	144	26.50	29	32.36	209
FI 5	6.57	26.61	37	23.62	NA	29.58	148
FI 6	6.46	26.40	20	23.41	NA	29.38	143
Assemblage 3							
FI 1	9.29	31.36	189	28.46	116	34.26	243
FI 2	12.91	36.64	279	33.81	235	39.48	326
FI 3	17.41	42.22	348	39.43	316	45.01	377
FI 4	11.82	35.14	257	32.29	208	38.00	298
FI 5	13.18	37.00	284	34.17	242	39.83	321
FI 6	21.69	46.86	394	44.10	368	49.61	419
FI 7	19.71	44.79	375	42.02	346	47.55	401
FI 8	8.15	29.46	145	26.53	31	32.39	210
FI 9	15.19	39.58	318	36.77	280	42.39	350
FI 10	13.91	37.97	297	35.14	257	40.79	332
FI 11	11.03	34.01	239	31.14	185	36.87	282
FI 12	12.68	36.33	275	33.49	230	39.17	312
Assemblage 5							
FI 1	6.93	27.29	73	24.31	NA	30.25	164
FI 2	8.78	30.53	171	27.62	87	33.44	229
Assemblage 6.1							
FI 1	12.06	35.48	262	32.63	214	38.33	302
FI 2	11.51	34.71	250	31.85	200	37.56	292
FI 3	7.37	28.10	104	25.14	NA	31.04	183
FI 4	11.60	34.84	252	31.98	202	37.69	293
Assemblage 6.3							
FI 1	8.41	29.90	156	26.98	58	32.82	218
FI 2	13.83	37.85	296	35.03	255	40.68	331
FI 3	8.13	29.43	144	26.50	29	32.36	210
FI 4	15.49	39.95	322	37.14	286	42.75	354
FI 5	4.57	22.41	NA	19.32	NA	25.48	NA
Average	11.42	33.96	238	31.08	183	36.84	282
Stdev.s***	4.40	6.26	102	6.34	104	6.19	87
Max	21.69	46.86	394	44.10	368	49.61	419
Min	4.57	22.41	NA	19.32	NA	25.48	NA

***Standard deviations and associated temperature are calculated through Excel and are not representative of Bodnar and Vityk (1995) temperatures.

Table A6-7. Fluid inclusion temperature proxies for sample L-BSZ-1 using salt volume, estimated salinity using halite area % vs salinity calibration, and temperature calculations (after Bodnar and Vityk, 1995).

Sample L-BSZ-1	Halite Area %	Salinity (eq NaCl wt%)	Ts	Minimum Salinity	Ts min	Maximum Salinity	Ts max
Assemblage 1							
FI 1	7.77	28.81	127	25.87	NA	31.75	176
FI 2	19.70	44.77	374	42.00	346	47.54	401
FI 3	21.45	46.62	392	43.86	365	49.37	417
FI 4	17.57	42.41	350	39.62	318	45.19	378
FI 5	18.85	43.84	365	41.07	335	46.62	392
Assemblage 2							
FI 1	21.98	47.15	397	44.40	371	49.91	422
FI 2	5.07	23.54	NA	20.48	NA	26.58	35
FI 3	33.78	57.81	485	55.10	464	60.51	505
FI 4	14.50	38.72	307	35.90	269	41.53	340
FI 5	6.17	25.83	NA	22.83	NA	28.82	94
FI 6	10.52	33.26	226	30.39	168	36.13	272
FI 7	22.82	48.01	405	45.26	379	50.75	429
Assemblage3							
FI 1	23.57	48.74	412	45.99	386	51.48	438
FI 2	15.95	40.51	323	37.71	294	43.31	360
Assemblage 4							
FI 1	21.55	46.72	393	43.96	366	49.47	418
FI 2	15.54	40.02	323	37.21	287	42.82	354
Assemblage 5							
FI 1	20.68	45.81	385	43.05	357	48.57	410
FI 2	9.80	32.16	205	29.27	140	35.04	356
Average	17.07	40.82	333	38.00	298	43.63	363
Stdev.s***	7.26	8.97	90	9.07	83	8.88	124
Max	33.78	57.81	485	55.10	464	60.51	505
Min	5.07	23.54	NA	20.48	NA	26.58	35

***Standard deviations and associated temperature are calculated through Excel and are not representative of Bodnar and Vityk (1995) temperatures.

Appendix 7: Additional mineral chemistry (SEM)

Appendix 7A: Metallic and ore minerals

Major metallic and opaque minerals include chalcopyrite, pyrrhotite and pyrite with minor minerals of sphalerite, galena, molybdenite, arsenopyrite, glaucodot, and ferberite-scheelite. Trace minerals include electrum and stannite. Average mineral composition averages are shown in Table 1.

Chalcopyrite composition from the BSZ and the WAu breccia were collected using the EMPA and chalcopyrite composition from the least altered host granite, the QFP dyke, and the Revenue diatreme were collected using the SEM-EDS with a total average composition in Table 1. Chalcopyrite in the early BSZ (sample E-BSZ-2; n = 3) has S (34.41±0.20 wt%), Fe (29.73±0.15 wt%), and Cu (33.77±0.11 wt%). Chalcopyrite in the late BSZ stockwork (sample L-BSZ-2; n = 3) has S (33.92±0.11 wt%), Fe (29.52±0.16 wt%), and Cu (33.93±0.36 wt%). Chalcopyrite in the WAu breccia (sample WAu-3; n = 3) has S (34.08±0.15 wt%), Fe (30.49±0.17 wt%), and Cu (34.65±0.05 wt%). Chalcopyrite in the Revenue granite (sample RG-1; n = 13) has S (39.18±2.18 wt%), Fe (28.96±0.75 wt%), and Cu (31.71±1.40 wt%). Chalcopyrite in the QFP (samples QFP-1 and QFP-2; total n = 6), has S (40.07±1.20 wt%), Fe (28.55±0.37 wt%), and Cu (31.10±1.12 wt%). Microprobe analyses from QFP-1 (n = 1) shows chalcopyrite having S (35.10 wt%), Fe (29.69 wt%), and Cu (34.62 wt%). Chalcopyrite in the Revenue diatreme (samples RD-1 and RD-2; total n = 14) has S (38.56±1.08 wt%), Fe (29.12±0.38 wt%)e, and Cu (32.20±0.91 wt%). In sample MW14, the chalcopyrite occurs with sphalerite, in which there is sphalerite dissolution in chalcopyrite and chalcopyrite disease within sphalerite. For this reason,

chalcopyrite in RD-1 region may have Zn (< 2.27 wt%), which results in lower Fe and Cu wt%.

Pyrite composition from the Revenue granite, the BSZ, the WAu breccia, and the Revenue diatreme were collected using the EMPA and pyrite composition from the QFP dykes were collected using the SEM-EDS with a total average composition in Table 1. Pyrite in the Revenue granite (Sample RG-1; n = 4) has S (51.61±0.42 wt%) and Fe (47.13±0.45 wt%). Pyrite from the early BSZ (sample E-BSZ-2; n = 3) has S (53.36±0.11 wt%) and Fe (46.80±0.13 wt%). Pyrite from the late BSZ (sample L-BSZ-2; n=10) has S (52.17±1.12 wt%) and Fe (47.52±0.54 wt%). Pyrite from the WAu breccia (sample WAu-2 and WAu-3; total n = 12) has S (51.92±1.36 wt%) and Fe (47.92±0.38 wt%). Pyrite from the Revenue diatreme (sample RD-1; n = 10) has S (53.04±0.32 wt%) and Fe (46.38±0.25 wt%). Pyrite from the QFP (samples QFP-1 and QFP-2; total n = 23) has S (53.40±1.33 wt%) and Fe (45.72±1.24 wt%).

Pyrrhotite composition from the Revenue granite, BSZ, and the WAu breccia were collected using the EMPA and pyrrhotite composition from the QFP dykes were collected using the SEM-EDS with a total average composition in Table X. Pyrrhotite in the Revenue granite (Sample RG-1; n = 4) has S (39.35±0.24 wt%) and Fe (60.44±0.26 wt%). Pyrrhotite in the early BSZ (Sample E-BSZ-2; n = 3) has S (39.35±0.21 wt%) and Fe (60.51±0.17 wt%). Pyrrhotite in the late BSZ pyrrhotite (sample L-BSZ-2; n = 3) has S (38.88±0.11 wt%) and Fe (59.22±0.03 wt%). WAu Breccia pyrrhotite (n=10) reports 39.01±0.12 wt% S and 59.70±0.36 wt% Fe. Pyrrhotite in the QFP (sample QFP-1; n = 2) has S (39.35±0.24 wt%) and Fe (59.51±0.15 wt%).

Sphalerite composition from the BSZ, the WAu breccia, and the Revenue diatreme were collected using the EMPA with a total average composition in Table 1. Sphalerite

from the late BSZ (sample L-BSZ-2; n = 5) has near-stoichiometric S (32.46±0.20 wt%), with variable Zn (48.76-51.64 wt%), Fe (6.31-11.61 wt%), and Cu (1.58-5.27 wt%). In this area, sphalerite may have trace amounts of Sn (1.61-2.96 wt%). Sphalerite of the WAu breccia (sample WAu-3; n = 10) contains 32.48±0.26 wt% S and 53.49±0.87 wt% Zn, with variable Fe (6.19-13.27 wt%) and Cu (0.14-6.10 wt%). Sphalerite of the Revenue diatreme (RD-1; n = 9) has S (32.63±0.18 wt%), Zn (56.76±0.61 wt), with variable Fe (4.21-7.95 wt%), and Cu (0.09-4.51 wt %).

Galena composition from the BSZ, QFP, WAu breccia, and Revenue diatreme were collected using the SEM-EDS with total average composition in Table 1. Galena in the early BSZ (sample E-BSZ-2; n = 1) has Pb (86.64 wt%), S (11.98 wt%), and minor Fe (1.38 wt%). Galena in the late BSZ (sample L-BSZ-2; n = 13) has Pb (87.52±0.29 wt%) and S (12.48±0.29 wt%). Galena in the QFP (QFP-X; n = 2) has Pb (85.10±0.57 wt%) and S (14.90±0.57wt%). Galena in the WAu breccia (WAu-4; n = 8) has Pb (84.49±0.14 wt%) and S (15.51±0.14 wt%). In a localized zone of the WAu breccia, galena (sample WAu-4; n = 23) has variable Pb (32.17-51.52 wt%), Bi (22.74-50.70 wt%), S (17.40±0.30 wt%), and Sb (1.78-8.34 wt%). In these locations, areas of galena surround anhedral grains (n = 6) of variable Bi (58.09-100 wt%) and Te (< 41.92 wt%). Galena in the Revenue diatreme (RD-2; n = 2) has Pb (84.90±0.54 wt%) and S (14.84±0.14 wt%).

Molybdenite was analysed from the late BSZ, the QFP, and the WAu breccia using the SEM-EDS, with a total average composition in Table 1. Molybdenite in the BSZ (sample L-BSZ-2; n=2) has Mo (58.79±1.28 wt%) and S (40.92±1.23 wt%). Molybdenite in the QFP (QFP-1; n = 3) has Mo (60.00±0.47 wt%) and S (39.77±0.56 wt%). Molybdenite in the WAu breccia (samples WAu-1, WAu-2, and WAu-3; total n = 28) has Mo (60.06±1.25 wt%) and S (38.87±1.16 wt%).

Glaucodot composition from the WAu breccia (samples WAu-2 and WAu-3) was collected form the EMPA with total average compositions in Table 1. Glaucodot (n=18) has As (33.74-43.05 wt%), Co (25.42-31.74 wt%), S (20.74-28.48 wt%), Fe (4.12-11.63 wt%), and minor Ni (< 0.96 wt%).

Arsenopyrite composition from the QFP dykes were collected using the EMPA and arsenopyrite composition from the late BSZ and Revenue diatreme were collected using the SEM-EDS with a total average composition in Table 1. Arsenopyrite from the QFP (sample QFP-2; n = 9) has As (44.10±1.84 wt%), S (20.86±1.71 wt%), and Fe (33.91±1.13 wt%). Arsenopyrite in the late BSZ (sample L-BSZ-2; n = 4) has As (43.88±0.68 wt%), S (23.42±0.67 wt%), and Fe (32.48±0.48 wt%). Arsenopyrite from the Revenue diatreme (sample RD-2; n = 1) has As (43.69 wt%), S (23.93 wt%), and Fe (32.38 wt%).

Tungstate composition from the WAu breccia (samples WAu-2 and WAu-4) were collected using the SEM-EDS. Scheelite (n = 14) has W (61.18±0.96 wt%), O (26.94±1.43 wt%), Ca (10.77±1.42 wt%), and Fe (< 5.14 wt%). Ferberite (n = 10) has W (58.60±0.62 wt%), O (26.43±1.53wt%), Fe (4.87±0.98wt%) and Mn (0.11±0.23 wt%).

Precious metals of electrum were found in the late BSZ and WAu breccia, respectively, using SEM-EDS. Electrum in the late style 1 mineralization (sample L-BSZ-2; n = 3) has Ag (68.11-70.81 wt%) and Au (31.89-29.19 wt%) which translates to 3.90-4.43 Ag : Au and in the WAu breccia (sample WAu-4; n = 2) has Au (92.63-94.85 wt%) and Ag (5.1-7.37 wt%) which translates to 6 Au : 10 Ag. Stannite composition from the late BSZ (sample L-BSZ-2; n = 1) was collected from SEM-EDS, shown in Table 1. Stannite has S (30.73-32.83 wt%), Sn (22.19-26.31 wt%), Cu (24.33-26.58 wt%), Fe (7.23-12.43 wt%), Zn (2.06-8.39 wt%) and O (< 4.78 wt%).

Table 1. Mineral compositions of metallic minerals obtained via SEM-EDS in wt%.

	Metallic and Ore Minerals																			
	cpp		py		po		sp				gn		gn-Bi				Bi±Te			
	n=10		n=46		n=23		n=24				n=27		n=14				n=6			
Element (Wt%)	Avg	1 σ	Avg	1 σ	Avg	1 σ	Avg	1 σ	Min	Max	Avg	1 σ	Avg	1 σ	Min	Max	Avg	1 σ	Min	Max
O	-	-	-	-	-	-	-	-	-	-	-	-	-	-	-	-	-	-	-	-
S	34.23	0.39	52.74	1.18	39.20	0.29	32.53	0.22	31.97	32.91	13.80	1.47	14.40	0.30	16.90	18.01	-	-	-	-
Ca	-	-	-	-	-	-	-	-	-	-	-	-	-	-	-	-	-	-	-	-
Mn	-	-	-	-	-	-	-	-	-	-	-	-	-	-	-	-	-	-	-	-
Fe	29.89	0.44	46.69	1.20	59.92	0.52	8.17	2.85	4.21	13.27	-	-	-	-	-	-	-	-	-	-
Co	-	-	-	-	-	-	-	-	-	-	-	-	-	-	-	-	-	-	-	-
Ni	-	-	-	-	-	-	-	-	-	-	-	-	-	-	-	-	-	-	-	-
Cu	34.17	0.45	-	-	-	-	2.35	2.01	0.09	6.10	-	-	-	-	-	-	-	-	-	-
Zn	-	-	-	-	-	-	54.37	2.33	48.76	57.85	-	-	-	-	-	-	-	-	-	-
As	-	-	-	-	-	-	-	-	-	-	-	-	-	-	-	-	-	-	-	-
Se	-	-	-	-	-	-	-	-	-	-	-	-	-	-	-	-	-	-	-	-
Mo	-	-	-	-	-	-	-	-	-	-	-	-	-	-	-	-	-	-	-	-
Ag	-	-	-	-	-	-	-	-	-	-	-	-	-	-	-	-	-	-	-	-
Au	-	-	-	-	-	-	-	-	-	-	-	-	-	-	-	-	-	-	-	-
Sb	-	-	-	-	-	-	-	-	-	-	-	-	-	-	-	-	-	-	-	-
Te	-	-	-	-	-	-	-	-	-	-	-	-	-	-	-	-	-	-	-	-
W	-	-	-	-	-	-	-	-	-	-	-	-	-	-	-	-	-	-	-	-
Au	-	-	-	-	-	-	-	-	-	-	-	-	-	-	-	-	-	-	-	-
Sb	-	-	-	-	-	-	-	-	-	-	-	-	5.79	1.86	1.78	8.34	-	-	-	-
Te	-	-	-	-	-	-	-	-	-	-	-	-	-	-	-	-	17.62	20.42	0.00	41.92
Bi	-	-	-	-	-	-	-	-	-	-	-	-	32.24	4.94	22.74	50.70	82.38	20.42	58.09	100.00
Pb	-	-	-	-	-	-	-	-	-	-	86.12	1.46	44.83	3.12	32.17	51.52	-	-	-	-
Total	98.29	0.93	100.00	0.88	99.38	0.64	98.42	0.35	97.86	99.04	100.00	0.00	100.00	0.00	100.00	100.00	100.00	0.00	100.00	100.00

Table 1 cont'd. Mineral compositions of metallic minerals obtained via SEM-EDS in wt%.

	Metallic and Ore Minerals													
	mol		glc		apy		sch		frb		electrum*		electrum**	
	n=33		n=18		n=14		n=14		n=10		n=3		n=2	
Element (Wt%)	Avg	1 σ	Avg	1 σ	Avg	1 σ	Avg	1 σ	Avg	1 σ	Avg	1σ	Avg	1 σ
O	-	-	-	-	-	-	26.94	1.43	26.43	1.53	-	-	-	-
S	39.07	1.23	21.78	1.75		1.92	-	-	-	-	-	-	-	-
Ca	-	-	-	-	-	-	10.77	1.42	-	-	-	-	-	-
Mn	-	-	-	-	-	-	-	-	0.11	0.23	-	-	-	-
Fe	-	-	8.38	1.67	33.39	1.16	1.95	1.72	14.87	0.98	-	-	-	-
Co	-	-	27.39	1.68	-	-	-	-	-	-	-	-	-	-
Ni	-	-	0.68	0.26	-	-	-	-	-	-	-	-	-	-
Cu	-	-	-	-	-	-	-	-	-	-	-	-	-	-
Zn	-	-	-	-	-	-	-	-	-	-	-	-	-	-
As	-	-	41.72	2.07	44.01	1.49	-	-	-	-	-	-	-	-
Se	-	-	-	-	-	-	-	-	-	-	-	-	-	-
Mo	60.61	0.19	-	-	-	-	-	-	-	-	-	-	-	-
Ag	-	-	-	-	-	-	-	-	-	-	69.46	30.54	6.26	1.59
Au											1.91	1.91	93.74	1.59
Sb	-	-	-	-	-	-	-	-	-	-	-	-	-	-
Te	-	-	-	-	-	-	-	-	-		-	-	-	-
W	-	-	-	-	-	-	61.18	0.96	58.60	0.62	-	-	-	-
Au	-	-	-	-	-	-	-	-	-	-	-	-	-	-
Sb	-	-	-	-	-	-	-	-	-	-	-	-	-	-
Te	-	-	-	-	-	-	-	-	-	-	-	-	-	-
Bi	-	-	-	-	-	-	-	-	-	-	-	-	-	-
Pb	-	-	-	-	-	-	-	-	-	-	-	-	-	-
Total	99.96	0.10	99.15	1.03	99.69	0.96	100.00	0.00	100.00	0.00	100.00	0.00	100.00	0.00

* Electrum analysed form the late style 1 mineralization in the sample L-BSZ-2

** Electrum analysed form the style 2 mineralization in the sample WAu-4

Appendix 7B: Silicate minerals

Silicate minerals include plagioclase series, alkali (K) feldspar, biotite, chlorite, white clay assemblages, zircon, titanite, and rarely allanite. The average composition of these minerals are shown in Table 2. Trace silicate minerals including zircon, thorite, allanite, and titanite have detailed compositions and locations in Table 2.

Feldspars were determined from the SEM for all zones in the Revenue occurrence and where identified as albite (n=16), oligoclase (n=17), andesine (n=15), anorthoclase (n=1), and alkali feldspar (n=101).

Biotite from the Revenue granite host rock, the early and late BSPZ (total n = 34) has variable SiO_2 (39.75-46.46 wt%), Al_2O_3 (13.98-29.00 wt%), FeO (13.88-22.08 wt%), MgO (6.17-20.83 wt%), K_2O (2.53-10.19 wt%), and TiO_2 (0.52-0.32 wt%).

Chlorite was analysed from the Revenue granite, the early and late BSZ, and QFP. An average composition (n = 37) has SiO_2 (34.36±1.14 wt%), 23.43±1.26 wt% Al_2O_3 (23.43±1.26 wt%) with variable FeO (18.59-28.08 wt%) and MgO (15.37-22.30 wt%).

White clay assemblages from the late BSZ, phyllic altered QFP, WAu breccia, and Revenue diatreme were determined to be illite-kaolinite±muscovite via infrared spectroscopy (See Appendix 4). Using the SEM, white clays (n=79) have variable compositions of SiO_2 (36.83-64.28 wt%), Al_2O_3 (16.14-42.89 wt%), FeO (0.30-31.67 wt%), MgO (0.35-16.48 wt%), K_2O (0.22-12.68 wt%), and TiO_2 (0.32-1.68 wt%).

Table 2. Mineral compositions of silicate minerals obtained via SEM-EDS in wt%.

	Silicate Minerals																	
	ab n=16		olg n=17		andes n=15		k-fds n=150		bt n=34				chl n=37		clay n=104			
Oxide (wt%)	Avg	1 σ	Avg	1 σ	Avg	1 σ	Avg	1 σ	Avg	1 σ	Min	Max	Avg	1 σ	Avg	1 σ	Min	Max
SiO_2	67.31	1.40	62.66	1.14	60.34	0.35	66.23	1.39	42.58	1.15	39.75	46.46	34.36	1.14	55.02	2.00	46.98	63.28
TiO_2	-	-	-	-	-	-	-	-	1.77	0.90	bdl	4.32	-	-	bdl	0.21	bdl	0.58
Al_2O_3	20.01	1.17	23.97	1.73	25.33	0.40	18.02	1.02	16.58	4.05	13.98	29.00	23.43	1.26	32.82	3.02	24.64	42.69
FeO	-	-	-	-	-	-	-	-	15.92	1.80	13.88	20.97	22.46	2.57	1.39	1.64	bdl	9.01
Fe_2O_3	bdl	-	bdl	-	bdl	-	bdl	-	-	-	-	-	-	-	-	-	-	-
MnO	-	-	-	-	-	-	-	-	-	-	-	-	-	-	-	-	-	-
ZnO	-	-	-	-	-	-	-	-	-	-	-	-	-	-	-	-	-	-
MgO	-	-	-	-	-	-	-	-	14.94	2.63	6.17	18.04	19.60	1.85	2.04	1.86	0.50	10.78
CaO	0.85	1.10	4.31	1.67	6.58	0.89	bdl	-	-	-	-	-	-	-	bdl	0.37	bdl	0.45
Na_2O	11.21	0.86	8.47	1.01	7.42	0.27	0.85	0.99	-	-	-	-	-	-	-	-	-	-
K_2O	0.50	0.55	0.56	0.83	0.25	0.54	14.07	1.49	8.10	2.22	2.53	10.19	-	-	8.28	2.30	bdl	11.78
P_2O_5	-	-	-	-	-	-	-	-	-	-	-	-	-	-	-	-	-	-
ZrO_2	-	-	-	-	-	-	-	-	-	-	-	-	-	-	-	-	-	-
La_2O_3	-	-	-	-	-	-	-	-	-	-	-	-	-	-	-	-	-	-
Ce_2O_3	-	-	-	-	-	-	-	-	-	-	-	-	-	-	-	-	-	-
ThO_2	-	-	-	-	-	-	-	-	-	-	-	-	-	-	-	-	-	-
UO_3	-	-	-	-	-	-	-	-	-	-	-	-	-	-	-	-	-	-
F	-	-	-	-	-	-	-	-	-	-	-	-	-	-	0.34	0.74	bdl	2.38
Total	100.02	0.03	100.01	0.02	100.01	0.03	99.55	1.31	99.89	0.12	99.70	100.01	99.93	0.23	99.98	0.06	99.61	100.10

Table 2 cont'd. Mineral compositions of silicate minerals obtained via SEM-EDS in wt%.

	Silicate Minerals									
	zrn		aln				thr			
	n=22		n=14				n=5			
Oxide (wt%)	Avg	1 σ	Avg	1 σ	Min	Max	Avg	1 σ	Min	Max
SiO_2	31.70	0.51	41.05	0.79	39.68	42.27	19.12	0.60	18.57	19.87
TiO_2	-	-	-	-	-	-	-	-	-	-
Al_2O_3	-	-	17.78	1.49	16.21	22.54	-	-	-	-
FeO	-	-	11.21	0.78	9.38	13.06	-	-	-	-
Fe_2O_3	-	-	-	-	-	-	-	-	-	-
MnO	-	-	-	-	-	-	-	-	-	-
ZnO	-	-	-	-	-	-	-	-	-	-
MgO	-	-	1.49	0.19	1.18	1.89	-	-	-	-
CaO	-	-	11.71	0.89	11.18	14.68	1.76	0.17	1.46	1.87
Na_2O	-	-	0.18	0.36	0.00	0.88	-	-	-	-
K_2O	-	-	-	-	-	-	-	-	-	-
P_2O_5	-	-	-	-	-	-	-	-	-	-
ZrO_2	68.25	0.52	-	-	-	-	-	-	-	-
La_2O_3	-	-	4.98	0.48	3.95	6.65	-	-	-	-
Ce_2O_3	-	-	8.94	0.79	7.97	10.99	-	-	-	-
ThO_2	-	-	2.74	1.30	bdl	4.13	67.95	12.29	52.75	77.66
UO_3	-	-					9.17	12.67	bdl	25.37
F	-	-	-	-	-	-	0.62	0.85	bdl	1.55
Total	100.00	0.01	100.00	0.02	99.97	100.03	100.00	0.00	100.00	100.00

Appendix 7C: Oxide minerals

Oxides found at all mineralization styles of the Revenue occurrence include rutile (W and Sn variance), ilmenite, uraninite and hematite. Average mineral compositions of oxides are shown in Table 3. Rutile from the early BSZ (n = 7) area has TiO_2 (98.18±0.14 wt%) and FeO (1.82±0.14 wt%). Rutile form the late BSZ (n = 9) has TiO_2 (99.62±0.71 wt%), FeO (0.14±0.26 wt%), variable WO_3 (<1.5 wt%) and CaO (0.15±0.25 wt%). Rutile from the QFP (n = 8) has TiO_2 (99.30±0.42 wt%), FeO (0.08±0.16 wt%), and CaO (0.55±0.31 wt%). Rutile from the WAu breccia (n = 28) has TiO_2 (98.30±1.57 wt%), FeO (0.38±0.23 wt%), CaO (0.12±0.40 wt%), WO_3 (and < 3.53 wt%), and SnO_2 (< 1.98 wt%). Rutile from the Revenue diatreme (n = 30) has TiO_2 (97.56±2.50 wt%), WO_3 (< 6.18 wt%), and minor FeO (0.20±0.36 wt%). Two analyses in this area had Cr_2O_3 (0.66 and 0.73 wt%) in the analysis associated with highest WO_3. Accessory oxides include ilmenite, hematite, and uraninite, where compositions are detailed in Table 3.

Table 3. Normalized oxide mineral compositions in wt%, derived from SEM analysis.

	Minerals									
	rt				ilm		urn		hem	
	n=82				n=1		n=18		n=4	
Oxide (wt%)	Avg	1 σ	Min	Max	Avg	1 σ	Avg	1 σ	Avg	1 σ
TiO_2	98.37	1.97	92.66	100.00	52.99	-	-	-	-	-
Al_2O_3	bdl	0.04	bdl	0.40		-	-	-	-	-
FeO	0.31	0.46	bdl	1.97	45.73	-	-	-	100	0
MnO	-	-	-	-	1.28	-	-	-	-	-
CaO	0.18	0.36	bdl	1.58	-	-	-	-	-	-
K_2O	bdl	0.20	bdl	0.41	-	-	-	-	-	-
Cr_2O_3	bdl	0.11	bdl	0.73	-	-	-	-	-	-
SnO_2	bdl	0.25	bdl	1.98	-	-	-	-	-	-
WO_3	1.08	1.63	bdl	6.18	-	-	-	-	-	-
UO_3	-	-	-	-	-	-	96.25	3.33	-	-
ThO_2	-	-	-	-	-	-	6.43	0.52	-	-
Total	100.00	0.00	99.98	100.02	100.00	0.00	100.00	0.01	100.00	0.00

Appendix 7D: Carbonate minerals

Carbonate minerals are a common gangue mineral, present in all samples that were studied in depth. The carbonate phases present are calcite, Fe-dolomite, and a siderite phase with variable composition. Carbonates were analysed via SEM, and proportions were calculated in molecular percent (mol.%) using cation oxide data (Table 4). Due to occasional trace amount of MnO, FeO+MnO were grouped together in the calculations and ternary graphics, though the amount of MnO in Fe-dolomite and siderite phases are usually negligible when determining mineral identification (<3.30 mol.% in each analysis, usually <1 mol%.). Calcite occurs in the Revenue granite host, early BSZ, least altered QFP, and in the WAu breccia, where it's average composition (n = 20) has CaO (99.20±0.86 mol%), MgO (< 1.09 mol%), and FeO+MnO (< 2.12 mol%). Fe-dolomite occurs in the late BSZ, phyllic altered QFP and Revenue diatreme, and in the WAu breccia where it's average composition (n = 68) has variable CaO (49.67±2.38 mol%), MgO (18.03 - 40.52 mol%), and FeO+MnO (11.99 - 31.91 mol%). The range in compositions show that the WAu breccia and late BSZ generally have higher FeO content, and analyses from the phyllic altered QFP dyke typically are lower-FeO content, though analyses for samples show similar ranges. Siderite occurs in the late BSZ, WAu breccia, and both least altered and phyllic altered Revenue diatreme. Siderite (n = 73) has variable FeO+MnO (47.20 - 100.00 mol%), MgO (< 48.0 mol%), and CaO (< 13.79 mol%). Like the Fe-dolomite, the compositions in each mineralized zone varies although general trends of FeO-dominant siderite occur in the WAu breccia, whereas the lower FeO content siderite occurs in the Revenue diatreme and the late BSZ composition ranging throughout.

Table 4. Normalized molecular proportions of carbonate phases in the Revenue occurrence, derived from SEM analysis.

	Carbonate Minerals											
	cal				dol				sd			
	n=20				n=67				n=73			
Oxides (Mol %)	Avg	1σ	Min	Max	Avg	1σ	Min	Max	Avg	1σ	Min	Max
CaO	99.20	0.86	97.21	100.00	49.67	2.38	45.48	57.23	1.82	2.48	bdl	13.79
MgO	bdl	0.24	bdl	1.09	31.35	5.11	18.03	40.52	14.12	14.91	bdl	48.00
FeO+MnO	0.75	0.76	bdl	2.12	18.98	4.23	11.99	31.91	84.07	15.69	47.20	100.00
Total	100.00	0.00	100.00	100.00	100.00	0.00	100.00	100.00	100.00	0.00	100.00	100.00

Appendix 7E: Phosphates and trace minerals

Phosphates including apatite, xenotime, and monazite, and other minerals including barite and cassiterite, have average mineral compositions condensed in Table 5 and 6, respectively.

Table 5. Phosphate mineral compositions in wt% oxide for apatite, monazite and xenotime.

	Phosphate Minerals											
	ap				mnz				xtm			
	n=60				n=8				n=3			
Oxide (wt%)	Avg	1 σ	Max	Min	Avg	1 σ	Min	Max	Avg	1 σ	Min	Max
CaO	49.33	2.51	54.44	46.34	-	-	-	-	-	-	-	-
P_2O_5	45.41	1.06	47.57	40.40	39.10	4.52	34.34	45.85	41.63	1.04	40.83	42.80
La_2O_3	-	-	-	-	12.89	10.70	bdl	21.53	-	-	-	-
Ce_2O_3	-	-	-	-	30.15	5.00	21.24	34.58	-	-	-	-
Nd_2O_3	-	-	-	-	16.57	10.77	8.26	32.92	-	-	-	-
Y_2O_3	-	-	-	-	-	-	-	-	47.00	2.31	45.20	49.60
Gd_2O_3	-	-	-	-	-	-	-	-	2.76	0.50	2.19	3.10
Dy_2O_3	-	-	-	-	-	-	-	-	5.31	0.83	4.50	6.15
Yb_2O_3	-	-	-	-	-	-	-	-	1.31	3.02	bdl	5.23
ThO_2	-	-	-	-	0.15	0.42	bdl	1.19	1.58	2.74	bdl	4.75
F	4.66	2.79	7.82	bdl	1.00	2.09	bdl	5.80	-	-	-	-
Cl	0.11	0.15	0.45	bdl	-	-	-	-	-	-	-	-
Total	100.00	0.01	100.02	99.99	100.00	0.01	100.00	100.02	100.02	0.02	100.00	100.03

Table 6. Additional mineral chemistry in oxide wt% for barite and cassiterite.

	Trace Minerals			
	brt		cst	
	n=6		n=1	
Oxide (wt%)	Avg	1 σ	Avg	1 σ
SO_3	37.77	0.14	10.79	-
FeO	-	-	7.44	-
BaO	61.69	1.05		-
CuO	-	-	2.08	-
SnO_2	-	-	79.69	-
SrO	0.64	0.99		-
Total	100.00	0.00	100.00	0.00

Appendix 8: Revenue occurrence model

The current deposit model involves a telescoping porphyry intruded by QFP dykes, resulting in skarn-like breccia, where a later pressure-release event resulting in the Revenue diatreme intruding to shallow depths, where mineralization may have been remobilized upon expanding dilation zone (T. Baressi, communication, 2018). The hypothesis of the fault system growing over-pressured as a result of the late-Cretaceous emplacements (located SE of the Revenue occurrence, Fig. 2) blocking and deforming the fault's passage may have led to an increase in pressure in the property (T. Baressi, communication, 2018). This "over-pressured" system could result in migrating hydrothermal fluids, multiple generations of mineralization, and breccia formations, and a final event of the diatreme (T. Baressi, personal communication 2018).

The Revenue granite pluton, emplaced ~105 Ma, hosts a porphyry of a later date of ~75 Ma, where early mineralization style 1 formed in association with calcite and potassic alteration including biotite and minor K-feldspar. This mineralization derived reduced fluids (Rowins, 2000), where pyrrhotite is dominant in the main mineralization and magnetite is absent in alteration assemblage. Possible oxidation or other changes in condition and chemistry allowed rutile±ilmenite to alter pyrrhotite (Fig. 8A). Therefore the main mineralization sequences was dominant in pyrrhotite, then pyrite and chalcopyrite. The source magma is implied to be mantle derived based on the Co-Ni affinity in trace element composition. The magma chamber would then cool, ending this mineralization event.

After, shallowly emplaced QFP dykes of the Casino Plutonic Suite, at similar age of ~75 Ma swarmed the region (Friend et al., 2018; Betsi et al., 2010 2011, 2013). These dykes are oriented W-E across the property, cross-cutting the Revenue granite and BSZ.

An alteration process dominant in chlorite pseudomorphically altering biotite with rutile± sulfide occurred throughout the region.

Another surge of magmatism onset the development of the late style 1 mineralization, in which similar structures were used to transport polymetallic-bearing hydrothermal fluids and cross-cut older base metal-biotite altered veins. The magma source produced oxidized, epithermal-type hydrothermal fluids, as implied by trace element composition and lack of pyrrhotite. These new fluids have a large carbonate component present as dolomite instead of calcite, and a shift in dominant sulfides to pyrite-chalcopyrite and introduction of molybdenite and arsenopyrite. Mineralization occurred in at least two phases, the first with an early quartz-dominated mineralization and later dolomite phase. Given the trace geochemical data in conjunction with petrographic observations, the mineralization style 1 is clearly split into two events that may share the same magma and hydrothermal fluid source, though the composition and conditions of the source would have differed between the two veining (quartz vs dolomite) events. This late style 1 mineralization and alteration affected QFP dykes in the region, as seen by the similar late style 1 mineralization cross-cutting crystals in the sample QFP-2.

At a similar time, shortly after and likely associated to QFP dyke emplacement, a breccia system occurred in the near the SW region of the BSZ area. Revenue granite and QFP fragments, showing chilled margins, are suspended in a quartz-carbonate-sulfide matrix, which characterizes style 2 mineralization. Yet another source, characterized by saline hydrothermal fluids, carried increased amounts of W and Sn in conditions that favoured siderite, of which precipitated in open spaces. Ferberite-scheelite masses and coarse grain galena suggest long mineralization times under preferable conditions, with late-phase pyrite (ii) shows boiling, open-space filling textures which may imply a sudden

shift in decreased pressure possibly related to uplift. Trace element compositions of major sulfides, in conjunction with W and Sn mineralization imply skarn-like influences for this mineralization.

Lastly, a diatreme intrudes the Revenue complex as a final pressure release from the over pressured system (T. Barressi, personal communication 2018). The initial high pressure and temperature may have caused previous mineralization to remobilize and become attenuated near the contacts of the diatreme with the Revenue granite and early BSZ mineralization, which characterizes mineralization style 3. Alternatively, a similar fluid source from the formation of the style 2 mineralization may be responsible for the metal carrying hydrothermal fluids for style 3 mineralization. No mineralization is recognized in the Revenue area afterwards.